

Improving the Wind Farm efficiency by simple means

LES study of a wind turbine array with tethered kites

Evangelos Ploumakis

Master of Science Thesis



Improving the Wind Farm efficiency by simple means

LES study of a wind turbine array with tethered kites

MASTER OF SCIENCE THESIS

For the degree of Master of Science in Sustainable Energy Technologies
at Delft University of Technology

Evangelos Ploumakis

September 8, 2015

Faculty of Aerospace Engineering (AE), Wind Energy Research Group · Delft University of
Technology



Copyright © Faculty of Aerospace Engineering (AE)
All rights reserved.

DELFT UNIVERSITY OF TECHNOLOGY
DEPARTMENT OF
FACULTY OF AEROSPACE ENGINEERING (AE)

The undersigned hereby certify that they have read and recommend to the Faculty of
Aerospace Engineering (AE), Wind Energy Research Group for acceptance a thesis
entitled

IMPROVING THE WIND FARM EFFICIENCY BY SIMPLE MEANS

by

EVANGELOS PLOUMAKIS

in partial fulfillment of the requirements for the degree of
MASTER OF SCIENCE SUSTAINABLE ENERGY TECHNOLOGIES

Dated: September 8, 2015

Supervisor(s):

dr.ir. Wim Bierbooms

Prof. dr. Gerard van Bussel

Reader(s):

dr.ir. Stephan de Roode

ir. Dhruv Mehta

ir. Lorenzo Lignarolo

Abstract

Wake effects in wind farms are a major source of power production losses and fatigue loads on the rotors. It has been demonstrated that in large wind farms the only source of kinetic energy to balance that extracted by the turbines is the vertical transport of the free-stream flow kinetic energy from above the wind-turbine canopy. In the present study, the possibility to enhance such process by introducing kites in steady flight within the wind-turbine array is studied with numerical simulations.

An aligned array of four wind turbines is simulated within the LES framework available in the computational fluid dynamics code `FLUENT`. The turbines are placed in a pre-generated turbulent atmospheric boundary layer (ABL) and modelled as actuator discs with both axial and tangential inductions, to account for the wake rotation. The inter-turbine spacing is six rotor diameters while a kite is suspended three diameters downwind each wind turbine, 0.25 diameters above the top-tip height. The kite is modelled as a body force on the flow, equal in magnitude and opposite in direction to the vector sum of the lift and drag forces acting on the kite.

The introduction of the kite system is found to have a significant effect on the power generated by the wind turbine array primarily due to the enhanced kinetic energy entrainment in the lower part of the ABL. The simulation results, consistent with previous findings, clearly suggest that the applied forcing is capable of redirecting the free-stream flow and assist wake recovery. Follow-up research on kite layout strategies for large wind farms and multiple wind directions as well as an analysis of different kite flight paths (i.e. crosswind motion) in the array is suggested.

Table of Contents

Acknowledgements	vii
Nomenclature	xv
1 Introduction	1
1-1 Background	1
1-1-1 Challenges related to large Wind Farms	2
1-1-2 Wind Turbine Wakes	2
1-1-3 Wind Turbine Wake interactions	4
1-1-4 Modelling of the wake	5
1-2 Previous work	5
1-3 Present work	8
1-3-1 Outline	9
2 Kite surface aerodynamics	11
2-1 3D wing aerodynamics	12
2-1-1 Kite shapes & Design requirements	14
3 Atmospheric Boundary Layer and Wind Turbine Aerodynamics	15
3-1 The Atmospheric Boundary Layer (ABL)	15
3-1-1 Atmospheric Stability	16
3-1-2 Turbulence	17
3-2 Actuator Disc concept	17
3-2-1 One-dimensional momentum theory and Betz limit	17

4	Computational Fluid Dynamics	19
4-1	Governing equations	19
4-1-1	Navier-Stokes equations	20
4-2	Approximate forms of the Navier-Stokes equations	21
4-2-1	Large eddy simulations (LES)	22
4-3	Discretization	23
4-3-1	Spatial Discretization	23
4-3-2	Temporal Discretization	24
4-4	Near-wall treatment for LES	25
4-5	Modelling of the rotor	26
4-6	Modelling the Atmospheric Boundary Layer (ABL)	26
5	Numerical simulations of the Atmospheric Boundary Layer (ABL)	29
5-1	Numerical wind flow	29
5-1-1	Spatial discretization	30
5-1-2	Computational domain	31
5-1-3	Numerical settings	32
5-1-4	Boundary conditions	32
5-2	ABL simulation results	33
5-3	Discussion	36
6	Numerical simulations of a wind turbine array	37
6-1	Numerical approach	37
6-1-1	Actuator Disc model in FLUENT	39
6-1-2	Wake rotation	41
6-1-3	Wind turbine array efficiency	43
6-2	Wind Turbine array simulation results	44
	(a) 2 wind turbines in a row	44
	(b) 4 wind turbines in a row - ADM-NR/ADM-R	47
	(c) 4 wind turbines (ADM-R) - partial vs optimal load	55
6-3	Discussion	58
7	Numerical simulations of a wind turbine array with tethered kites	61
7-1	Modelling the kite surface	62
7-2	Kite modelling conventions	64
7-3	Numerical setup	65
7-4	Numerical simulation results	67
	(a) DSE report methodology & Kite facing study	67
	(b) Kite sizing: $A_{kite,s}$ & $A_{kite,l}$	69
	(c) ADM-R & $A_{kite,l}$ under partial and optimal load	72
	(d) ADM-R $C_T=0.88$ & $A_{kite,l}$ - high power density	75
7-5	Discussion	78

8	Conclusions	81
8-1	Recommendations	82
8-1-1	ABL profiles	82
8-1-2	Wind turbine array with kites	82
A	UDF - Read velocity profiles	85
A-1	FLUENT on the HPC12 cluster	85
A-2	FLUENT commands	86
A-3	User Defined Function (UDF) code	87
B	Four wind turbines - local grid refinement	89
C	Kite system calculations	93
C-1	Pressure distribution	93
C-2	Normal force calculations	93
	Bibliography	97

Acknowledgements

I would like to express my gratitude and thanks to my supervisors Wim Bierbooms, Dhruv Mehta and Lorenzo Lignarolo for their guidance and support in the work leading to this thesis. Their expertise on atmospheric flows, numerical simulations and wind turbine aerodynamics proved invaluable in the course of this diverse and fascinating project. Being constantly engaging and friendly, gave rise to many rewarding discussions during our scheduled meetings and/or my casual walk-ins.

I would like to thank Gerard van Bussel and Stephan de Roode for participating in the defence committee. A special thanks to Roland Schmehl for his active guidance on airborne wind energy systems and for doing me the honour to present my thesis work at the Airborne Wind Energy Conference 2015. Additionally, my gratitude goes out to Sander van Zuijlen for granting me access to the computer cluster and for his patience to deal with all the novice questions and missteps.

Since, I have already become part of the Dutch wind energy industry, I would like to extend my thanks to my new colleagues Martijn and Dennis at Lagerwey Wind for their warm welcome and for making my transition from the university to the new working environment as smooth as possible.

A special word of thanx to my fellow students in student room 5.12. Aside from the casual thesis brainstorming there was always the time for yet another cup of coffee, news updates, political discussions, always something to chat about cheering up the daily routine making the thesis work that much funnier and a lot more memorable.

Finally, I would like to express my sincere thanks and love to my friends, girlfriend and family for their love and support throughout all the years of my studies in Delft. At last but not least, I would like to thank my friend Nadina for the editing work on the cover page.

Evangelos Ploumakis
Delft University of Technology
Delft, August, 2015

List of Figures

1-1	Wind turbine wake regions and mixing. The vorticity magnitude in an axial wake plane of the NREL-5MW is plotted. [1].	3
1-2	Normalized power as function of wind turbine number in a farm at a wind speed of 8m/s; different models are compared to measurements [2].	7
1-3	The Daeolus kite system, placed in an offshore wind farm, as conceived by the S12 group [3].	9
2-1	The two Laddermill concepts [4].	12
2-2	Schematic representation of the crosswind pumping cycle's traction and retraction phases for the Delft KitePower system [5].	12
2-3	Upstream and downstream modification of the flow in the vicinity of a finite span lifting wing [6].	13
2-4	Lift Coefficient vs angle of attack for different Aspect Ratio wings. The effect of how decreasing the aspect ratio or increasing the sweep decreases the C_L/α slope [7].	14
3-1	Vertical structure of the earth's atmosphere. The ABL is found in the lowest portion of the troposphere and is separated by the rest of the troposphere by a capping inversion [8].	16
3-2	Schematic of the flow going over the wind turbine blades when modelled as an ADM [9].	18
4-1	Resolved vs modelled turbulence scales for RANS LES and DNS models.	22
4-2	(Left) Non-uniform Structured Grid, (Right) Non-uniform Unstructured Grid . . .	23
4-3	Discretization of the convective terms (flow direction from left to right)	24

5-1	Sizing and impression of the spatial discretization of the computational domain used in the ABL simulations	31
5-2	First order statistics: Vertical streamwise velocity profiles developed in the precursor simulation. Time averaged statistics for each flow pass after the 6th are presented. The black dashed line represents the target log-law profile for the given ground roughness characteristics.	34
5-3	Second order statistics: Vertical profiles of turbulence intensity developed in the precursor simulation. Time averaged statistics of TI for each successive flow pass, spatially averaged in the streamwise direction.	35
5-4	Non-dimensional velocity profile in a semi-log plot. The classical log law is represented with the black dashed line while the numerical results for the different flow passes in color.	36
6-1	C_P vs C_T of an ideal turbine [10].	38
6-2	Schematic view of the computational domain and two actuator discs aligned in the streamwise direction [11].	40
6-3	Power coefficient variation with tip speed ratio for an idealized 2MW turbine [12].	42
6-4	Side view of the computational domain with two wind turbines in a row.	45
6-5	Normalized x-velocity, \bar{u}/U_∞ , in the streamwise direction for AD1 and AD2.	46
6-6	Turbulence Intensity, in the streamwise direction (x-direction), downstream AD1 and AD2.	46
6-7	Visualization of the computational domain including 4ADs	47
6-8	Normalized x-velocity, \bar{u}/U_∞ , plots in the wake of the discs (ADM-NR). The time-averaged velocities are gathered in locations: $x/D=-1/1/3/5$	49
6-9	Turbulence intensity, in the streamwise direction (x-direction), at the discs (ADM-NR). The TI data are gathered in locations: $x/D=-1/1/3/5$	49
6-10	Out of plane velocity, \bar{w}/U_∞ , (z-direction) plots for the discs without specified tangential velocity (ADM-NR). The z-velocity data are gathered in locations: $x/D=-1/1/3/5$	50
6-11	Normalized x-velocity \bar{u}/U_∞ plots in the wake of the discs (ADM-R). The time-averaged velocities are gathered in locations: $x/D=-1/1/3/5$	51
6-12	Turbulence intensity, in the streamwise direction (x-direction), in the wake of the discs (ADM-R). The TI data are plotted in: $x/D=-1/1/3/5$	52
6-13	Out of plane normalized velocity, \bar{w}/U_∞ , (z-direction) plots for the discs (ADM-R) with specified tangential velocity. The z-velocity data are gathered in locations: $x/D=-1/1/3/5$	52
6-14	Side view of the normalized mean kinetic energy transport $\bar{\Phi}/U_\infty^3$ for the ADM and ADM-NR cases.	53
6-15	Normalized velocity deficit for ADM-R and ADM-NR plotted for three downwind distances $x/D=1/3/5$	54

6-16	Side view of the wake expansion for the ADM and ADM-NR cases. The contour represents the normalized streamwise velocity \bar{u}/U_∞	55
6-17	Top view of the wake expansion for the ADM and ADM-NR cases. The contour represents the normalized streamwise velocity \bar{u}/U_∞	55
6-18	Normalized x-velocity profiles (continuous lines) at a downwind distance of 5 rotor diameters ($x/D=5$) for the actuator discs. The x-crosses represent the velocity profiles at $x/D=-1$ for $C_T=0.88$ & the dotted (no lines) for $C_T=0.56$	57
6-19	Turbulence intensity profiles at a downwind distance of 5 rotor diameters ($x/D=5$) for each one of the actuator discs under partial and optimal loading. The x-crosses represent the velocity profiles at $x/D=-1$ for $C_T=0.88$ & the dotted lines for $C_T=0.56$	57
6-20	The radial profiles of the normalized mean flow-kinetic energy flux, $\bar{\Phi}$, are evaluated on the horizontal x-y plane. $\bar{\Phi}$ is plotted at $x/D=5$ downwind the actuator discs AD_i under partial and optimal load.	58
7-1	Grooves in the upper and lower surface due to ballooning of the wing [13].	62
7-2	Pressure coefficients for ballooned wing (cell-centre/rib) and the NACA0012 profile (wing) simulations [13].	63
7-3	Left: Pressure distribution on the first rib and cell centre at high angle of attack. Right: Same distribution at low angle of attack [13].	63
7-4	Left: (a) Force and velocity vectors at a kite in a continuous loop. Right: (b) kite in a static position [14].	65
7-5	Mesh of the computational domain including the kite system and detailed view of the successive mesh refinement around the kite area. The hexahedral cells at the kite surface are of 1m length in all directions ($\Delta x=\Delta y=\Delta z=c/16$).	66
7-6	Visualization of the kite facing configurations	68
7-7	Normalized x-velocity plots at a downwind distance of 5 rotor diameters ($x/D=5$) for the actuator discs. The simulation results of the two simulations using the ADM-R concept before and after the introduction of the kite system are presented. 70	70
7-8	Turbulence intensity profiles at a downwind distance of 5 rotor diameters ($x/D=5$) for each one of the actuator discs. Comparative plots of the base case only with the ADM-R, ADM-R + $A_{kite,s}$ & ADM-R + $A_{kite,l}$	70
7-9	Contour plots of TI_x values for the ADM-R and ADM-R + kite systems.	71
7-10	Radial profiles of the normalized mean flow-kinetic energy flux, $\bar{\Phi}$, evaluated on the horizontal x-y plane and plotted at $x/D=5$ downwind the actuator discs AD_i for the different kite sizes.	71
7-11	Normalized x-velocity profiles at a downwind distance of 5 rotor diameters ($x/D=5$) for the actuator discs. The x-crosses represent the velocity profiles at $x/D=-1$ for $C_T=0.88$ & the dotted (no lines) for $C_T=0.56$. The effect of different wind turbine loading on the wake velocity, including the $A_{kite,l}$ surface, is plotted.	73

7-12	Comparative plots of different loading for the turbine using the ADM-R model. Turbulence intensity profiles at a downwind distance of 5 rotor diameters ($x/D=5$) for each one of the actuator discs. The x-crosses represent the velocity profiles at $x/D=-1$ for $C_T=0.88$ & the dotted lines for $C_T=0.56$. The $A_{kite,l}=470m^2$ is used to simulate the kite surface in the flow.	74
7-13	The radial profiles of the normalized mean flow-kinetic energy flux, $\bar{\Phi}$, are evaluated on the horizontal x-y plane. $\bar{\Phi}$ is plotted at $x/D=5$ downwind the actuator discs AD_i under partial and optimal load after the introduction of the $A_{kite,l}$	74
7-14	Normalized x-velocity profiles at a downwind distance of 5 rotor diameters ($x/D=5$) for the actuator discs under optimal load ($C_T=2$). The effect of different kite power densities, on the wake velocity, is plotted.	77
7-15	Turbulence intensity profiles at a downwind distance of 5 rotor diameters ($x/D=5$) for each one of the actuator discs (ADM-R, $C_T=0.88$) . The $A_{kite,l}=470m^2$ with different power densities is used to simulate the kite in the domain.	77
7-16	The radial profiles of the normalized mean flow-kinetic energy flux, $\bar{\Phi}$, are evaluated on the horizontal x-y plane. $\bar{\Phi}$ is plotted at $x/D=5$ downwind the actuator discs (ADM-R) under optimal load after the introduction of the $A_{kite,l}$ with three different power densities.	78
B-1	Comparison of the normalized x-velocity \bar{u}/U_∞ profiles in the wake of the discs with rotation (ADM-R). The time-averaged velocities are plotted at $x/D=5$ downwind each one of the discs.	90
B-2	Comparison or the turbulence intensity levels, in the streamwise direction (x-direction), for different grid sizes. The TI data are are plotted at $x/D=5$ downwind each one of the discs (ADM-R).	90

List of Tables

5-1	Simulated wind and roughness parameters	30
5-2	Domain size and mesh specifications	31
5-3	Solver settings	33
5-4	Precursor simulation boundary conditions. The flow in the streamwise direction is driven by a specified pressure gradient, specified in the periodic BC's tab, for the successive flow passes.	34
6-1	Summary of cases and corresponding parameters for the numerical computations. The notation used for the actuator disc simulations without rotation, ADM-NR, and the simulations of the added swirl on the flow, ADM-R, is the one used in the work of Porté-Agel (2010) [15].	39
6-2	Summary of the wind turbine and wind inflow characteristics used in the numerical computations.	39
6-3	Tangential velocities for all blade elements. The results are plotted for partial ($C_T=0.56$) and optimal ($C_T=0.88$) loading of the discs.	43
6-4	Mesh details of the computational domain for case (a)	45
6-5	Case (a) results: Thrust force and extracted power for two actuator discs, with 10D spacing, aligned in the streamwise direction.	47
6-6	Mesh details of the computational domain	48
6-7	Case (b1) results: Thrust force and power extracted for each one of the four actuator discs without swirl velocity specification (ADM-NR).	50
6-8	Parameters used to estimate the tangential velocity coefficient h_n at $r=R$ for $C_T=0.56$ & $\lambda=7$	51
6-9	Case (b2) results: Average velocity at the discs, thrust force and power extracted for the four wind turbine case with added swirl.	53

6-10	Parameters used to estimate the tangential velocity coefficient h_n at $r=R$ for $C_T=0.88$ & $\lambda=8$. The mean velocities at the discs are estimated to be 20% lower than the ones predicted in table 6-9.	56
6-11	Case (c) results: Average discs velocities, thrust and extracted power for the actuator disc model with rotation (ADM-R) operating under optimal load, $C_T=0.88$. The power extracted values of $C_T=0.56$ are also presented for comparison. . . .	58
7-1	Summary of cases and corresponding parameters for the numerical computations of a wind turbines array with suspended kites.	62
7-2	Flow characteristics of the kite system, under steady flight, used in the numerical simulations.	66
7-3	Size and mesh details of the computational domain	67
7-4	Case (a) results: Simulation results after the introduction of the kite system. The effect of two facing configurations for a $105m^2$ kite surface is treated in the test case. The base case results, before the introduction of the kites, are presented in the bottom line.	68
7-5	Case (b) results: Simulation results of the case with the $A_{kite,l}=470m^2$ kite system. Power and efficiency values are also presented for case (a2) and the base case.	72
7-6	Reference parameters used in the simulations for the partial and optimal load cases with the $A_{kite,l}$	72
7-7	Case (c) results: Simulation results of the different wind turbine loading cases, for the actuator disc with rotation (ADM-R) with the $A_{kite,l}=470m^2$ kite system.	75
7-8	Kite flight parameters used to simulate the different kite power densities.	76
7-9	Case (d) results: Simulation results for the large kite surface $A_{kite,l}=470m^2$ and high power densities, using the actuator disc with rotation (ADM-R) under optimal loading $C_T=2$	78
B-1	Case (d) results: Grid resolution and computational time per time step for the coarse (D/5), base (D/10) and refined (D/20) grid sizes. The time-averaged streamwise velocities at the discs and the efficiency values for the array are presented.	91
C-1	Pressure jump calculation steps for a reference wing surface with chord $c=1$ for an ambient velocity of 7.8 m/s.	94
C-2	Pressure coefficient data for the upper and lower surface of the $470 m^2$ kite based on the simulation data obtained from Aart de Wachter (2008) [13]. The normal force coefficient and normal force values for a wind velocity of 7.8m/s, 11m/s & 15.6m/s	95

Nomenclature

List of Symbols & Abbreviations

α	Angle of attack
α_i	Induced angle of attack
$\bar{\Phi}/U_{hub,\infty}^3$	Normalized kinetic energy flux in the vertical direction
β	Kite elevation angle
ΔP	Pressure jump
Δt	Time-step size
κ	Von Karman constant
λ	Tip speed ratio
$\langle u'^2 \rangle, \langle u'v' \rangle, \langle v'^2 \rangle$	Reynolds stresses
ω	Rotational speed
Φm	Dimensionless wind shear
τ_w	Shear stress at the wall
ε	Kite glide angle
$A_{kite,l} = A_{AD_i}/12$	Large kite surface
$A_{kite,s} = A_{AD_i}/48$	Small kite surface
<i>ABL</i>	Atmospheric Boundary Layer
<i>AD</i>	Actuator Disc
<i>ADM – NR</i>	Actuator Disc model with only axial induction
<i>ADM – R</i>	Actuator Disc model with axial and tangential inductions
<i>AL</i>	Actuator Line
<i>AR</i>	Aspect ratio
<i>AS</i>	Actuator Surface
<i>AWE</i>	Airborne Wind Energy
C_l	Lift coefficient
C'_P	Modified power coefficient
C_R	Resultant aerodynamic force coefficient

C'_T	Modified thrust coefficient
C_{D_i}	Induced drag
C_d	Drag coefficient
C_{F_a}	Normal force coefficient
$C_{p,l}, C_{p,u}$	Pressure coefficients for the upper and lower wing surfaces
C_P	Power coefficient
C_T	Thrust coefficient
CFD	Computational Fluid Dynamics
f	Coriolis parameter
F_D	Aerodynamic drag force
F_L	Aerodynamic lift force
f_n	Pressure jump coefficient
F_T	Aerodynamic thrust force
F_t	Tether force
h_n	Tangential velocity coefficient
$HAWT$	Horizontal Axis Wind Turbine
LES	Large Eddy Simulations
n_f	Efficiency of the wind turbine array
P	Extracted power
P_l	Kite power density
R_i	Richardson number
\tilde{R}_i	Richardson number
Re	Reynolds number
TI	Turbulence Intensity
TI	Turbulence Intensity
u_*	Friction velocity
U_∞	Free stream velocity
u_θ	Tangential velocity
u_a	Apparent wind velocity
u_D	Streamwise velocity at the disc averaged over the disc area
ν	Kinematic viscosity
w	Downwash velocity
w	Out-of-plane velocity component
a	Axial induction factor
a_t	Tangential induction factor
ρ	Density

Chapter 1

Introduction

1-1 Background

Humanity has harnessed the power of the wind for thousands of years initially through sails and wind mills. For more than two thousand years wind-powered machines had been used to pump water and grind grain. In Mykonos and in other islands of Greece windmills were used to mill flour and remained in use until the early 20th century. By the end of the 19th century pioneers such as Poul la Cour employed wind energy for generating electricity. The energy crisis of the 1970s accelerated the development of industrial sized wind turbines especially in countries such as the USA, Germany and Denmark. The world's first multi-megawatt wind turbine was constructed in 1978 ("*Danish development*") pioneering many technologies used in modern wind turbines, and followed in 1980 by the world's first onshore wind farm in Crotched Mountain, NH, USA. The first offshore wind farm, consisting of 11 turbines, was installed in Vindeby, Denmark. At the moment, the largest onshore wind farm in the world, Gansu Wind farm in China has a capacity of over 6,000MW with a goal of 20,000MW by 2020 and is followed by the Alta Wind Energy Center in California, with a capacity of 1,020MW. As of April 2013, the 630MW London Array in the UK is the largest offshore wind farm in the world. In 2015, GE was still the largest U.S. manufacturer of wind turbines, although recently overtaken by the Danish company Vestas as the largest manufacturer and installer in the world.

In 2008, the EU adopted a baseline target of at least 20% of the total energy consumption be supplied by renewable energy sources by 2020¹. Wind power is currently the most developed renewable technology and is expected to deliver the lion's share in the transition from fossil based energy production to renewables. Despite the historic usage of wind power in the Netherlands, the country lags behind most EU countries in the production of energy from renewable sources. In 2010, The Netherlands used only 4% wind power of electricity, when the equivalent for Germany is 9.4% and Portugal 14%. Winds of change, though, appear

¹Directive 2009/28/EC of the European Parliament and of the Council of 23 April 2009: <http://eur-lex.europa.eu/legal-content/en/TXT/?uri=CELEX:32009L0028>

on the Dutch horizon since in January 2015 the Ministry of Economic Affairs, as part of its National Energy Agreement², announced a goal of 16% sustainable energy use by 2023.

Large wind farms (mainly offshore) will play an instrumental role in reaching the objectives of the adopted policies around the world towards making renewable energy deliver a larger portion of the world's total energy consumption. Wind farms in the scale of Gansu, also provide new challenges in terms of optimizing power production and decreasing the overall cost of energy, as large scale wind farm production is still in its infancy.

1-1-1 Challenges related to large Wind Farms

Large wind farms are usually organised in patterns of rows and columns and the array configuration is typically decided upon the dominant wind direction and turbine size. The array configuration along with the variability in the wind direction means that all turbines will experience wake situations since they will more or less be aligned with one or more upstream turbines and their wakes. With the fast growing number of wind energy projects installed worldwide, an increasing number of wind turbines have been installed in large wind farms resulting in reduced inter-turbine spacing and significant power losses i.e. Barthelmie et al. [2] reported power losses of more than 40% for certain wind directions at Horns Rev. The interaction of the undisturbed wind flow with wind turbines results in a wake flow also associated with increased turbulence levels and higher fatigue loads for the downstream turbines. On the other hand, the added turbulence facilitates increased turbulent mixing, which entrains more energy from the surrounding atmosphere leading to a faster wake recovery. Wake effects become comparatively more important in off-shore wind farms, where the atmospheric turbulence is lower and the wake region persists for a longer area behind the rotor [16].

One of the main challenges that the wind industry faces today involves an incomplete understanding of the aerodynamics within the wind farm. The performance of a wind farm has a strong correlation to the spatial distribution (array configuration) of the turbines in a single array. Therefore, the accurate computation of the wake momentum deficit downwind a wind turbine is of crucial importance for wind farm operators in order to maximize energy capture and minimize power losses transferred to the electrical grid. The present work sets out to provide new ideas aimed at addressing the challenges related to wake effects in wind turbine arrays, such as the available kinetic energy in downstream locations under "full wake" conditions.

1-1-2 Wind Turbine Wakes

Modern wind turbines extract kinetic energy from the wind and convert it to electricity. It is then expected from the basic concept of energy conservation that the extraction of kinetic energy from the wind results in a decrease of the wind velocity (wake) downstream of a wind turbine when compared to the free/undisturbed flow. A deeper insight, into large scale interactions found in the atmosphere, is gained via the study of the main transport and mixing mechanisms typically observed in the atmospheric boundary layer. Due to instabilities, inherent in atmospheric flows, disturbances will form vortical structures, where the shear layer

²Netherlands Enterprise Agency January 2015: <http://english.rvo.nl/sites/default/files/2015/01/Offshore%20wind%20energy%20in%20the%20Netherlands.pdf>

"rolls up", that merge and form large coherent structures transporting each stream into the other (convective transport). Those vortical structures achieve transport but this mechanism is not enough to complete the mixing. Inside those larger vortical structures, there are rolled-up shear layers. These again form vortical structures and so on to much smaller scales. Many levels of shear form, but only at the smallest ones through mixing occurs. With increasing Reynolds number, the variety of size scales increases meaning also the smallest scales get smaller, so mixing is promoted. As with any property depending on the generation of small scales, the location of the mixing transition depends on the level of perturbations in the initial conditions of the shear layer. Added streamwise vorticity i.e. tip-induced vortices in the shear layer can therefore be linked with increasing the mixing efficiency.

To understand the development of wind turbine wakes in the atmosphere, three distinct regions of study have been proposed by the scientific community, as seen in figure 1-1: i) near wake, ii) intermediate wake and iii) far wake. The *near wake* refers to the area in the direct vicinity of the wind turbine and it typically spans from 0-4D length downstream the wind turbine. It is mainly affected by the rotor characteristics (i.e. number of blades, the blade aerodynamics, tip vortices) and the inflow conditions. It is characterized by wake expansion with a further decrease in the mean streamwise velocity and an adverse pressure gradient. In the *intermediate wake*, a shear layer develops inside and outside the effective area of the turbine. The region is characterized by unstable tip-vortices that merge into larger-scale structures. The end of the intermediate wake is defined as the streamwise distance from the turbine where the mixing layer has reached the rotor centerline. The wake structure after the intermediate wake region is driven by two main mechanisms: convection and turbulent mixing. In the *far wake* region the wake can be considered as fully developed and the recovery of the wake momentum deficit continues.

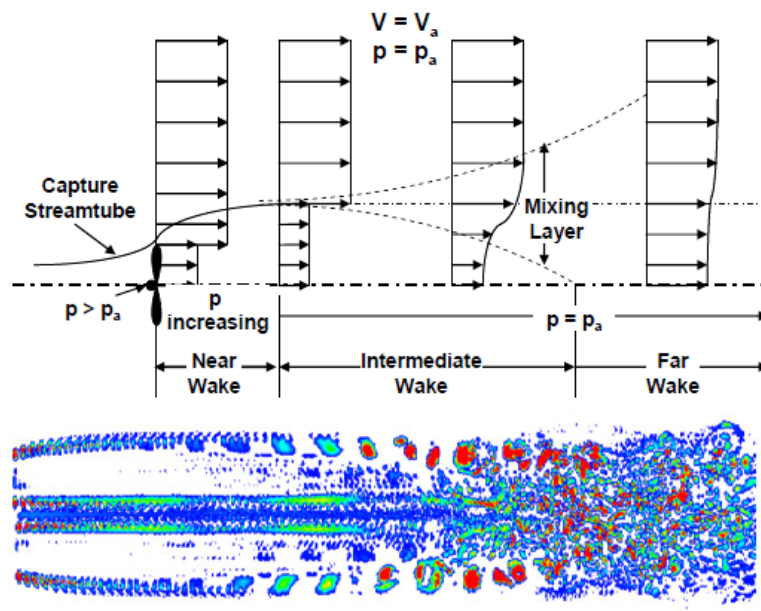


Figure 1-1: Wind turbine wake regions and mixing. The vorticity magnitude in an axial wake plane of the NREL-5MW is plotted. [1].

1-1-3 Wind Turbine Wake interactions

The power extraction for stand-alone wind turbines is due to the difference between the upstream and downstream kinetic energy fluxes. On the contrary, it is shown that for the turbines, operating in a "fully developed" wind-turbine boundary layer, the entrainment of kinetic energy from the free atmosphere into the wind turbine canopy, is the only source of kinetic energy to balance that extracted by the wind turbines [17]. The total kinetic energy that is available in the lower parts of the atmospheric boundary layer (ABL) is therefore extracted in two primary ways: from the incoming wind at the leading edge of the wind farm and from above the wind farm [18]. The changes in the streamwise direction can be neglected (after the fourth row [2]) and vertical transport of momentum becomes a crucial parameter in determining the overall efficiency of "infinitely large" wind farms³.

When talking about very large spaced wind turbine clusters new challenging questions are raised for wind energy development. Performance of the system supersedes the performance of an individual wind turbine and collective effects become important. This is the reason why the attention is shifting on research issues at the larger "farm scale" rather than the individual "turbine scale". On larger scales the dominating mechanisms that affect the wake evolution and decay are listed below:

1. ***Atmospheric conditions:*** Humidity and diurnal stability changes are shown to affect wake propagation, though the significance of the effects still needs to be accurately determined [2]. Additionally, the higher the free-stream flow speed, U_∞ , the larger the convective transport in the wake, which affects the location of the boundary between the "near wake" and "far wake" regions.
2. ***Wind Turbine loading:*** The magnitude of the energy extracted directly affects the velocity deficit of the near wake. The change in momentum is quantified with the trust coefficient for different operational speeds. The higher the thrust on the rotor the lower the wake velocity and the greater the difference between the flow velocities inside and outside the wake (shear). For very high rotor loading a considerable amount of kinetic energy of the incoming flow is converted into large-scale turbulent motion, leading to the turbulent wake state. Momentum is transferred into the wake due to the mixing of the low velocity fluid with the high velocity fluid from the free-stream flow.
3. ***Wake stability:*** Perturbations in the wind turbine operation such as yawed and sheared flow conditions typically manifest themselves in the wake flow in the form of instabilities. Recent wind tunnel and field observations [20, 21], revealed that wakes do not propagate steadily behind the rotor, but have a tendency to oscillate randomly, a phenomenon referred to as "wake meandering". The most notable changes, due to the presence of external perturbations, are in the wake pitch and rotor thrust coefficient which in turn significantly affect the steady evolution of the wake [22].

³With the height of the atmospheric boundary layer of about 1km and modern wind farms exceeding 10-20km in the horizontal direction a "fully developed" flow regime can be established. As wind farms grow larger the asymptotic limit of the "fully developed" or "infinite" wind farm has been receiving a lot of interest. This limit state is associated with wind farms on flat terrain whose length exceeds the height of the atmospheric boundary layer by over an order of magnitude [19].

4. **Cumulative effects:** As already discussed when multiple turbines are located in a wind farm, certain wind turbines operate in the wake of other turbines located upstream. Cumulative wake effects decrease wind speed as the wind travels downstream and are affected by the number of wind turbines and the complex wake interactions with the lower part of the ABL [19]. Large eddy simulations have been extensively used in the past years to quantify the effects of array layout⁴ on the performance of both onshore [23, 24] and offshore wind farms [2, 25].

1-1-4 Modelling of the wake

Modelling of a wind turbine wake is a key task for the energy yield prediction of operating wind farms as well as the optimization of new wind farm layout configurations. Numerical simulations, instead of experiments, is the main focus of the scientific community for two main reasons. Full-scale, good quality experiments are costly and are limited to provide information on the flow field. Wind flow modelling software is nowadays mainly used to extrapolate the flow field data from on-site measurements to locations where poor or no measurements were taken. Most of the modelling software used is based on either micro scale models created from measurement campaigns (linear approach i.e. WAsP, WindPRO, WindFarmer) or the Computational Fluid Dynamics (CFD) approach, where the differential governing equations of fluids are solved in a numerical way.

CFD computations of wind farms faces other difficulties. Accurate representation of both the flow over the turbine blades and the flow in the near and far wake requires massive computational resources. This is mainly due to the unsteady nature of the flow field and the turbulent length scales that range from the size of small eddies on the blades to the distance between the wind turbines. In order to capture the the different length and time scales of the atmospheric motions, over a significant number of wind turbines, domain sizes of several kilometres in the horizontal dimension are needed. This is reason why large eddy simulations (LES) of large wind turbine arrays in the ABL often use simplified models for the effects of individual wind turbines. Though less computationally intensive turbulence models are typically used in engineering applications (i.e. RANS), coherent turbulent structures in the atmospheric flows are known to dictate the vertical transport of momentum in the wake region, therefore the need to resolve those scales with LES [26]. At the moment, the actuator disc approach is the only method that can be employed to simulate the flow inside large wind farms as all the other methods are still too computationally intensive [27].

1-2 Previous work

Comprehensive reviews of turbine-wake research were published by Vermeer et al. [28], Sørensen [29] and Hansen et al. [30]. To date, though, a detailed understanding of the complex flow physics of wind turbine wakes and their interactions has not been attained. Several researchers have studied different aspects of flow in a wind farm to gain a better understanding on some of these complex flows.

⁴Array layout is characterized by the spacing between wind turbines (along and across the prevailing wind direction) and by their alignment (aligned or staggered).

(a) Ambient and turbine generated turbulence

A numerical study of atmospheric turbulence effects using large-eddy simulations on stand-alone wind turbine wakes was published by Wu and Porté-Agel (2012) [31]. High ambient turbulence intensity (TI) levels were associated with faster wake recovery. Additionally, the locations of maximum turbulence intensity and shear stresses⁵ were observed closer to the turbine relative to lower TI levels. Follow up research work [32], on the interaction between large wind farms and the ABL, revealed the importance of a wind farm layout on the flow structure and wind-turbine performance (aligned vs staggered configuration). In the numerical work of Troldborg, Sørensen et al. (2007) [33] it is concluded that the large scale motion of the wake is governed by the large eddies of the imposed atmospheric turbulence, defining both the structure and the dynamics of the downstream flow. Field measurements performed by Roy and Traiteur (2010) [34] suggest that the turbine generated turbulence can enhance the vertical mixing of momentum leading to substantial changes in the near-surface air velocity and temperature. The sources of added turbulence are formed by the tip vortices, turbulent boundary layers leaving the blades and the presence of the nacelle and tower.

(b) Stability changes of the Atmospheric Boundary Layer

Atmospheric stability refers to the capacity of the atmosphere to enhance or suppress turbulent motions. Diurnal thermal stability changes of the turbulent ABL are shown to affect the wind profiles along with the turbulence characteristics in the atmospheric boundary layer. A stable atmosphere for instance suppresses turbulent motions and is associated with high wind shear in both direction and magnitude. Full scale measurements, performed by Wharton et al. [35], attempted to quantify the effect of different stability conditions on power extracted by the wind turbines. The variability induced by changes in the atmospheric stability at a given wind speed was found to be higher under stable conditions and much lower from 15% to 20% during convective regimes. In the work of Van den Berg (2008) [36] it is argued that the thermal stability in a stable boundary layer increases the wind shear, when compared to the neutral boundary layer, yielding higher power production. The work of Magnusson and Smedman (1999) [37] focused on the transition zones, from weakly unstable to weakly stable conditions ($-0.05 < R_i^6 < 0.05$), and reported a linear increase in the velocity deficit in downwind measurements at the far wake region (up to 9D). Information about atmospheric stability conditions, are shown to be of significant importance and can be employed to improve predictions of wind speed, power production and the loads on the wind turbine components.

(c) Vertical Momentum Transport

An important contribution on the understanding of the wake flow, into large wind turbine arrays, is the identification of vertical kinetic energy entrainment as a driving factor for the performance of large wind farms. This vertical flux, or entrainment of kinetic energy has been

⁵Large shear stresses are a consequence of intense mixing in a turbulent boundary layer. They are a parameter of interest in boundary layers.

⁶The Richardson number R_i is often used to indicate stability. The following convention is used: $R_i < -0.05$: unstable stratification (daytime), $-0.05 < R_i < 0.05$: neutral stratification (overcast), $R_i > 0.05$: stable stratification (night).

measured in wind tunnel experiments [17] and large eddy simulations [19] and has been shown to balance the total energy extracted by the wind turbines. Previous research has shown the entrainment to be an important limiting factor when the flow becomes fully developed and there is a balance between the forcing of the atmospheric boundary layer and the drag of the wind turbines. The force equilibrium that characterizes a "fully developed" wake flow is reflected in the power extracted by the downwind turbines of a large wind turbine array (figure 1-2): the loss in power of the second turbine row is significant, under "full-wake" conditions, but for the successive turbines the power loss is much smaller.

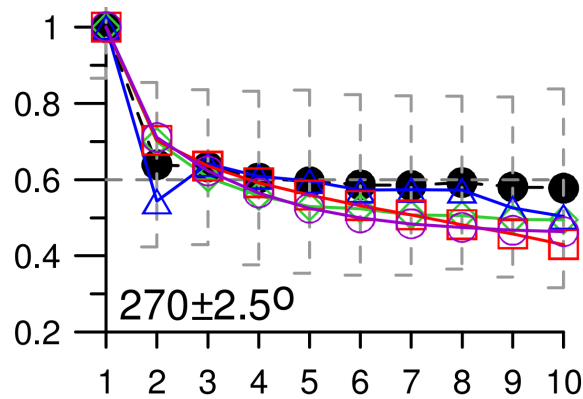


Figure 1-2: Normalized power as function of wind turbine number in a farm at a wind speed of 8m/s; different models are compared to measurements [2].

Only few have performed large eddy simulations (LES) on large wind farms. One of the most prominent works is that of Ivanell et al. [16], where two of the ten rows of the Horns Rev wind plant were simulated with periodic boundary conditions. Using the actuator disc concept with both axial and tangential inductions, he observed that in case full wake interactions the wake effect is significantly over predicted. Partial wake interaction on the other hand led to under prediction. The numerical work of Calaf et al. [19] focused more on the atmospheric sciences perspective. The aim of their work was to understand how large wind plants modify the vertical transport of momentum and kinetic energy across the atmospheric boundary layer. In the work of Cal, Hamilton et al. (2012) [38], the ABL interactions that dominate the entrainment of mean kinetic energy from the above-wake flow into the wind turbine were studied. A spectral analysis showed that large scales of flow (about the size of the rotor diameter in length) dominate the vertical entrainment. Improving the rate of vertical kinetic energy entrainment can, therefore, be achieved by modifying the large-scale structures of the flow.

In an attempt to increase power generation, in the work of VerHulst and Meneveau [39], a synthetic forcing was applied in the vertical direction to divert the wake flow and enhance wake recovery. The hypothetical forcing was assumed to be the result of modified aerodynamic wind turbine characteristics (i.e tilting, yawing), with magnitude proportional to the thrust force. It was found to have a significant effect on the overall kinetic energy flux in a large wind turbine array. Vertical mixing increased and higher velocities at the discs were reported leading to an improvement of the turbine power output.

1-3 Present work

In view of the realization that for large wind farms, it is the vertical entrainment that dominates the availability of power, we set out to study an innovative way to enhance the vertical transport of momentum. The study of new designs that could potentially assist the wake re-energizing process in wind turbine arrays, is a crucial part of the ongoing quest to improve the overall efficiency and lower the cost of energy. In the present study, the possibility to enhance the vertical transport of momentum by introducing kites in steady flight within a wind-turbine array is investigated. Large eddy simulations (LES) of a small wind turbine array operating in a turbulent atmospheric boundary layer (ABL) are used to evaluate the effect of the kites on the mean flow statistics. The LES sets are performed in a commercial CFD package ANSYS FLUENT licensed to the Delft University of Technology.

The work includes the analysis of numerous simulations that are performed in three distinct phases: 1) the atmospheric boundary layer precursor simulation, 2) the simulation of the wind turbine array and 3) the simulation of the array with the suspended kites downwind each one of the turbines. In the precursor simulation the velocity profiles and turbulence properties of the ABL are generated by the LES solver in a laterally periodic domain. The turbines are placed in the pre-generated turbulent atmospheric boundary layer (ABL) and are modelled using the traditional actuator disc concept with both axial and tangential inductions. The flow parameters of interest include the mean streamwise velocity deficit, \bar{u}/U_∞ , the time-averaged turbulence intensity levels and the mean kinetic energy transport $\bar{\Phi} = -\bar{u}(u'v')$ in downstream locations. The kites are introduced in the wind turbine array in the latter part of the report. They are modelled as body forces on the wake flow and are suspended half-way the spacing distance of the wind turbines in the array. The effect of different kite surface sizes and varying power densities on the spatial distribution of the mean kinetic energy flux in the wake region is evaluated. Extracted power values for the actuator discs and array efficiency estimations are reported for the simulated cases before and after the introduction of the kites.

The present study sets out to investigate with numerical simulations a design that was initially proposed in the 2011 Design Synthesis Exercise at the Aerospace department of TU Delft. The group of students⁷ proposed the use of a bow kite system as a cost efficient solution to increase the efficiency of the offshore wind park "Egmond aan Zee" (OWEX), see figure 1-3. The idea was based on the principle that the kite generates lift and therefore downwash⁸, bending the undisturbed flow into the wake region, yielding a velocity increase in the streamwise direction of the wind farm. Based on analytical calculations the "Daeolus kite system" generated enough downwash and achieved a 4% efficiency increase for the OWEZ wind farm. Several numerical simulations of wakes and wake interactions between four aligned wind turbines in a wind turbine array have been conducted and presented as part of this thesis work. Additionally, the effect of kites suspended inside the turbine array, on the statistics of the wake flow, is evaluated and compared to the base case; before the introduction of the kites.

⁷Credits for the original work to Group S12: Daniel Boonman, Carsten Broich, Ronald Deerenberg, Koen Groot Ash Hamraz, Roelant Kalthof, Gijs Nieuwint, Jan Schneiders, Yu Tang and Jord Wiegerink under the supervision of Wim Bierbooms.

⁸The term downwash, as used in aeronautics, is the change in direction of air deflected by the aerodynamic action of an airfoil, wing or rotor blade in motion as part of the process of producing lift [40]. The force required to create the downwash is equal in magnitude and opposite in direction of the lift force on the airfoil.



Figure 1-3: The Daeolus kite system, placed in an offshore wind farm, as conceived by the S12 group [3].

1-3-1 Outline

A brief introduction into Airborne Wind Energy (AWE) systems and high altitude wind energy extraction is presented in **chapter-2**. The two main types of power generating concepts are presented along with the formulations for the aerodynamic lift force and power generated for tethered wing sections. Before discussing the numerical work, it is important to discuss the main aerodynamic considerations and understand the physics of the flow. **Chapter-3** gives an overview of the aerodynamics of a wind turbine, including a description of the atmospheric effects that influence its operation. The blade element momentum method (BEM) is also presented since it is frequently used in many CFD codes (mainly the actuator-type methods). In **chapter-4** the computational fluid dynamics principles that any practitioner should be familiar with are presented. The most popular approaches to approximate the Navier-Stokes equations are presented. Spatial and temporal discretization schemes are presented along with the near-wall modelling approach employed in the present study. A review of the modelling approaches for the wind turbine rotors, wind turbine wakes and atmospheric boundary layer (ABL) conclude the chapter. In **chapter-5** the large eddy simulations (LES) model in ANSYS-Fluent is used to generate the atmospheric boundary layer (ABL) profiles, which were used as inflow conditions for the wind turbine array simulations before and after the introduction of the kites. The LES simulations, referred to as "precursor" runs, are used to generate the flow turbulence and velocity profiles for a neutral atmospheric boundary layer for the latter parts of the report. A full LES/Smagorinsky approach is adopted at the ground boundary surface, with specified shear stress, while no successive refinements were performed in the boundary close to the wall. The precursor simulation approach is adopted with the use of cyclic boundary conditions in the lateral faces of the computational domain, and the flow is allowed to develop for 5 successive flowthrough passes before statistics are gathered. Though only the time-averaged flow statistics are studied, LES is also considered for the wind turbine simulations since it is the model that more accurately represents the evolution and cascade

of the large scales of turbulence in atmospheric boundary layer flows. The results on the simulated wind shear profiles are presented and the ability of the code, FLUENT, to approximate the log-law of the wall is commented. The "successor" runs use the pre-generated ABL wind data in numerical simulations of a wind turbine array (chapter 6) and a wind turbine array with suspended kites (chapter 7). In **chapter-6** a wind turbine array of initially two and later on four wind turbines in a row is modelled. The wind turbines are simulated as actuator discs with both axial (ADM-NR) and tangential (ADM-R) inductions to simulate wake rotation. Different wind turbine spacing and loading factors are treated. The main interest is on the wake velocity recovery behind the discs as well the turbulence characteristics of the modified flow. In **chapter-7**, kites are suspended three rotor diameters downwind the actuator discs, $D/4$ above their top-tip height. Inter-turbine spacing of six rotor diameters is used in a four wind turbine array aligned with the streamwise wind flow (full wake conditions). The kites are simulated as body forces on the flow and are introduced in the domain as a constant discontinuous pressure jump over an infinitely thin surface; "fan" boundary condition in FLUENT. Different kite sizes [m^2] and power densities [W/m^2] are evaluated on the wake flow of four wind turbines, simulated as actuator discs with tangential induction (ADM-R), operating under partial and full loading conditions. A set of wake flow parameters (i.e. velocity deficit, turbulence intensity, kinetic energy flux) are plotted in specified locations downstream the turbines to evaluate the effect of different kite sizes and power densities on the mean flow statistics.

Kite surface aerodynamics

In search of alternative renewable energy resources the high altitude airborne wind energy (AWE) concept was born. The basic idea of extracting energy from high altitude winds using a large and fast flying kite was originally presented in the work of Loyd (1980) [41]. In contrast to wind turbines, airborne wind energy systems are either flying freely in the air or are connected to a tether on the ground. For the tethered systems power is generated in form of a traction force that drives a generator on the ground. Two main types of power generating scenarios are identified in the literature. The intermittent kite power system of attitude change and the manoeuvring or crosswind power generation system.

The first one widely known as the "**pumping Laddermill**" originates from the rotating Laddermill project (W.J. Ockels, 2001) and is presently realized as a one cable system with one or more kites that are reeled out with high force and reeled in with low pulling force (figure 2-1). During the energy generation phase the mechanical energy extracted from the wind is converted to electrical energy via a tether connected to a ground generator. In retraction phase the pulling force of the kite is minimized and the tether is pulled back using the generator as motor. There is also the possibility to use the extracted mechanical energy in a more direct way: to pump water or pull a ship. Several applications of the Laddermill system are under investigation such as the high altitude power station up to 9000m (Sky-Windpower) and the Laddermill propelled ship. The principle of "**crosswind**" motion to increase the force in the tether stems from Loyd (1980) (figure 2-2). An observation, well known amongst kite surfers, is that as soon as the kites flies in fast loops in a crosswind direction the tension in the lines increases significantly. It can be easily proven via the aerodynamic lift force F_L of an airfoil that increases with the square of the apparent flight velocity v_a calculated in equation 2-1. In the energy generation phase the pulling force can be maximized by making the kite fly crosswind on lying-eight orbits with a flight speed several times the wind speed.

$$F_L = \frac{1}{2}\rho AC_L v_a^2 \quad (2-1)$$

Since power generation from different kite flight scenarios, using a ground generator station, is not a matter of interest for the present study, the focus is shifted towards the aerodynamic

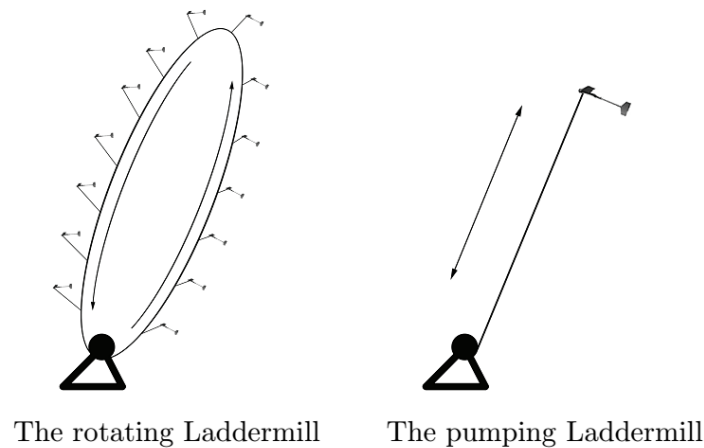


Figure 2-1: The two Laddermill concepts [4].

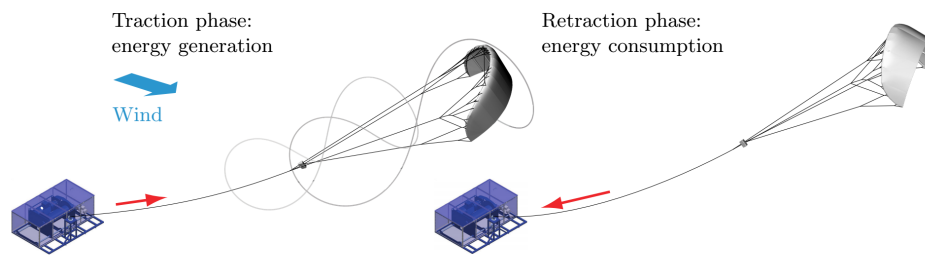


Figure 2-2: Schematic representation of the crosswind pumping cycle's traction and retraction phases for the Delft KitePower system [5].

effect of 3D wing sections in steady flight. Kites are treated in terms of the flight induced aerodynamic forces examining the possibility to divert the stream-wise flow in the vertical direction. The goal of the present study is to qualitatively evaluate the effect of the resultant aerodynamic forces on the flow due to the presence of a 3D wing section replicating the net aerodynamic forces on a kite.

2-1 3D wing aerodynamics

In a wing of finite span the pressure difference on the upper and lower parts of wings causes spillage around the blade tips accelerating the flow in the spanwise direction which sheds and rolls up. As a consequence a vorticity sheet continuously detaches from the wing and rolls up to generate trailing vortices. The pair of counter-rotating vortices generated at the wing tips alter the speed and direction of the airflow and generate a velocity downwards. The downwash induced velocity with the flow velocity results in a slightly tilted apparent velocity. As always the lift vector is perpendicular to the apparent flow which is now tilted backwards (normal force in figure 2-3) and introduces a force component in the flow direction called "induced

drag" or "drag due to lift". The induced drag, as seen in figure 2-3, is directly related to the lift generated and angle of attack typically formulated as:

$$C_{D_i} = \frac{C_L^2}{\pi AR} \quad (2-2)$$

The greater angle of attack, up to the critical angle where stall takes place, the greater amount of lift generated and greater the induced drag. For a lifting wing, vorticity is constantly being generated on the surface and shed from the trailing edge creating a wake. **Vortex drag** is the term used commonly used when referring to induced drag caused solely by trailing vortical structures.

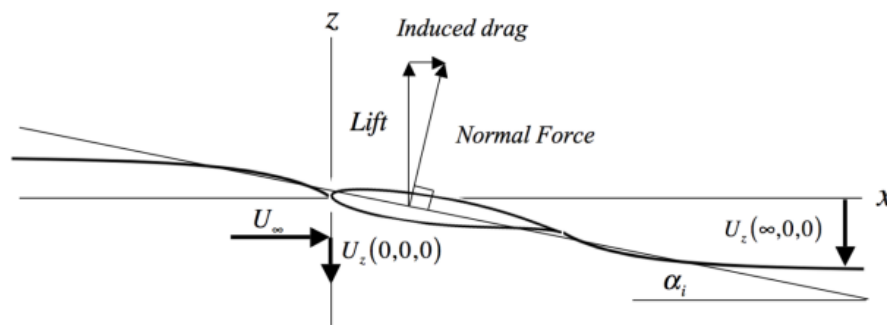


Figure 2-3: Upstream and downstream modification of the flow in the vicinity of a finite span lifting wing [6].

A two dimensional (no tips) wing section generates equal upwash and downwash [7]. In the 3D case however the downwash is greater because of the added wingtip vortices (see vortex drag). Variations in downwash along the span can produce spanwise variations in the oncoming flow ahead of the wing and thus local differences in section angle of attack. The mathematical formulation of the parameters related to wing generated downwash are briefly presented. The downward velocity component created from the vortex pairs can be identified in the free-stream ahead of the wing, at the wing as well as far downstream as seen in figure 2-4. The downward flow causes a change (decrease) in the local wing angle of attack with respect to the free stream by an amount which is known as: induced angle of attack, a_i , given by:

$$a_i = w/U_\infty \quad (2-3)$$

where: w the downwash velocity and U_∞ the free stream velocity. As a result the wing experiences the effective angle of attack $a_{eff} = a - a_i$. The downwards deflected velocity is shifted by an amount known as the downwash angle, ε , and is calculated in eq. 2-4. Resulting from the momentum theory the induced angle of attack, a_i , is related to the shape and the aerodynamic characteristics of a wing section (eq. 2-5).

$$\varepsilon = 2a_i \quad (2-4)$$

$$a_i = \frac{C_L}{\pi AR} \quad (2-5)$$

where: C_L is the finite wing (3D) lift coefficient and the aspect ratio: $AR = \frac{b^2}{S}$ with b: the wingspan and S: the wing area. Combining equations 2-3 and 2-5 we can directly relate the lift coefficient with the downwash velocity for a specified aspect ratio.

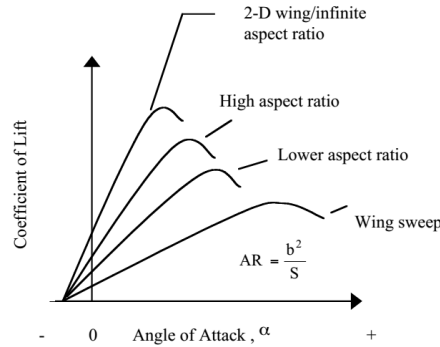


Figure 2-4: Lift Coefficient vs angle of attack for different Aspect Ratio wings. The effect of how decreasing the aspect ratio or increasing the sweep decreases the C_L/α slope [7].

2-1-1 Kite shapes & Design requirements

Different wing shapes can produce significantly different downwash distributions behind the wing and therefore different lift distributions along the span. We are going to look into a number of effects in isolation (aspect ratio, taper ratio) and conclude, if possible, on the design to yield the maximum amount of total downwash. We can easily understand from equations 2-5 & 2-3 that to reach the objective of maximum downwash velocity magnitude, the angle of attack that provides the maximum lift coefficient C_l , for any given wing section, is desired.

A low **aspect ratio** wing will in theory provide more downwash than a rival, high AR, wing since by decreasing the wing span while increasing the chord or wing area (short and stubby wing) will increase the downwash produced (eq. 2-3 & 2-5). For the aforementioned assumption to hold we should wrongfully assume that C_l can be kept constant for different ARs. As clearly presented in figure 2-4 low AR wings are much more inefficient generating less lift for a given angle of attack. For the sake of comparison therefore, assuming that the same lift is generated, the actual total downwash, w , should be the same. The only thing that changes is the distribution over the span for different ARs. A wing is called tapered when the chord at the tip is smaller compared to the chord at the root. **Taper ratio**, λ , is defined as the ratio between the tip chord (C_t) and the root chord (C_T): $\lambda = \frac{C_t}{C_T}$. The change of the generated downwash due to taper change is presented in the results of the NACA Technical Report TR 648 [42]. Given the taper and AR, $\Delta\varepsilon$ is estimated based on a range of constants, k , from the NASA report ($\Delta\varepsilon = \frac{k}{AR}$). It is shown that, for the same aspect ratio, the smaller the taper ratio (conversion of taper 1:t to a decimal taper ratio) the higher the downwash generated.

Atmospheric Boundary Layer and Wind Turbine Aerodynamics

The purpose of this chapter is to provide an overview of the most important aspects of the aerodynamics of wind turbines. A good understanding of the flow physics helps understand the choice for mathematical models. Wind turbines operate in the atmospheric boundary layer (ABL), exposed to different wind speeds, wind shears and turbulence levels. This severely complicates the calculation of the flow around them, therefore, some properties and nomenclature of the atmosphere are presented in this section.

3-1 The Atmospheric Boundary Layer (ABL)

The atmospheric boundary layer (ABL) can be visualized as the lower part of the atmosphere (1-2 km) and based on *Stull* (1988) [43] it is the boundary layer directly influenced by the presence of the earth's surface (exchange of momentum, heat and water vapour) while it responds to the earth's forcing with a time-scale of an hour or less. The velocity profile of the atmospheric boundary layer is often modelled using the logarithmic approximation.

$$U(y) = \frac{u_*}{\kappa} \ln\left(\frac{z}{z_0}\right) \quad (3-1)$$

The height of the ABL can range from hundreds of meters to a few kilometres. The definition of its height is sometimes as the distance above the earth where the flow is undisturbed (hard to define) or where turbulence disappears. Above the boundary layer the geostrophic wind is encountered, driven by the pressure gradients and influenced by the Coriolis force. The ABL height can be approximated through the relation:

$$y_{h_{ABL}} = C\left(\frac{u_*}{f}\right) \quad (3-2)$$

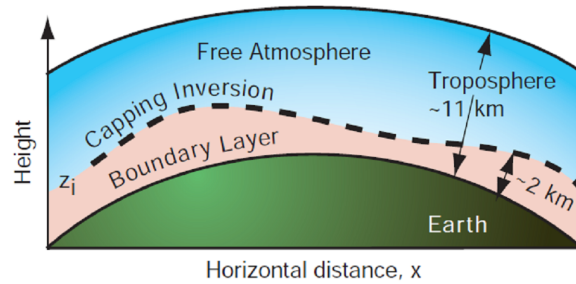


Figure 3-1: Vertical structure of the earth's atmosphere. The ABL is found in the lowest portion of the troposphere and is separated by the rest of the troposphere by a capping inversion [8]

where: u_* is the friction velocity (eq. 3-3), f the Coriolis parameter, $\tau_w = u_*^2 \rho$ is the wall shear stress, ρ the fluid density and κ the von Karman constant ($\kappa \approx 0.4$). The Coriolis force is neglected in our simulations since it is only relevant when simulating large wind farms [15]. Based on the work of Crasto (2007) [44] a value of $C=0.25$ yields boundary layer heights close to the observed daytime heights.

$$u_* = \frac{\kappa U_{h_{ABL}}}{\ln\left(\frac{h_{ABL} + z_0}{z_0}\right)} \quad (3-3)$$

3-1-1 Atmospheric Stability

Heating and cooling of the earth's surface constantly occurs throughout a 24-hour period as the daytime solar heating and night-time heat loss tend to modify the temperature distributions in the atmosphere and alter the stability of the ABL. To analyse atmospheric stability the concept of adiabatic lapse rate is useful. It is defined as the change in temperature with height for a system with no heat exchange, $(d\vartheta/dz)$, and is approximately -1°C per 100m. The following atmospheric boundary layers may be considered:

- In a neutral boundary layer (NBL) the turbulence production is dominated by the strong shear near the surface. It is most of the time a transitional state between stable and unstable conditions and is characterized by a negligible vertical potential temperature gradient ($d\vartheta/dz = 0$) between the ground and the air above.
- The unstable/convective boundary layer (CBL) is found anytime the ground is warmer than the air above (upside-down convection $d\vartheta/dz < 0$) and is characterized by enhanced turbulence kinetic energy and vertical transport of momentum. In the CBL the thermal effects are speeding up the vertical moves favouring turbulence generation.
- The stable boundary layer (SBL) results from the combination of cold surface and warm air where turbulence is generated by shear and destroyed by negative buoyancy and viscosity. Because of the competitive mechanisms of shear and buoyancy the strength of turbulence in the (SBL) is much weaker in comparison to neutral and convective

boundary layers as the thermal effects ($d\theta/dz > 0$) slow down the vertical velocity and scalar fluxes.

3-1-2 Turbulence

Atmospheric turbulence is known to be anisotropic (statistical properties independent of direction) and is a function of the surface roughness, atmospheric stability and distance from the ground. It is defined as:

$$TI = \frac{\sigma}{\bar{u}} \quad (3-4)$$

where: σ is the standard deviation of the wind velocity and \bar{u} is the magnitude of the average velocity. In principle it is formulated for each wind direction following the convention: TI_u , TI_v and TI_w .

The energy spectrum of a turbulent velocity field should be proportional to $f^{-5/3}$, in the inertial subrange, with f the frequency. For the spectral density of the longitudinal component, two expressions are typically used. The Kaimal and the von Karman spectrum both of which depend on surface roughness and height above the surface.

3-2 Actuator Disc concept

In this section the classical actuator disc theory is used to describe the operation of a wind turbine and the physics of the flow field. A number of authors have derived methods for predicting the steady-state performance of a rotor with a known blade shape and airfoil characteristics. The foundation for the development of actual wind turbines can be placed in the early 1920's originating from the work of a German physicist and pioneer Albert Betz. Betz was the first to prove the maximum amount of energy that could be extracted from the air using wind turbines.

3-2-1 One-dimensional momentum theory and Betz limit

The one-dimensional momentum theory model generally attributed to Betz, originated by R.E. Froude and W.J. Rankine (1865), was based on the linear momentum theory and was originally developed to predict the performance of ship propellers. A flow through a control volume, shaped like a stream tube, was assumed with the wind turbine being represented by an actuator disc. The actuator disc concept in a stream tube causes a pressure drop in the stream of air and is visualized in figure 3-2. The rotor predictive methods that are based on the actuator disc concept use the principle of representing the rotor with equivalent forces distributed on a semi-permeable disc of zero thickness.

To describe the AD concept we consider a control volume where the mass flow rate of air flowing through the stream-tube is constant for all stream-wise positions (figure 3-2). This means that the affected mass of air remains separate from the flow that does not pass through the rotor disc. Based on the aforementioned assumption the mass flow rate is given as

$\dot{m} = \rho AU$, where ρ is the air density, A is the rotor swept area and U_∞ is the inflow wind velocity, must be the same along the stream-tube written as:

$$\rho A_\infty U_\infty = \rho A_d U_d = \rho A_w U_w \quad (3-5)$$

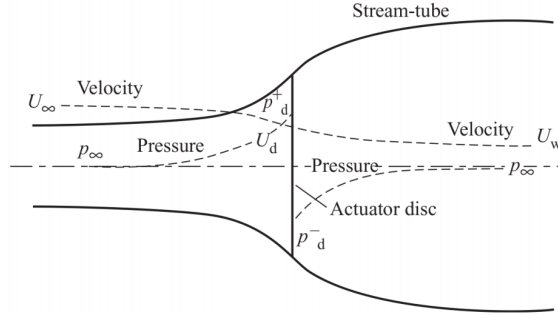


Figure 3-2: Schematic of the flow going over the wind turbine blades when modelled as an ADM [9].

U_∞ and U_w represent the inflow and outflow velocities respectively while U_d represents the velocity at the rotor disc. The classical Froude-Rankine theory considers the balance of axial-momentum far-up and downstream the rotor for a uniformly loaded actuator disc without rotation. By applying the conservation of momentum on the model and by equating the change in momentum to the thrust force (pressure drop) we obtain an equation for the calculation for the *aerodynamic power* output of a wind turbine expressed as:

$$P_{rotor} = \frac{1}{2} \rho A_{rotor} U_\infty^3 4a(1-a)^2 \quad (3-6)$$

The axial induction factor, a , is introduced as the decrease of the wind velocities at the rotor disc, expressed as:

$$a = \frac{U_\infty - U_d}{U_\infty} \quad (3-7)$$

Based on the aforementioned considerations the *thrust* and *power coefficients* C_T and C_P in terms of the free-stream, U_∞ , and the slip-stream velocity, U_w , are given as:

$$C_T = \frac{puA(U_\infty - U_w)}{\frac{1}{2}\rho U_\infty^2 A} = 4a(1-a) \quad (3-8)$$

$$C_P = \frac{\frac{1}{2}puA(U_\infty^2 - U_w^2)}{\frac{1}{2}\rho U_\infty^3 A} = 4a(1-a)^2 \quad (3-9)$$

The optimal conversion possible is proven to be for: $a=1/3$ and for a thrust coefficient: $C_T = 8/9$. Independent of their shape, wind turbines cannot extract more than 59.3% of the kinetic energy available in the air equivalent to a maximum power coefficient of 16/27 widely known as the "Betz limit".

Computational Fluid Dynamics

The need for more sophisticated methods to calculate the near and especially the far wake accurately, pushed the development towards methods that rely on the principles of conservation of mass, momentum and energy. In this chapter we will take a look at the partial differential equations governing fluid flow and their properties relevant for wind turbine applications.

When performing a numerical simulation several approaches need to be taken into account. To begin with the physical model of the flow is set which determines the set of equations to be solved. Then the volume in which the flow is simulated needs to be defined, known as the computational domain. The domain is then discretized in space and time. The computational mesh defines the spatial resolution of the numerical solution and for the temporal discretization the flow equations are approximated with either an explicit or implicit method. As the set of equations in fluid mechanics is non-linear a set of stopping criteria needs to be set to the iterative scheme. The resulting solution is finally analysed and, in case it is considered necessary, some of the previously performed steps are repeated with respect to the solution data. These steps will be discussed in the following sections.

4-1 Governing equations

Fluid dynamics is the study of fluids in motion considering the forces that bring about this motion. Computational Fluid dynamics (CFD) is the tool that allows us to solve flow problems that don't have known analytical solutions. Quoting the definition provided by John D. Anderson, Jr. (1995), "CFD is numerical solution of fluid flow problems, by replacing the partial derivatives in the Navier-Stokes equations with discretized algebraic forms, which in turn are solved to obtain numbers for the flow field values at discrete points in time and/or space". In the case of wind engineering the flow under consideration is the atmospheric boundary layer (ABL).

Computational Fluid Dynamics (CFD) analysis of wind turbines is a rather challenging task mainly because of the level and complexity of interactions occurring simultaneously from the

blade boundary layer to the interaction with the ABL and the surrounding terrain. This is the reason why the available resources need to be properly allocated and focused on the target of work.

4-1-1 Navier-Stokes equations

The equations describing the dynamic behaviour of viscous fluids are the Navier-Stokes equations. For a homogeneous, isotropic, incompressible, Newtonian fluid the equations are simplified in the form of Newton's second law:

$$\underbrace{\rho \underbrace{\frac{d\vec{V}}{dt}}_{\text{Velocity change in time}} + \rho \underbrace{(\nabla\vec{V})\vec{V}}_{\text{Convective change}}}_{\text{Mass} \cdot \text{Acceleration}} = \underbrace{\underbrace{\vec{G}}_{\text{Body force}} - \underbrace{\nabla p}_{\text{Pressure change}} + \underbrace{\mu\nabla^2\vec{V}}_{\text{Viscous Forces}}}_{\text{Forces}} \quad (4-1)$$

where: \vec{V} : represents the instantaneous fluid velocity components (u, v, w) in the three directions x, y, z [m/s], \vec{G} : the body forces in the three directions x, y, z [N/m^3] and p: the instantaneous pressure [Pa]. The Euler equations introduce a further simplification to the Navier-Stokes equations by omitting the viscous terms. The derived equations for the conservation of momentum as known as Navier-Stokes equations. In combination with the continuity equation, they can fully describe an incompressible and Newtonian fluid flow in three dimensions. In the present work we consider a flow without thermal stratification we therefore, therefore LES is based on the filtered incompressible Navier-Stokes equations for neutral flows and the continuity equation:

$$\text{Conservation of Momentum: } \frac{du_i}{dt} + u_j \frac{du_i}{dx_j} = -\frac{1}{\rho} \frac{dp}{dx_i} + \frac{d(2vs_{ij})}{dx_j} + f_i \quad (4-2)$$

where:

$$s_{ij} = \frac{1}{2} \left(\frac{du_i}{dx_j} + \frac{du_j}{dx_i} \right)$$

$$\text{Conservation of Mass (Continuity): } \frac{d\bar{u}_i}{dx_i} = 0 \quad (4-3)$$

The vectors u_i and x_i are the instantaneous velocity and position, p is the instantaneous pressure, t is time, ρ is density, s_{ij} the strain rate tensor and f_i is added for modelling the effects of the wind turbines in the momentum equation. The Navier-Stokes equations are non-linear, coupled, partial differential equations in almost every real situation therefore impossible to solve with the only exceptions being one-dimensional and creeping flows. This is the main reason why several methods have been developed to predict real flows with CFD the most popular of which are presented in the following section.

4-2 Approximate forms of the Navier-Stokes equations

The numerical solution of the Navier-Stokes equations is extremely difficult for turbulent flows mainly due to the significantly different mixing-length scales that are involved. Five of the most popular approaches in engineering are summarized below:

- **Direct Numerical Simulation (DNS):** Solve the exact Navier-Stokes equations completely. All scales of the fluid motion, spatial and temporal, are resolved by the computation (most accurately solve the NS equations, meaning that nothing is being modelled, but are too expensive for turbulent flows as the grid must be very fine and the time step very small).
- **Large Eddy Simulation (LES):** Solve the "filtered" Navier-Stokes equations. Only large scales of the fluid motion are resolved by the computations, with the smaller ones being modelled (unaffordable for solving the boundary layer).
- **Reynolds Averaged Navier-Stokes (RANS):** Solve the "time-averaged" Navier-Stokes equations. Only the mean flow is solved and all eddies are modelled (predicts mean flow structures, efficient in the boundary layer but excessive diffusion in the separated region).
- **Unsteady RANS (URANS):** Introduces a temporal filter defined by the time step in the analysis in order to capture the longer period flow features. Simulates the unsteady nature of the wind field and does a much better job in simulating pressure distributions and wind loads when compared to RANS.
- **Detached-Eddy Simulation (DES):** Hybrid method where the boundary layer is resolved using URANS while the core/separated regions are resolved using LES.

The choice of turbulence model mainly depends on the type of flow, the required accuracy level and the availability of computational resources. In theory it is possible to compute all the turbulent length scales via direct numerical simulations (DNS) since turbulent flows are fully described by the Navier-Stokes equations. For high Reynolds flows however, DNS is not an option as the computational cost is proportional to Re^3 . Instead of computing all turbulent length scales one could only resolve the large eddies (LES), larger than the filter scale (relative to the grid size), while the effect of the smaller scales is parameterized using a sub-grid-scale (SGS) model [45]. It requires much greater computational resources and therefore is not commonly used in the wind industry at the present point. It is considered to be superior than RANS in terms of accurate representation of the vortical structures that are in the energy containing range of interest. The LES model is also unsteady meaning that the solution is calculated over a range of time steps as opposed to the averaged single time step of the RANS approach. The main discretization is based on the level of resolved vs. modelled turbulence scales, as seen in figure 4-1. The more turbulent scales modelled the less the computational cost with the trade-off of reduced accuracy.

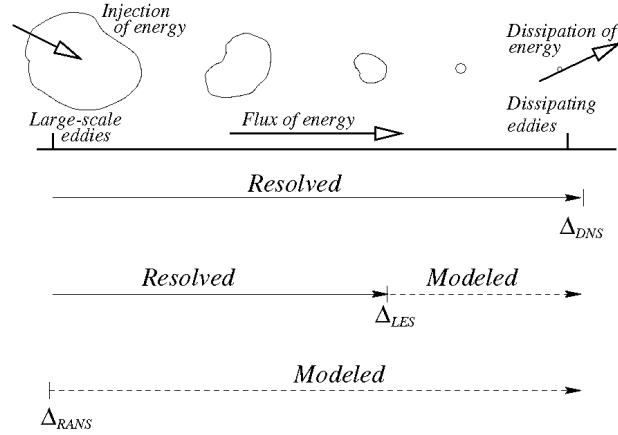


Figure 4-1: Resolved vs modelled turbulence scales for RANS, LES and DNS models.

4-2-1 Large eddy simulations (LES)

In LES the larger scales of motion are directly computed in the GS part while the eddies below the specified filter size are modelled using an SGS model. When the length scales dominating the flow are in the higher end of the energy range it is considered that LES works extremely well and provides accurate results. Wind power generation is predominantly affected by the larger scales of the flow and thus LES is considered suitable for the simulation in the following sections. The first step in a LES simulation is the filtering operation which filters out the eddies smaller than the filter scale while it retains the larger eddies. The filtering of any variable ϕ is defined as convoluting the function with a filtering kernel:

$$\bar{\phi}(x, t) = \int_{Domain} \phi(x', t) G(x, x', \Delta) dx' \quad (4-4)$$

where: $G(x)$ is the filtering kernel in physical space. The cut off width is often taken as $\Delta = \sqrt[3]{(\Delta x \cdot \Delta y \cdot \Delta z)}$ where Δx , Δy , Δz are the grid sizes for the domain axes respectively. After the filtering process the momentum equations are computed where the interaction between the larger eddies (resolved scales) and the smaller eddies (modelled eddies) is contained in the subgrid stress $\tau_{i,j}$. The effect of the unresolved SGSs is parametrized with the eddy viscosity assumption of the Smagorinsky-Lilly closure scheme:

$$\tau_{sgs} = -2l^2(2S : S)^{1/2}S \quad (4-5)$$

with $S = (\nabla \bar{u} + (\nabla \bar{u})^T)/2$ the strain-rate tensor and l the characteristic length scale for the eddy-viscosity.

4-3 Discretization

The partial differential equations that describe the flow need to be discretized, meaning the local derivatives within the flow equations are transformed into finite values on a finite number of computational points. It is important to distinguish between two types of discretization: the spatial and the temporal discretization. In the space discretization we are replacing the spacial continuum by a finite number of points or cells where the numerical values of the variables can be determined. The spatial discretization results in the generation of a grid describing the domain at certain points. The temporal discretization is used to transform the temporal derivatives into finite time steps and is only used when simulating unsteady or time-dependent flows.

4-3-1 Spatial Discretization

Grid generation and grid quality are essential elements of the discretization process and of utmost importance for CFD simulations. It is the most critical element in the cost of CFD simulations and more importantly the mesh quality critically effects the accuracy of the obtained numerical results. The accuracy is related not only to the size but also to the form of the mesh. As the size of the cells goes to zero (infinite number of cells) the discretization error will also go to zero. To ensure a good quality mesh the aspect ratio, skewness angle and smoothness or stretching ratio of the grid cells must be checked. Aspect ratio is a measure of stretching of the cell and is defined as the ratio of the maximum distance between the cell centroid and face centroids to the minimum distance between the nodes of the cell. A value of 1 indicates no deviation from the optimal shape which is the recommended practice for CFD simulations. Skewness determines how close the grid cells are to an equilateral cell with values ranging from 0 (equilateral) to 1 (degenerate). Rapid changes in cell volume between adjacent cells is a case of low smoothness that translates into larger truncation errors¹.

In terms of space discretization we distinguish between a structured and an unstructured grid. The structured grid is a grid with regular topology where neighbourhood relation between the points is given by a one-, two-, or three-dimensional array. On the other hand an unstructured grid is a grid with irregular topology (figure 4-2). Another distinction is made relative to the sizing difference between adjacent grid cells. The uniform grid is characterized by equal spacing between grid points and the non-uniform grid with unequal spacing between grid points. Structured grids with either uniform or non-uniform arrangement are preferred when considering CFD simulations.

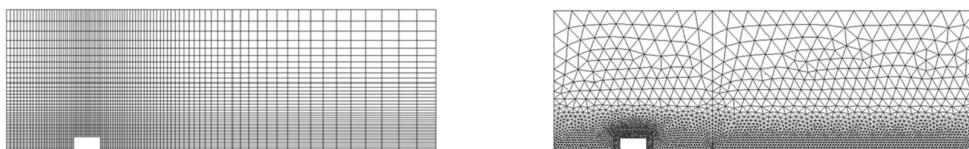


Figure 4-2: (Left) Non-uniform Structured Grid, (Right) Non-uniform Unstructured Grid

¹Truncation error, in numerical integration, is the difference between the partial derivatives in the governing equations and their discrete approximations. It is a function of the grid quality and the flow gradients.

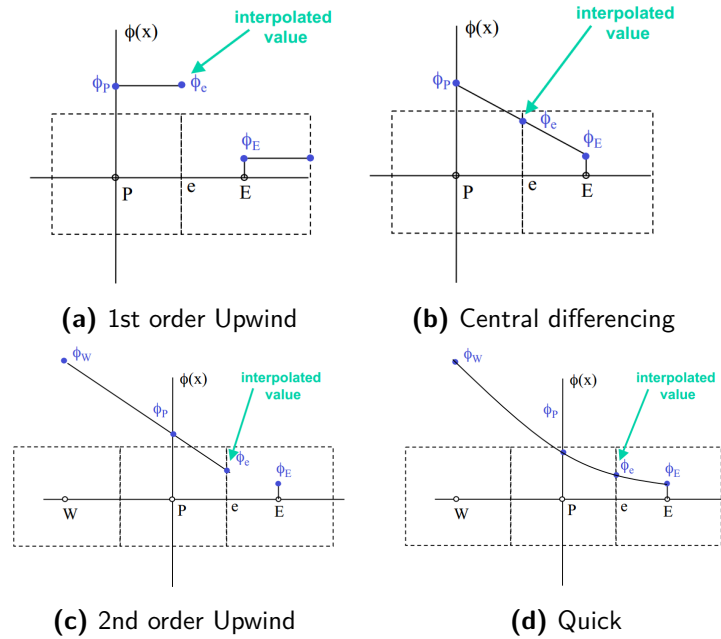


Figure 4-3: Discretization of the convective terms (flow direction from left to right)

There are three common discretization approaches: the finite difference (FD), the finite volume (FV) and the finite element (FE). The finite volume method has been employed in many commercial CFD packages, including FLUENT, where the solution domain is subdivided in a number of control volumes (CVs) surrounding each node point (centroid of one CV) in the computational grid. In the finite volume method the values of the flow variables at the faces of one control volume need to be obtained in terms of the centroid values of all its neighbouring cells by suitable interpolation schemes. The simplest of the interpolation schemes, is the first-order upwind interpolation scheme (figure 4-3a), use the upstream cell values (φ_P) to calculate the face value (φ_e). The face quantities are identical to the upwind cell quantities and are associated with faster computations and lower level of accuracy. The second-order upwind scheme (figure 4-3c) uses the cell-centred value and the gradient within the upstream cell ($\nabla\varphi$) to compute the face value of φ . When using the LES turbulence model a second-order central difference discretization scheme is available. A third major scheme is called QUICK (figure 4-3d) and is a 3rd order differencing method where the face value φ_e is calculated based on the cell-centred values of the cell immediately upstream (P) and the second cell upstream (W).

4-3-2 Temporal Discretization

The temporal derivatives (rate of change of parameter φ with respect to time $[d\varphi/dt]$) within the flow equations need to be discretized when interested in simulations involving unsteady or time-dependent flows. The flow quantities are therefore calculated by dividing the simulated time into discrete time steps. Several methods exist for this process that can be mainly divided into two classes: the *explicit* and the *implicit* discretization. The explicit methods calculate the state of a system at a later time step based on the state of the system at the

current time. The simplest explicit time scheme is the explicit or forward Euler method which is expressed as:

$$\varphi^{n+1} = \varphi^n + f(t_n, \varphi^n)\Delta t \quad (4-6)$$

The explicit Euler method has a first order accuracy and belongs to the class of two-level methods as two time levels are involved the current state (n) and the state at the later time (n+1). The main problem of the method is that it becomes unstable if the time step Δt is chosen too large.

The implicit discretization class, in contrast to the explicit method, calculates the state of a system at a later time step based on the slope of the future value. The simplest implicit time discretization method is the implicit or backward Euler method expressed as:

$$\varphi^{n+1} = \varphi^n + f(t_n, \varphi^{n+1})\Delta t \quad (4-7)$$

The values of the next time step are not known yet and therefore have to be handled as additional unknown variables of the equation system that is solved first. The major advantage of implicit methods is that they are not sensitive to the size of the chosen step. The solving process of one time step may be slower compared to the explicit methods, due to the additional computational effort, though the overall scheme is often faster as they require fewer time steps for convergence.

Temporal and spacial discretization are related through the Courant Number:

$$C = \frac{\bar{u}\Delta t}{\Delta x} \quad (4-8)$$

To avoid convergence issues the time step (Δt) is chosen such as the Courant number is typically <1 . This effectively means that the fluid particles travel a distance, during one time step, which is no longer than the grid size (Δx).

4-4 Near-wall treatment for LES

The law of the wall for the inner part of a turbulent shear flow was first published by Theodore von Karman in 1930 and is a simple analytic function for the mean velocity distribution, the logarithmic law. It states that the average velocity of a turbulent flow at a certain point is proportional to the logarithm of the distance from that point to the wall (applicable to $<20\%$ of the height of the flow). Boundary layer flows are generally divided in the inner wall region (important viscous effects) and the outer region away from the wall. For high Reynolds number flows, resolving all the small-scale eddies is too computationally demanding therefore the need for a technique to abandon the calculation of the near-wall flow. In the present study no near-wall functions were employed and full LES with the Smagorinsky SGS model were used without any grid refinement in the ground boundary. A simplified near-wall modelling approach that was used to evaluate the capability of the code to approximate boundary layer flows.

4-5 Modelling of the rotor

When modelling wind turbine arrays, in CFD, the Actuator Disc [46, 47] and the Actuator Line [48, 49, 33] methods are typically used while the Actuator Surface [50] model has only been recently explored. Full rotor simulations, due to much finer resolution around the turbines, are extremely computationally intensive and provide accurate resolution to the near wake which is not of major importance when studying large scale wind farm flows. The force that the actuator disc/line exerts on the flow is added to the momentum equation,

$$\frac{D\mathbf{u}}{Dt} = \mathbf{f} - \frac{1}{\rho}\nabla p + \nu\nabla^2\mathbf{u} \quad (4-9)$$

In the **Actuator Disc (AD)** model, the rotor is simulated as a semi-permeable disc, while the induced forces on the flow are calculated based on the local aerodynamic lift and drag coefficients of the blade (airfoil data). Variations of the AD, found in the literature, include the definition of thrust and tangential forces (ADM-R) while others only thrust (ADM-NR). The ADM may simulate wind turbines and the induced wakes but fails to create the tip vortices carried onto the wake [48]. For this reason Wu and Porté-Agel (2013) [32] performed LES simulations of wind farm in order to compare the results obtained from the ADM-NR/ADM-R with turbulence measurements collected with hot-wire anemometry. It was noted that generally the ADM-R yields improved predictions in the wake of all wind turbines relative to the ADM-NR, stressing the importance of turbine-induced flow rotation in the prediction of the wake structures. A more refined approach relies on forces distributed along rotating lines. The **Actuator Line (AL)** models do not resolve the full geometry of wind turbines, and are modelled as a set of blade elements (lines) along the blade axis. Significantly smaller mesh sizes are required which usually makes impractical for advanced turbulence models with large domain sizes. In the work of Ivanell (2009) [16] the wind turbine wake using the Actuator Line was studied using direct numerical simulations (DNS). The mean velocity results and turbulence characteristics reported in the Ph.D. thesis of Troldbord (2008) [48], using the AL model, were in good agreement with the field measurements performed. In the **Actuator Surface(AS)** model, the forces are calculated based on empirical formulas on a 2D-airfoil, as a function of the chord, therefore avoiding one of the main simplifications of ALM. The application of an actuator surface model is discussed in the work of Dobrev (2007) [50] and the results were compared with the NREL Phase VI experiment data showing satisfying agreement.

4-6 Modelling the Atmospheric Boundary Layer (ABL)

When performing CFD simulations a key issue among wind engineers is the accurate representation of the turbulent Atmospheric Boundary Layer (ABL). One of the most popular two-equation turbulence models is the k- ϵ model where two coupled transport equations for the turbulence kinetic energy, k, and the dissipation rate, ϵ are solved. It has been successfully applied to large range of different applications ranging from: wind flow around structures [51], urban environments [52], and flow over flat and complex terrain [53]. The performance of the model however largely depends on the choice of model constants while large differences

are reported in the literature [54]. LES are generally shown to reproduce main turbulence properties with higher accuracy, when compared to standard RANS type models, though it is stressed that further research is needed in sub-grid scale modelling [55, 56]. Xie and Castro (2006) [57] presented a comparison of LES, RANS and DES for a flow over wall mounted obstacles showing the superior performance of LES within the canopy. Dejoan et al. (2010) [58] compared RANS and LES for pollutant dispersion and concluded that LES performed better in the prediction of the vertical velocity and Reynolds shear stress, whereas the results for the streamwise velocity were comparable.

One of the major difficulties, encountered in LES, is the definition of realistic upstream conditions at the domain inlet. Several inflow generation techniques have been proposed in the past decade and can be classified into three main categories: synthetic methods, precursor simulations and recycling methods. A basic **synthetic** method is to generate turbulent inflow data is to superimpose random fluctuations on a mean velocity profile. The generated data do not exhibit and spatial or temporal correlations and the energy generated is uniformly spread over all wave numbers [59]. One of the more realistic turbulence, with better spatial and temporal correlations, is to run a precursor simulation either before the main simulation or simultaneously with it, usually by extending the domain upstream the area of interest. In the **precursor simulations or "mapping" methods** (described in [60]) a part of the precursor domain is combined into the main computational domain and the flow variables are sampled on a cross-plane far downstream the inflow plane. The sampled data are then recycled back to the inflow plane at each time-step. Another well established procedure, often used in LES of experimental configurations, is to generate inflow boundary conditions from the knowledge of the bulk velocity and swirl number otherwise known as **recycling or matching database** method. Imposed wind shear profiles by applying momentum sources in each computational cell was initially introduced in the publication of Mikkelsen and Sørensen (2007) [49] and later on adopted in work of Ivanell and Sørensen (2007) [16]. The turbulence field is pre-generated based on Mann's method (Mann 1994) [61] (time-varying body forces on the flow) and is imposed at the inlet of the computational domain. Superimposing, though, the wind shear, direction, speed and stability does not guarantee correct ABL statistics since those parameters are physically correlated [62].

Numerical simulations of the Atmospheric Boundary Layer (ABL)

To generate the numerical wind, the LES model coupled with the Smagorinsky - Lilly sub-grid-scale (SGS) model available in FLUENT was used. In the numerical simulations two main assumptions are made to simplify the analysis of the ABL motion. Firstly, the ABL is considered neutrally stable meaning that thermal effects are neglected. For our test case it is considered as a valid assumption as we are interested only in highly turbulent flows where the mixing produced by mechanical turbulence far outweighs the moments developed due to thermal effects. Since the purpose of the study is to provide a qualitative report of the examined test cases, the assumption of a neutral ABL saves computational time since the additional equation for the transport of potential temperature does not need to be solved. The second one is of incompressible wind flow, valid for low Mach number flows ($Ma < 0.3$) where the flow is (quasi)steady and isothermal meaning that compressibility effects can be neglected.

5-1 Numerical wind flow

The numerical wind was created in an empty domain (without wind turbines) from now on referred to as the "precursor" simulation. Precursor simulations along with periodic boundary conditions are typically used in the literature to generate the ABL turbulence based on known ground roughness characteristics [63, 64, 65]. In the precursor ABL simulation the flow is recycled in the domain allowing the boundary layer and its turbulence to naturally develop. Once the flow approaches the logarithmic profile, corresponding to the predefined mean velocity and ground roughness characteristics, the flow profiles are recorded at a specified vertical plane for three to four flowthrough passes. The flowthrough time is defined as $t_{pass} = L/U_0$, where L is the length of the computational domain and \bar{U}_∞ is the mean inlet velocity. The recorded wind profiles (x,y,z velocity components) are saved for each time-step and fed as inflow conditions for all successor simulations of the wind turbine array. Wind

farm simulations strongly rely on accurate wake-ABL interaction which is possible only with a correct ABL model. Synthetic methods to generate the ABL, allow the simulation of fully developed infinitely wind farms, without requiring a large domain using periodic conditions in the lateral boundaries. They require lesser computational effort than precursor simulations but lack the statistical correlations of a physical ABL. Pre-generated or precursor ABL profiles require additional computational effort and disc space requirements to save the wind data but provide more physically sound representation of the ABL. A comparison of the more commonly used methods to generate the ABL is found in section 4-6.

In order to generate the fluctuating velocity components in the computational domain the spectral synthesizer method is employed in FLUENT. The synthesized turbulence method is used in our case, to provide the initial "kick" and initiate motions in the flow. For a velocity inlet boundary condition, a random field of fluctuating velocities (based on a random flow generation (RFG) Fourier technique proposed by Smirnov, Shi et al. (2001) [66]) is superimposed on a specified mean velocity.

Table 5-1: Simulated wind and roughness parameters

Mean wind speed [m/s]	\bar{U}_∞	8.5
Temperature [K]	T	288.16
Pressure [Pa]	P_0	101325
Turbulence intensity	TI	12%
Coriolis parameter [s^{-1}]	f	0.00016
Wall shear stress [Pa]	τ_w	0.394
Aerodynamic roughness length [m]	z_0	0.1
Density [kg/m^3]	ρ	1.225
Von Karman constant	κ	0.40
Friction velocity [m/s]	u_*	0.45
Kinematic viscosity [m^2/s]	ν	0.0000179

5-1-1 Spatial discretization

The requirements for mesh resolution are typically based on the assumption that the largest relevant turbulent scales are similar in size to the width of the instability zone [67]. For a bluff body, with diameter D, the minimum resolution required should be of the order: $\Delta_{max} \leq 0.05D$ [67]. Since the simulations to generate the wind profiles are realized in an empty domain the meshing requirements are now specified based on the diameter of the wind turbines that will be introduced in the follow-up simulations and will be the main sources of instability in the flow. Based on the aforementioned convention, for an 80m diameter wind turbine, the proposed uniform cell's dimensions would have been 4x4x4m. Ivanell [16] uses a mesh with resolution of roughly 4m with a local 2m resolution near the turbines. Based on the availability of the computational resources it was determined that, to generate the wind flow, a grid with uniform grid resolution of 8m would be a good starting point; compromise between computational load and resolved turbulence length scales (filtering length in LES is based on the local spatial-discretization). The 8m grid spacing, will from now on, be referred to as the D/10 grid sizing, with D=80m the diameter of the reference wind turbine used in the simulations of the following chapters.

5-1-2 Computational domain

The computational domain dimensions should be selected to represent the ABL without constraining the energy carrying turbulent structures. For neutral boundary layers the domain height scaled according to the u_*/f_c where u_* is the friction velocity and f_c is the Coriolis parameter. The proportionality constant is typically taken as 0.3 meaning that the domain height is given as: $H = 0.3u_*/f_c$. For a friction velocity of 0.45 and Coriolis frequency $f=1.6e-4$, the domain height is estimated at 800m. For fully turbulent channel flows the "Best practice guidelines" [67] when periodic conditions are used in the later boundary layers a sufficient length of the domain is required (at least 8-10h, where the boundary layer thickness: $h=H/2 \Rightarrow L_x=3200m-4000m$) to allow the formation of turbulence structures independent of the periodic boundaries. Based on their recommendations [67] for simulating turbulent structures in periodic channel flows a domain size of $4H \times 1H \times 1.5H$ ($L_x=3200m \times L_y=800m \times L_z=1200m$) would suffice. Based on the already determined computational cell size ($8 \times 8 \times 8$) the domain cells were calculated about 6m based on $N_x \times N_y \times N_z$ ($400 \times 100 \times 150$) grid points.

Table 5-2: Domain size and mesh specifications

Domain dimensions	L_x [m]	2000
	L_y [m]	800
	L_z [m]	800
Number of Nodes	N_x	250
	N_y	100
	N_z	100
Computational cell length	Δx [m]	8
	Δy [m]	8
	Δz [m]	8
Total number of cells		2,500,000

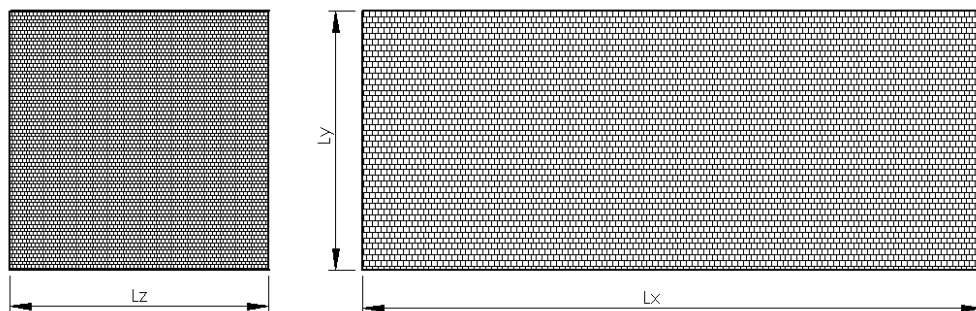


Figure 5-1: Sizing and impression of the spatial discretization of the computational domain used in the ABL simulations

To summarize, the LES simulations are performed in a domain of $2.5H \times 1H \times 1H$ ($L_x=2000m \times L_y=800m \times L_z=800m$) with a grid spacing of $N_x \times N_y \times N_z$ ($250 \times 100 \times 100$). Ideally

the domain in the streamwise direction, L_x should be $4L_y-6L_y$ with L_y the domain height; determined by the height, H , of the atmospheric boundary layer. This ensures that no spatial correlations due to the presence of the periodic boundary conditions are preserved along the domain fetch. A smaller domain was chosen to limit the computational costs, since in the present study, we are mainly interested in a qualitative comparison of the wake flow parameters before and after the introduction of the kite system. The domain size is application dependent and for the present work the recommendations of Hall (1997) [68] have been followed. The computational time required, with the same type of processors and simulation parameters, for the 2.5m cell domain was 30 hours for a single flow pass through the domain. An approximate of 10 days were needed to generate the inflow conditions, for the successor simulations, on the cluster of the Aerodynamics Research Group @ TU Delft utilizing 10 x Intel Xeon E5-2670v2 CPUs using 4GB of RAM/core. The effect of the domain size and grid spacing on the accuracy of the solution is investigated in chapter 6.

5-1-3 Numerical settings

The LES model with the Smagorinsky model was used to simulate the turbulent flow since, under certain conditions (Smagorinsky constant not too high, spatial grid and time step not too large), it provides more realistic results than conventional models. An exact value for the Smagorinsky constant C_s does not exist, since it is known to vary with application, with values reported in the literature from 0.1 to 0.25. The default value of $C_s=0.1$ in FLUENT was used to avoid unwanted dissipation of small scale turbulence (in duct flows values in excess of 0.12 have been known to suppress turbulence completely). The solver settings are adjusted based on the available documentation: "Best Practice - Scale-Resolving Simulations in ANSYS CFD" [67]. Based on their reported verification studies, to achieve low numerical dissipation, LES is carried out using Central Difference (CD) schemes. For the spatial discretization of the convection terms a second order upwind scheme was employed though a first order scheme would also be sufficient (the models are dominated by their source terms). For skewed or polyhedral meshes it is recommended to use the Least Square Method (LSM) for the spatial discretization gradient. For the pressure terms, the PRESTO scheme should be avoided, since it is more dissipative than the other options, therefore the standard pressure interpolation was used. Time integration is carried out with the Second Order implicit Euler scheme as proposed. An implicit time integration scheme is used which is stable for any time step size. Due to the uncertainty of the time-step a time-step dependence study is typically performed to evaluate the numerical error associated with larger time-steps. Due to the extra computational costs associated with smaller time-steps, a temporal convergence study was not considered in the present work. For explicit schemes, the Courant-Friedrich-Levy (CFL) criterion needs to be satisfied, $C = \frac{u\Delta t}{\Delta x} \leq C_{\max}$ though the requirement in our case is a rather low time step to minimize numerical dissipation which is known to affect the evolution of turbulence in LES. For all the precursor simulations, the time discretization is second-order implicit with a time step: $\Delta t=0.1$.

5-1-4 Boundary conditions

At the top side of the computational domain a symmetry boundary condition is used ($du/dy=0$, $dv/dy=0$, $dw/dy=0$). Since no fluxes are allowed to cross, the top boundary needs to be placed

Table 5-3: Solver settings

Viscous model	Model	LES
	SGS model	Smagorinsky-Lilly : $C_s=0.1$
	Pressure-Velocity coupling	SIMPLE
Solution methods	Spatial discretization	Gradient : Least Squares Cell Method
		Pressure: Standard
		Momentum: BCD
		SGS Kinetic Energy: BCD
	Transient Formulation	Second Order Implicit
	Time step size	$\Delta t = 0.1s$

away from the surface to ensure that no pressure waves induced by the surface topography or obstacles are reflected back into the flow. At the bottom surface an imposed wall stress boundary condition relates the wall stress to the velocity at the first gridpoint using the standard log-law. The shear specified as $\tau_w=0.394$ Pa represents the drag generated by the roughness of the surface and corresponds to that of a crop-land with $z_0=0.1m$. By specifying a shear at the wall boundary, instead of a no-slip condition, clears the need for refinement of the cells close to the wall to resolve the boundary layer at the ground surface. For fully resolved LES, the first cell normal to the ground should obey the $y^+=1$ guideline to properly resolve the boundary layer. Based on the Reynolds number expected for the simulated flow the $y^+=1$ requirement for LES corresponds to a wall spacing distance of 0.00005m which is not feasible in terms of computational cost for any CFD simulation.

For the first flowthrough pass, only, the boundary conditions for the inlet/outlet of the domain are set to velocity inlet/outlet. This was a necessary step, in the turbulent wind flow generation process, since the Spectral Synthesizer method in FLUENT is only made available when coupled with velocity/pressure inlet/outlet BCs. After the first flow pass all the lateral boundary condition (inlet/outlet and sides) are changed to periodic (cyclic) and the simulation is allowed to run until the boundary layer is considered to be fully developed. To characterize the development of the boundary layer, the statistics of the main flow parameters for each flow pass were gathered and compared; the simulation was stopped as soon as minimal changes in the flow characteristics (velocity and turbulence profiles) were observed. A constant pressure gradient is imposed in the flow direction to drive the precursor simulation after the initial flow pass. It is calculated as: $d \langle p \rangle / dx = -\rho u_*^2 / H$, with H the height of the computational domain. The domain boundary conditions used for the presented simulation results are summarized in Table 5-4.

5-2 ABL simulation results

In this section three turbulence statistics are evaluated in prescribed downstream locations to characterize the wake flow: i) streamwise velocity, ii) total turbulence intensity, iii) dimensionless wind shear. The results presented in the following figures are based on the flowing conventions. The flow is allowed to develop for five successive flow passes until time-statistics

Table 5-4: Precursor simulation boundary conditions. The flow in the streamwise direction is driven by a specified pressure gradient, specified in the periodic BC's tab, for the successive flow passes.

Boundary face	BCs [first flow pass]	BCs [successive flow passes]
Inlet	Velocity inlet	Periodic
Sides	Periodic	Periodic
Outlet/Exit	Outflow	Periodic
Terrain	Wall with specified shear	Wall with specified shear
Top	Symmetry	Symmetry

are gathered. The velocity profiles plotted in the following figures are time averaged for the for each flow pass through times as well as horizontally averaged over the length of the domain over the specified time frame. The presented flow statistics for each one of the successive flow passes are therefore not affected by the previous ones.

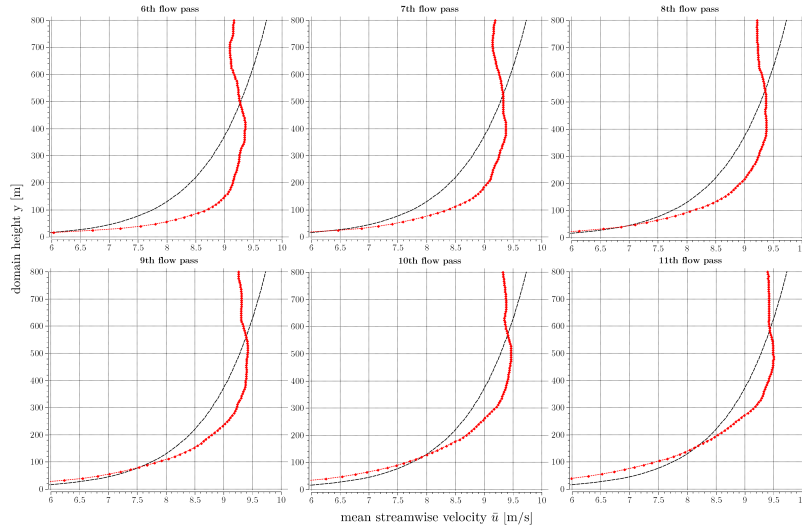


Figure 5-2: First order statistics: Vertical streamwise velocity profiles developed in the precursor simulation. Time averaged statistics for each flow pass after the 6th are presented. The black dashed line represents the target log-law profile for the given ground roughness characteristics.

The excessive velocity gradients close to the surface layer, see figure 5-2, have been previously reported in the literature and is known as a traditional problem in LES simulations of the ABL [52]. The decay of the velocity profile with distance along the fetch of the domain is visible and is in line with the results presented in the work of Riddle et al. [52]. Based on the numerical work of Richards and Hoxey [69] a shear stress should be applied at the top of the domain, an important requirement, to sustain the ABL profile through the length of the domain. The 8th, 9th and 10th flow passes are the ones to closely approximate the logarithmic law at the area of interest for the successor simulations. The area of interest extends from 40-120 meters (80m hub height) for the simulations including the wind turbines (chapter 6) and from 40-140 meters for the simulations with the kite surface (chapter 7).

In the work of Mason and Thomson (1994) [70] it was demonstrated that the standard

Smagorinsky model coupled with wall functions is unable to accurately capture the logarithmic velocity profile. In LES the dissipation characteristics of the Smagorinsky model have a direct impact on the turbulence kinetic energy on the resolved field which has a direct influence on the mean velocity profile.

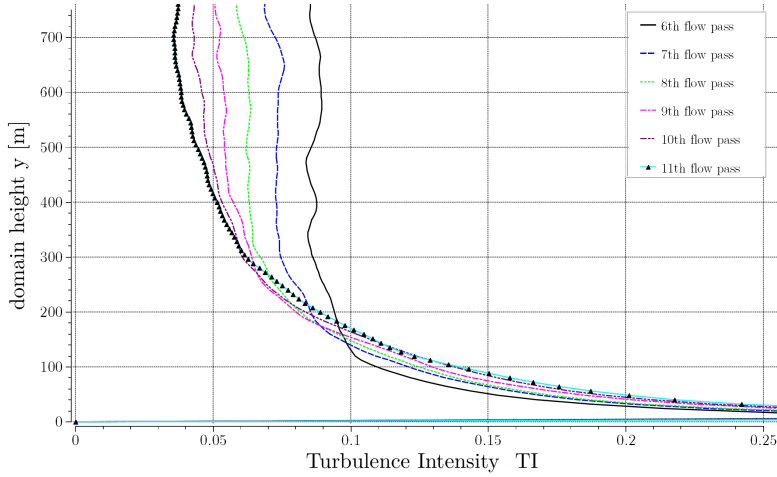


Figure 5-3: Second order statistics: Vertical profiles of turbulence intensity developed in the precursor simulation. Time averaged statistics of TI for each successive flow pass, spatially averaged in the streamwise direction.

The turbulence intensity profiles as they develop in the successive flow passes are presented in figure 5-3. An average turbulence intensity of 12% is developed at the domain height where the wind turbines will be placed in the successor simulations. Again no horizontal homogeneity in the turbulence characteristics is obtained in line with the problems reported in the work of Franke and Frank (2005) [71] and Blocken and Carmeliet (2006) [51] using FLUENT 5 and FLUENT 6.

In neutrally stratified flows, the peak normalized velocity variances are of the magnitude $\sigma_u^2/u_*^2 = 5 - 7$, $\sigma_v^2/u_*^2 = 3 - 4$, $\sigma_w^2/u_*^2 = 1 - 2$ [66, 72]. The max horizontally averaged values for the normalized total velocity variance falls within the range for the x- and y-velocity components ($\sigma_u^2/u_*^2=6.5$ and $\sigma_v^2/u_*^2=3$) and is out of range for the z- velocity component.

For LES simulations the dimensionless wind shear Φm is calculated from the horizontal and time-averaged profile of wind speed and is often used to measure the ability of computational solvers to capture the mean velocity profiles. The non-dimensional velocity profile is plotted in a semi-log plot and visualized in figure 5-4. Assuming therefore that the mean wind shear, $d < M > /dy$, only depends on friction velocity, u_* , and the height above surface, y , we get from dimensional analysis:

$$\Phi m = \frac{ky}{u_*} \left\langle \frac{dU}{dy} \right\rangle \quad (5-1)$$

Neutral ABL simulations with the standard Smagorinsky model had been performed in the work of Mason and Thomson (1994) where an overshoot in velocity was reported and values of the normalized wind shear Φm reaching a maximum of 2. The same trend is observed

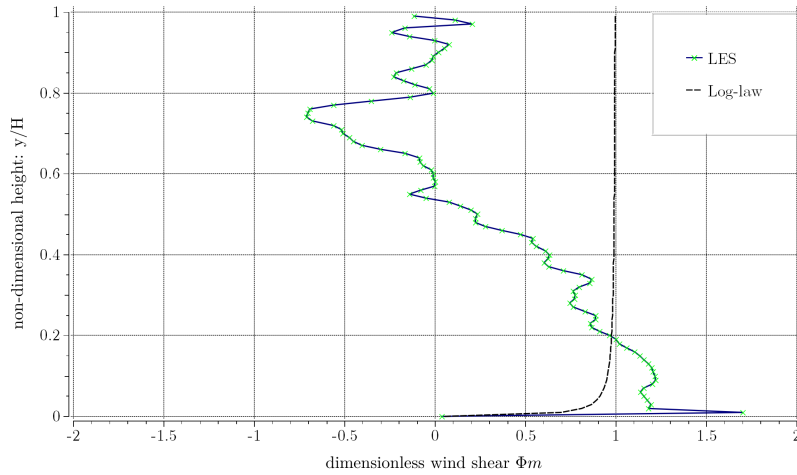


Figure 5-4: Non-dimensional velocity profile in a semi-log plot. The classical log law is represented with the black dashed line while the numerical results for the different flow passes in color.

in the surface layer of the simulations performed while the negative Φm values are due to the negative velocity gradients above $H/2$. Though not in perfect agreement with the law-of-the-wall, due to the limitations of the LES solver available in FLUENT, a clear logarithmic profile develops in the surface layer that will be used in the successor simulations including the actuator discs.

5-3 Discussion

A traditional problem, as recognized in LES of the ABL, is that the mean velocity profile differs from the log-law-of-the-wall in the surface layer (lowest 10% of the boundary layer height). Because of the computational costs involved it is too costly to resolve all the near wall turbulent structures, for high Reynolds number flows, therefore the need for a wall-model. As already observed in the work of *Mason* (1994)[70] the Smagorinsky-model coupled with a wall model is unable to capture the logarithmic velocity profile. The problem arises near the rough surface where the contribution of the SGS model dominates that of the resolved terms yielding **excessive gradients of the mean velocity near the wall**.

The cause of the discrepancy was identified and analysed in the work of Porté-Agel and Mason [73, 70] and was mainly attributed to the very dissipative nature of the Smagorinsky model in the near-surface region. The total turbulence kinetic energy is therefore damped to levels that are not large enough to reduce the mean shear in the region. As a result many of the LES simulations using the Smagorinsky model to capture the ABL profile show excessive gradients of the mean velocity near the wall. An improvement in the near wall region has been reported after the introduction of a backscatter model (the transfer of energy from unresolved to resolved scales)[66, 74]. Unfortunately a backscatter modification is not available in FLUENT.

Numerical simulations of a wind turbine array

In the present chapter numerical simulations of wind turbines placed in the atmospheric boundary layer (ABL) are presented. The simulations are performed within the LES framework available in the computational fluid dynamics solver FLUENT. The velocity profiles generated in the *precursor simulation* (section 5-2) are used as inflow conditions for all wind turbine simulations. The mean flow conditions at hub height are characterized by a free-stream velocity of $U_{hub,\infty}=6\text{m/s}$ and $TI_{hub,\infty}=12\%$. The wind turbines are modelled using the actuator disc concept, with both axial and tangential inductions, allowing for accurate predictions of the wind turbine wakes at a feasible computational cost. The turbine specifications and operational characteristics of the reference turbine are based on Vestas V80 2.0 [75]. Large eddy simulations are performed for different wind-turbine arrangements and turbine loading factors. The results are used to quantify the vertical transport of momentum and kinetic energy across the boundary layer.

6-1 Numerical approach

The computational domain is identical in size for both the vertical (y) and spanwise (z) directions (height $Ly = 800\text{m}$ and width $Lz = 800\text{m}$) as the one used to generate the wind profiles in the precursor simulation. The length of the domain is adjusted to facilitate two different turbine spacing distances and ranges from $Lx=2000\text{-}2240\text{m}$. The diameter of the wind turbines relative to the domain width is $D = 0.1Lz = 80\text{m}$ and are placed at a height of $y = 0.1Lz = 80\text{m}$ above the bottom boundary surface. The spatial discretization of the domain, with the actuator discs, uses the same grid size of 8m in all directions. Full resolution of the boundary layer is beyond the scope of the present project, therefore no additional refinement is applied in the vicinity of the rotors, since only the far wake characteristics are of interest.

When using the actuator disc to represent a turbine, the axial induction factor, a , provides an input to describe the turbine operation. The induction factor is related to the power and thrust coefficient of a turbine (refer to equations 3-9 and 3-8). The maximum power and thrust coefficients are achieved at the Betz limit for turbine efficiency for an induction factor $a=1/3$, see figure 6-1. Operating turbines, though, at the Betz limit may not yield the maximum efficiency for the wind turbine array. Suboptimal performance of the front turbines can be realised for smaller thrust coefficients for the upwind turbines, allowing the downstream turbines to capture more power. Sub-optimal power extraction has already been treated in the literature in terms of coordinating wind turbine controllers to optimize wind farm performance [76, 77]. This mode of operation was developed to account for the aerodynamic coupling (wake interactions) between neighbouring turbines to maximize the power captured by a collection of wind turbines.

In the present study we treat the cases of both optimal and suboptimal wind turbine loading in terms of a qualitative comparison of the mean flow statistics affecting mixing the wake region. Though extracted power values for the discs are reported, we have no interest in optimizing the total extracted power extracted by the wind-turbine array. Mean kinetic energy flux and turbulence intensity profiles are plotted in downstream locations of the wake region to evaluate the efficiency of the mixing. Different wind turbine loading is expressed in terms of the modified thrust coefficient C'_T for optimal and sub-optimal axial inductions: $a=1/3$ for the Betz limit and $a=0.17$ for sub-optimal operation. Using the more familiar definition of the thrust coefficient, the two loading cases are characterized by $C_T=0.88$ and $C_T=0.56$ for all actuator discs, corresponding to a tip speed ratio of $\lambda=8$ and $\lambda=7$ respectively.

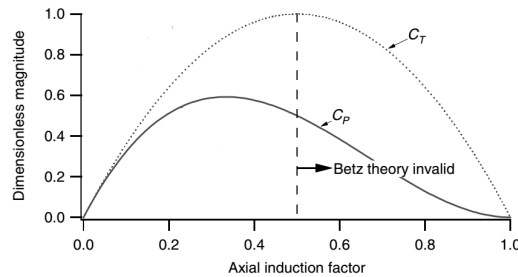


Figure 6-1: C_P vs C_T of an ideal turbine [10].

A summary of the realized simulations is presented in table 6-1. Case (a): two aligned actuator discs, with a spacing of ten rotor diameters, operating under suboptimal conditions. Case (b): Four aligned wind turbines are simulated with inter-turbine spacing of six rotor diameters, under sub-optimal operation. Additionally, in case (b) the effect of swirl (blade rotation) on the wake flow is modelled. For the first two test cases sub-optimal operation was realized for a thrust coefficient: $C_T=0.56$ which corresponds to an induction factor of $a \sim 0.17$. The wake flow characteristics, for the actuator disc model with swirl flow specification (ADM-R), under partial ($C_T=0.56$) and optimal ($C_T=0.88$) loading are presented in case (c). The effect of local grid refinement on array efficiency and power predictions is presented in Appendix B.

The inflow conditions for all four cases are identical using the generated profiles of $x/y/z$ velocities generated in the precursor simulation. The inflow profiles correspond to the 7th,

Table 6-1: Summary of cases and corresponding parameters for the numerical computations. The notation used for the actuator disc simulations without rotation, ADM-NR, and the simulations of the added swirl on the flow, ADM-R, is the one used in the work of Porté-Agel (2010) [15].

Case	WTD's	WTD Loading	WTD Spacing	Lx x Ly x Lz	Grid resolution
(a)	2 Discs (ADM-NR)	$C'_T=0.85$	10D	25D x 10D x 10D	D/10
(b)	4 Discs (ADM-NR/ADM-R)	$C'_T=0.85$	6D	28D x 10D x 10D	D/10
(c) [BASELINE]	4 Discs (ADM-R)	$C'_T=0.85$ & $C'_T=2$	6D	28D x 10D x 10D	D/10

8th, 9th, 10th, 11th, 12th flow pass as explained in section 5-2. A total of, 10500 velocity files, are used for four pass-through times amounting to a wind file of 18.3 minutes real time with an average velocity in the domain of $\bar{U}_\infty=8.5$ m/s. The flow statistics presented in the following sections have been averaged over the latter two flow passes while the flow pass through times are re-evaluated based on the velocity at hub height of the first turbine.

The Reynolds number $Re_D = \bar{U}_{hub,\infty} D / \nu$ for the simulations is calculated based on the mean free-stream velocity at hub height $\bar{U}_{hub,\infty}$. All cases are run with ambient turbulence $TI_{H,\infty}$ levels at hub height of 12%.

Table 6-2: Summary of the wind turbine and wind inflow characteristics used in the numerical computations.

D [m]	H_{hub} [m]	v [m^2/s]	$\bar{U}_{hub,\infty}$ [m/s]	Re_D	$TI_{hub,\infty}$
80	80	1.79E-05	6	2.9E+07	12%

A circular surface area corresponding to the V80 wind turbine diameter was sketched, in a 3D CAD Design Software, SOLIDWORKS, and was extruded in the streamwise direction. It was found that due to the large scale of the domain it was necessary to model at 1/10th scale of the actual dimensions. The model was later on scaled up in FLUENT Meshing Tool to the desired dimensions. The computational requirements associated with three-dimensional, unsteady LES can only be run, within realistic time-frames, in computer clusters with multiple nodes in parallel. The calculations for the present study are submitted to the Linux based HPC12 cluster located at the faculty of Aerospace Engineering in TU Delft. The mesh generation and simulation set-up was done locally on a personal computer and later on submitted to the cluster queuing system for execution. The computational time required to obtain the flow statistics for i.e. a sample 8x8x8 cell domain (D/10 spacing) was approximately 100 hours using the latest/fastest cores on HPC12 (type:h, 20 Intel(R) Xeon(R) CPU E5-2670v2 cores with 4GB of RAM/core).

6-1-1 Actuator Disc model in FLUENT

The CFD software FLUENT utilizes the "fan" boundary condition to simulate propeller induced flow. It is formulated as a discontinuous pressure jump across an infinitely thin surface and is specified as a function of the normal velocity at the disc. For the wind turbine simulations attention is needed so as to model the fan with the pressure drop downwind of the actuator discs. The reverse fan direction checkbox is used, if needed, for corrections. The pressure jump across the disc corresponds to the thrust of the rotor (eq. 6-4) and is calculated from

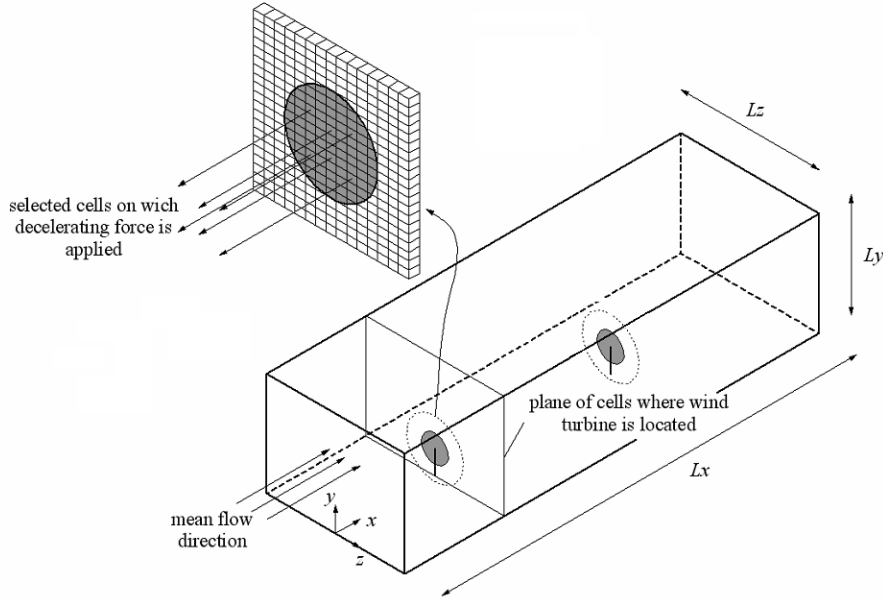


Figure 6-2: Schematic view of the computational domain and two actuator discs aligned in the streamwise direction [11].

the normal velocity averaged over the disk area. The model can either be used as a one-dimensional approximation of the thrust force or with an added tangential velocity component to account for the effects of blade rotation. The radial variation of the thrust force can be approximated in the fan model by applying different pressure jumps along the disc radii; not used in the present study. The effect of each wind turbine on the flow is expressed in terms of the thrust force:

$$T = -\frac{1}{2}\rho C'_T u_D^2 A \quad (6-1)$$

where: C'_T is the modified thrust coefficient corresponding to the reference velocity at the disc u_D rather than the one far upstream. In LES of wind turbine arrays, with significant wind turbine wake interactions, the upstream reference velocity (see eq. 3-8 for the classical definition) is not readily known. For our simulations, it is more natural to use the velocity at the rotor disc u_D . The classic actuator disc theory allows relating both velocities according to a the induction factor (eq. 3-7). We also define C'_T [19]:

$$C'_T = \frac{C_T}{(1-a)^2} \quad (6-2)$$

In the absence of friction C'_P equals C'_T and C_P is calculated based on eq. 6-3

$$C_P = (1-a)^3 C'_P \quad (6-3)$$

Assuming a surface area, A , of the actuator disc the thrust is calculated from the pressure difference before and after the disc as:

$$T = A(p^+ - p^-) \quad (6-4)$$

Based on eq. 6-1 that relates the modified thrust coefficient with thrust we get that the pressure difference at the disc relative to C_T' and upstream velocity is calculated as:

$$\Delta P = \frac{1}{2} C_T' \rho u_D^2 \quad (6-5)$$

The fan boundary condition, in FLUENT, is realised with a **pressure jump** and is assumed to be a polynomial function in the form:

$$\Delta P = \sum_{n=1}^N f_n u^{N-1} \quad 1 \leq N \leq 7 \quad (6-6)$$

where: ΔP is the pressure jump, f_n are the pressure jump coefficients and u is the velocity magnitude normal to the fan. Based on eq. 6-5 and 6-6 it is easily understood that a 2nd order polynomial ($N=3$) is required to simulate the pressure jump across the disc relative to the normal velocity.

The work-flow of estimating the pressure jump coefficient f_n used in FLUENT is by calculating C_T' (eq. 6-2) for the desired C_T values and in turn the pressure drop ΔP from eq. 6-5 for each one of the discs. It is easily understood that the pressure drop at the discs is proportional to the square of the velocity at the discs u_D , therefore $N=3$ is used when solving for f_n in eq. 6-6. For an induction factor $a=1/3$ that corresponds to the Betz limit for optimal energy extraction, the optimal thrust coefficient is $C_T=0.88$. The modified thrust coefficient is therefore calculated from eq. 6-2 and is equal to $C_T'=2$. The pressure jump coefficient is therefore calculated to be $f_n=-1.21$. (mean velocity at hub height $U_{hub}=6\text{m/s}$ & $\Delta P=43.6\text{Pa}$). The negative sign on the coefficient indicates the desired pressure drop in the stream-wise direction. For sub-optimal power production we assume $C_T=0.56$ which corresponds to an induction factor $a=0.17$ and a modified thrust coefficient $C_T'=0.85$. The pressure jump at the disc for an average hub height velocity of 6m/s is estimated to be $\Delta P=11\text{Pa}$ and the pressure jump coefficient: $f_n=-0.3$.

6-1-2 Wake rotation

For flows with significant three-dimensional effects the values of the tangential and radial velocities need to be introduced to generate swirl in the flow. To account for the **swirl flow** and simulate the effects of wake rotation in the flow downstream the discs, we use the tangential velocity component in the fan BC available in FLUENT. The radial induced velocity is typically small compared to the axial and tangential velocities and is therefore often neglected in calculations. The tangential velocity at each point in the radial direction is calculated as: $v_\theta = v_x \cos\theta + v_y \sin\theta$ where " v_x " is the instantaneous x-velocity, " v_y " is the instantaneous y-velocity and " θ " is the angular coordinate. The $\cos\theta$ and $\sin\theta$ functions are defined as: $\cos\theta = x/r = x/\sqrt{x^2 + y^2}$ and $\sin\theta = y/r = y/\sqrt{x^2 + y^2}$.

These velocities can be specified as polynomial functions in FLUENT of the radial distance from the fan centre. The radial velocity is specified as:

$$u_r = \sum_{n=-1}^N g_n r^n \quad -1 \leq N \leq 6 \quad (6-7)$$

The tangential velocity is specified as:

$$u_\theta = \sum_{n=-1}^N h_n r^n \quad -1 \leq N \leq 6 \quad (6-8)$$

where u_r and u_θ are the radial and tangential velocities, with polynomial coefficients g_n and h_n respectively and r the distance from the fan centre.

To calculate the coefficient h_n for the tangential velocity component, under partial ($C_T=0.56$) and optimal ($C_T=0.88$) loading of the discs, the following steps are followed. The axial induction factor, a is calculated from eq. 3-8 using the already determined thrust coefficient. For $C_T=0.56$ and $a=0.17$ the power coefficient is calculated to be $C_P=0.46$ from eq. 3-9. Since a depends only on the tip speed ratio, i.e. $a(\lambda)$, blade element momentum theory can be used to derive expressions for $C_P(\lambda)$ and $a(\lambda)$ in terms of the aerodynamic properties of the turbine blades. In our case, the $C_P(\lambda)$ curve for a 2MW wind turbine was obtained from the "Small wind turbines" book by David Wood [12] and is presented in figure 6-3. We can now determine from the plotted data on the graph the tip speed ratio for the desired power coefficient $C_P=0.46$, which was estimated to be $\lambda \sim 7$. From the definition of local tip speed ratio, see eq. 6-9, and a given wind speed at hub height, we can calculate the rotational speed of all blade elements in the spanwise direction.

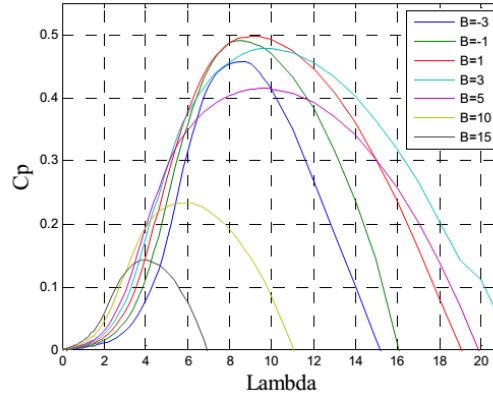


Figure 6-3: Power coefficient variation with tip speed ratio for an idealized 2MW turbine [12].

$$\lambda_r = \frac{\omega r}{U_{hub,\infty}} \quad (6-9)$$

where: ω is the angular velocity of each blade element and r is the distance from the rotor center. We can now calculate the angular induction factor a' for all blade sections (eq. 6-10) and finally the tangential velocity from eq. 6-11.

$$a' = \frac{a(1-a)}{\lambda_r^2} \quad (6-10)$$

$$a' = \frac{u_\theta}{2\omega r} \quad (6-11)$$

For $C_T=0.88$ and $a=1/3$ the power coefficient is calculated to be $C_P=0.59$ from eq.3-9. Once again based on the V-80 data from the C_P - λ plot and after adjusting the optimal power coefficient $C_P=0.59$ to the max power coefficient for the V-80 $C_P=0.5$ we obtain the optimum tip speed ratio $\lambda \sim 8$. For a free stream flow speed at hub height of $U_{hub,\infty} \sim 6\text{m/s}$ the tangential velocities for partial ($C_T=0.56$) and optimal ($C_T=0.88$) loading of the discs are presented in table 6-3.

Table 6-3: Tangential velocities for all blade elements. The results are plotted for partial ($C_T=0.56$) and optimal ($C_T=0.88$) loading of the discs.

r [m]	$C_T=0.56$			$C_T=0.88$		
	λ_r	a'	u_θ [m/s]	λ_r	a'	u_θ [m/s]
2	0.35	1.1518	4.84	0.40	1.3819	6.63
4	0.70	0.2880	2.42	0.80	0.3455	3.32
6	1.05	0.1280	1.61	1.20	0.1535	2.21
8	1.40	0.0720	1.21	1.60	0.0864	1.66
10	1.75	0.0461	0.97	2.00	0.0553	1.33
12	2.10	0.0320	0.81	2.40	0.0384	1.11
14	2.45	0.0235	0.69	2.80	0.0282	0.95
16	2.80	0.0180	0.60	3.20	0.0216	0.83
18	3.15	0.0142	0.54	3.60	0.0171	0.74
20	3.50	0.0115	0.48	4.00	0.0138	0.66
22	3.85	0.0095	0.44	4.40	0.0114	0.60
24	4.20	0.0080	0.40	4.80	0.0096	0.55
26	4.55	0.0068	0.37	5.20	0.0082	0.51
28	4.90	0.0059	0.35	5.60	0.0071	0.47
30	5.25	0.0051	0.32	6.00	0.0061	0.44
32	5.60	0.0045	0.30	6.40	0.0054	0.41
34	5.95	0.0040	0.28	6.80	0.0048	0.39
36	6.30	0.0036	0.27	7.20	0.0043	0.37
38	6.65	0.0032	0.25	7.60	0.0038	0.35
40	7.00	0.0029	0.24	8.00	0.0035	0.33

6-1-3 Wind turbine array efficiency

An estimation of the array efficiency can be made, based on the thrust values for the turbines obtained from the simulation results. Methodology: Two new surfaces, equal to the rotor area, are created right upstream and downstream the rotor area. The **Surface- > transform surface** module is used to create the surfaces based on the reference area of the ADs at $dx=+1/-1\text{m}$ relative to the location of the each one of the discs. The force on the flow, for each one of the new surfaces, is calculated with the **surface integral** calculator of mean static pressure available in the **Reports** tab for FLUENT 14.5 [78, 79]. The total force

on the flow is the algebraic sum of the two calculated forces on the flow. The mean extracted power for each one of the turbines is then calculated as $P_{disc} = T\bar{u}$ and the efficiency of the farm based on eq. 6-12. C'_T is calculated from the pressure difference: static pressure on the upstream and downstream surface in the vicinity of the discs from eq. 6-2 which is equal to C'_P ¹. C_P in turn is calculated from eq. 6-3. The methodology described above, to estimate the extracted power for each one of the discs, accounts for slight variations in the power coefficient of the turbines and will be used for all the upcoming test cases.

$$n_{wf} = \frac{P_1 + P_2 + \dots + P_N}{NP_1} \quad (6-12)$$

6-2 Wind Turbine array simulation results

In the present section the results for the wind turbine simulations, modelled as actuator discs, are presented. All presented simulation results are evaluated for the same computational time with identical inflow velocity profiles (generated in the ABL section) and cfd solver settings. A total of three flowthrough passes are simulated (statistics are gathered for the latter two) while the flowthrough time is calculated as: $t = x/\bar{u}_{hub,\infty} = 2240m/6ms^{-1} \sim 373s$. Three flow passes require 1120s or 11200 time-steps for a time-step size $\Delta t=0.1s$ and an average of 5 days of computational time/test case. The results for the four case studies summarized in table 6-1 are presented in the following sections.

(a) 2 wind turbines in a row

A two wind turbine array, with a spacing distance of ten rotor diameters (10D), placed in a 25D domain is simulated in the present section as seen in figure 6-4. The domain was extended at a distance of 5D upwind the first turbine to avoid any interaction of the inlet boundary surface with the first actuator disc. A large spacing distance of ten rotor diameters between the turbines to record the velocity deficit profiles far downstream the actuator discs. A downwind distance of 10D from the second turbine was used to avoid the interaction with the outlet BCs as well as minimize the effect of backflow on the simulation results. Backflow is often observed with outlet boundary conditions as the solver is constantly preserving the mass balance in the domain. The width and height of the domain were both set as 10D and the turbines were placed at the center of the computational domain at a height, $y=1D$. The computational domain and mesh details are summarized in Table 6-4.

The spatial distribution of two turbulence statistics is used to characterize the evolution of the wind-turbine wakes: the normalized streamwise velocity deficit, $\Delta\bar{u}/\bar{u}_{hub}$, and the total streamwise turbulence intensity, $TI_i = \frac{u_{i,RMS}}{U_\infty}$.

where: $u_{i,RMS}$ is equal to $\sqrt{u'u'}$ $\sqrt{v'v'}$ $\sqrt{w'w'}$ for $i=x,y,z$ respectively. The streamwise velocities downstream AD1 (figure 6-5 (left)) indicate a poor wake recovery at distances up to

¹Frictionless flow is assumed meaning that the assumption of $C'_T = C'_P$ is valid. In reality, the drag on the turbine blades plays an important role, which mainly affects the torque, such that C'_P is in practice significantly lower than C'_T . $C'_P = 0.985 \cdot C'_T$ accounts for the drag on the blades [19]

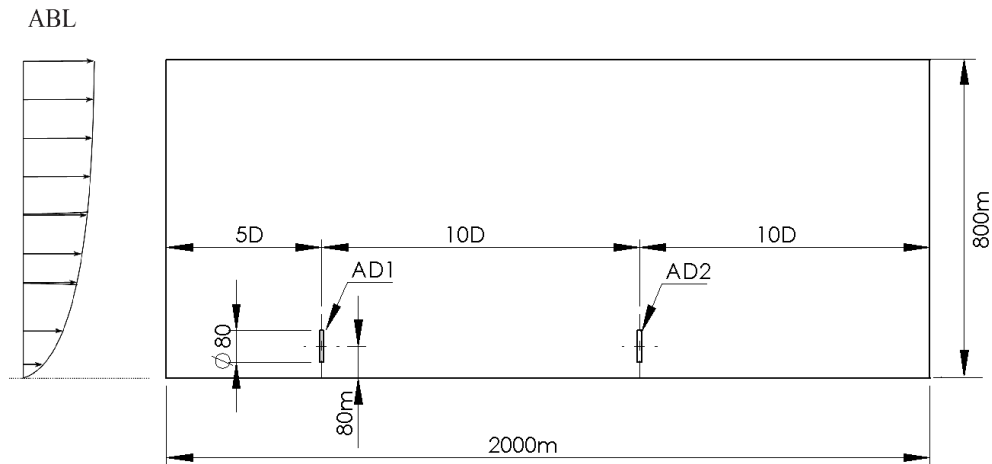


Figure 6-4: Side view of the computational domain with two wind turbines in a row.

Table 6-4: Mesh details of the computational domain for case (a)

Parameter	Value
Domain width: L_z	10D
Domain height: L_y	10D
Turbine spacing	10D
Domain length downstream AD2	10D
Domain length upstream AD1	5D
Cell spacing [m]	8 (D/10)
Aspect ratio (max)	6
Orthogonal quality (min)	0.3
Computational cost (s/time-step)	30
Total nodes count	2,558,441

7 rotor diameters. Additionally, TI levels drop by 10%, on average, 1D after the disc and gradually increase at the top-tip height, above the ambient turbulence levels, at a distance of 3 rotor diameters. TI values remain below the free stream levels, at the lower 3/4 of the wind turbine, for all downstream locations. At the downstream locations of 3D and 5D TI levels gradually increase at the top-tip height from 25% to 47%. 7D downwind AD1, turbulence levels stabilize to 25% above the free stream values. The turbulence levels in the wake remain almost constant ~ 0.14 up to the location of the second wind turbine.

It is observed that *suboptimal operation* of the turbines has a strong effect on the flow dynamics in the wake. By decreasing the thrust, generated by the turbine, less turbulence kinetic energy is generated directly behind the upstream turbine. This, in turn, leads to reduced mixing and poor wake recovery at downwind distances at least up to ten rotor diameters.

Numerical studies have shown that turbulence intensity levels in the incoming flow can have a strong effect on the spatial distribution of the mean velocity deficit. Higher turbulence intensity levels have been associated with faster wake recovery [31]. Field measurements

have also shown that the turbine generated turbulence can enhance the vertical mixing of momentum leading to faster recovery of the wake velocity [34]. Lower than ambient TI levels, predicted downstream AD1, is therefore an indication of poor kinetic energy transport in the wake region and can in turn explain the slow velocity recovery observed. Simulations [80, 33] and experimental studies [81, 82] have shown that stand-alone turbines recover faster in conditions of higher turbulence intensity levels in the incoming flow. The same effects have been observed in large wind farms, such as the Horns-Rev offshore wind farm, where the deficit of the downwind turbines decreases from 50% to 30% as the turbulence intensity in the incoming flow increases from 3% to 12% [83].

Downwind AD2 (figure 6-5 (right)) a much faster recovery of the streamwise velocity is observed. The TI levels in the wake of AD2 are much more pronounced relative to the ambient ones. The TI levels reach a maximum of ~ 0.2 at a distance of $5D$, an increase of 42% relative to the levels measured at $x/D=-1$ for AD2. The turbulence levels then start decreasing and stabilize to a value of ~ 0.16 at $7D$ and are preserved to a value of ~ 0.15 till the end of the computational domain.

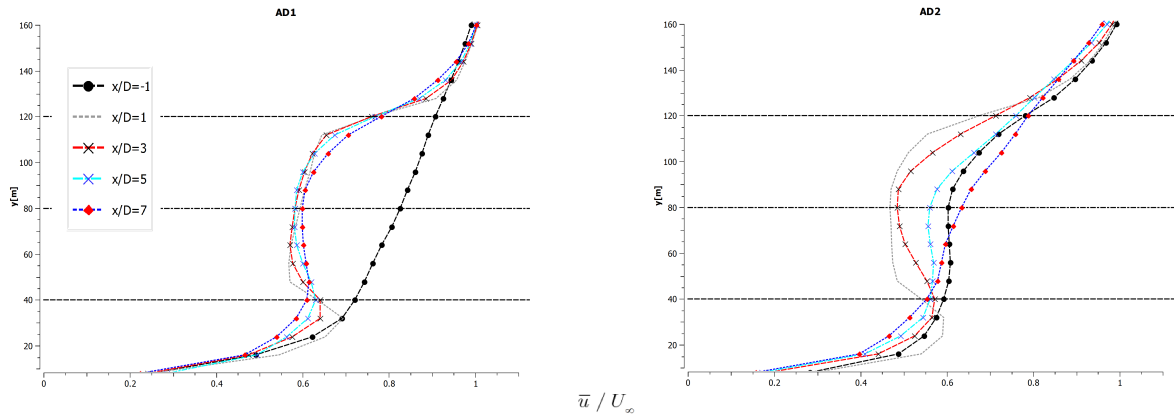


Figure 6-5: Normalized x-velocity, \bar{u}/U_{∞} , in the streamwise direction for AD1 and AD2.

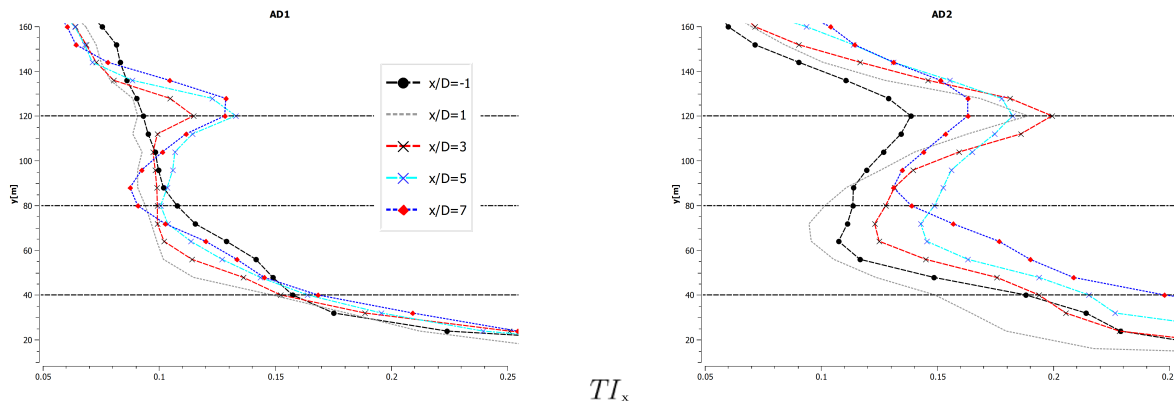


Figure 6-6: Turbulence Intensity, in the streamwise direction (x-direction), downstream AD1 and AD2.

Based on the estimated power extracted from the discs, the wind turbine array operates with an efficiency of 77%. The thrust force on the flow and the power extracted are presented in table 6-5. Minimal wake velocity recovery in all downstream locations along with the continuous increase in the turbulence levels in the domain are characteristics of an under-developed wake flow that cannot be used as reference for the simulations including the kite system. This is the reason why in all upcoming simulations the domain is extended to facilitate four actuator discs in a row with smaller spacing distance.

Table 6-5: Case (a) results: Thrust force and extracted power for two actuator discs, with 10D spacing, aligned in the streamwise direction.

ADM-NR	AD1	AD2	efficiency [%]	
\bar{u} [m/s]	5.958	4.895		
C'_T	0.835	0.813		
Thrust [N]	-90,928	-59,864		
Protor [W]	540,705	292,766	833,471	77

(b) 4 wind turbines in a row - ADM-NR/ADM-R

In the present case study the number of wind turbines simulated as actuator discs is increased to four and at the same time the spacing distance is decreased to six rotor diameters. The spacing distance of 6D is equal to the one used in the numerical simulations of Jha et al. [1] where turbulence transport in aligned and staggered wind turbine arrays was evaluated. The computational domain is extended in the streamwise direction by three rotor diameters in to facilitate the larger wind turbine array. The new wind turbine configuration is presented in figure 6-7. The wind turbine diameter, hub height and thrust coefficient remain unchanged.

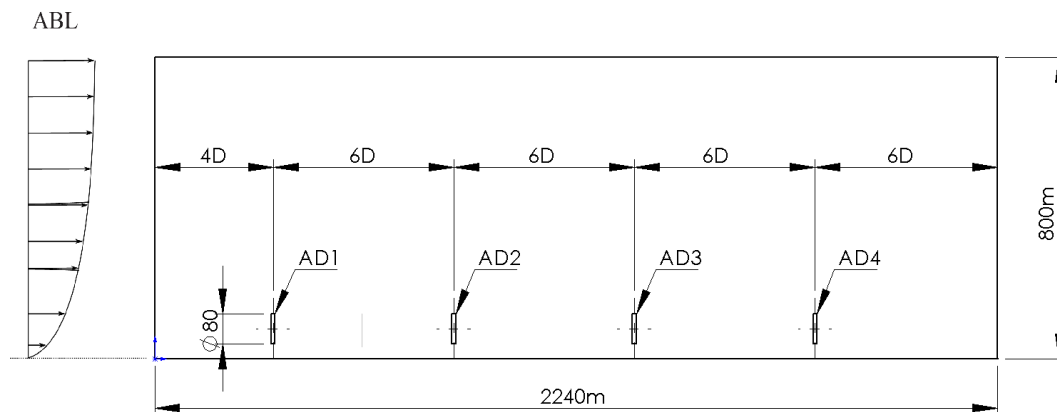


Figure 6-7: Visualization of the computational domain including 4ADs

The grid cell size and meshing method also remain unchanged. The 1st wind turbine is placed at 4D from the domain inlet and the 4th turbine at 6D from the domain outlet. The added domain length accounts for an extra 400 thousand cells (2.5m-> 2.9m ~ 13% increase in the grid size relative to the initial domain) that translates into a 2s increase in simulation time

using the same type of computational resources. For 32s/time-step and 10500 time-steps the total simulated time is ~ 94 hours. The extra 2s of computational cost/time-step for the new domain amounts to a total of ~ 6 hours per simulation which is not considered substantial. The details of the new computational domain are presented in table 7-3.

Table 6-6: Mesh details of the computational domain

Parameter	Value
Domain width: L_z	10D
Domain height: L_y	10D
Domain length	28D
Turbine spacing	6D
Domain length upstream AD1	4D
Cell spacing [m]	8 (D/10)
Aspect ratio (max)	12.8
Orthogonal quality (min)	0.15
Computational load (s/time-step)	32
Total nodes count	2,894,441

The characteristics of the wake flow for the new spacing distance and the larger number of wind turbines are presented in the following sections. The effect of swirl in the flow is also evaluated in terms of power production and array efficiency.

Case (b1): LES/ADM-NR

The results for the wind farm simulations where the actuator discs are simulated as a pressure drop without swirl velocity specification (ADM-NR) are presented. The cut-plane, where the results are sampled, is located at the middle of the discs parallel to the streamwise flow. Four locations in the streamwise direction are plotted for each actuator disc to evaluate the development of the wake flow. The streamwise velocity plots normalized over the free stream velocity are presented in figure 6-8. Significant wake recovery is observed from the 2nd wind turbine onwards. The 3rd and 4th discs show a full recovery of the wake velocity at a 5D distance relative to their inflow conditions ($x/D=-1$). TI levels gradually increase downstream the first two turbines to an average of 66% above the ambient turbulence levels. The maximum TI levels are observed at a distance of 3D downstream AD3 just below the top-tip height to a value of ~ 0.23 (91% increase to the ambient TI). TI levels drop down to 0.18 at the disc area of AD3 for $x/D=5$. The presence of the 4th turbine does not account for any other increase in TI levels in the domain. The turbulence intensity levels subside to a value of 0.15 (25% higher than ambient) at $x/D=5$. From the second turbine onwards the wake velocity recovery remains on the same levels and is in accordance with the measurements presented by Hansen and Barthelmie [83] for the Horns Rev wind farm.

In figure 6-10 the out of plane velocity, w , normalized over the free stream velocity (\bar{w}/U_∞) is plotted. It is evident that the modelling of the actuator discs as a streamwise pressure jump does not introduce any tangential velocity component and therefore no rotation in the wake flow. The rotation of the wake, due to the rotation of the blades, is considered in the following section.

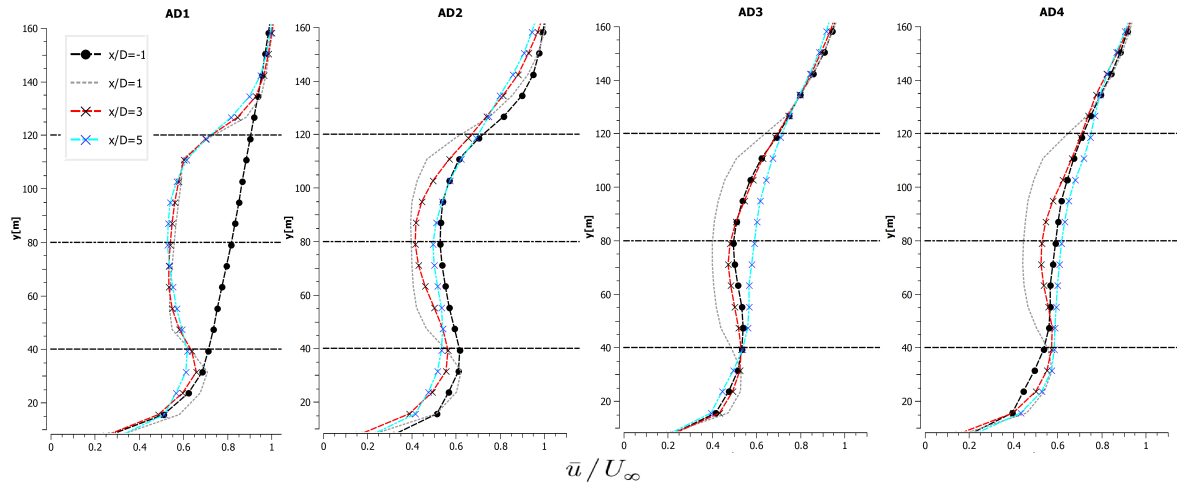


Figure 6-8: Normalized x-velocity, \bar{u}/U_∞ , plots in the wake of the discs (ADM-NR). The time-averaged velocities are gathered in locations: $x/D=-1/1/3/5$.

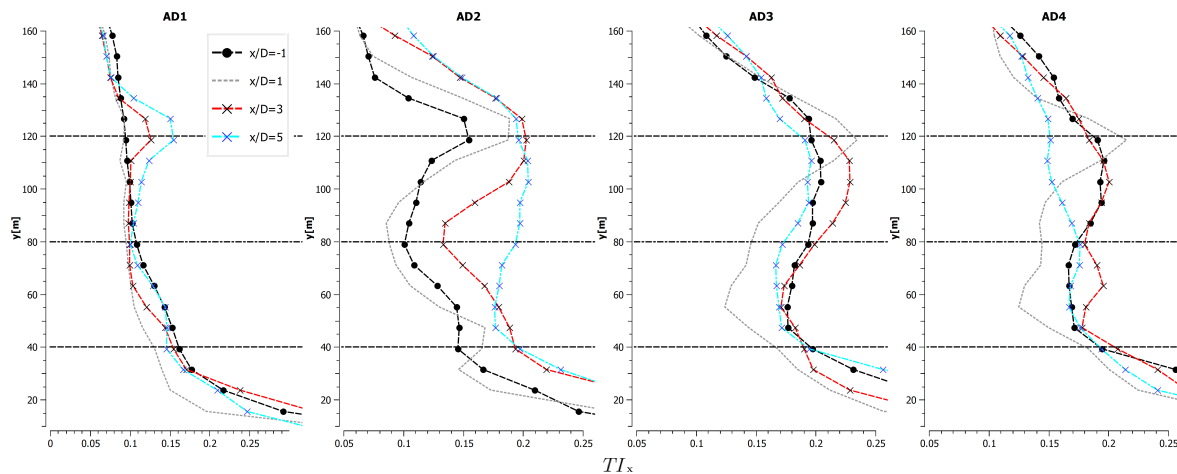


Figure 6-9: Turbulence intensity, in the streamwise direction (x-direction), at the discs (ADM-NR). The TI data are gathered in locations: $x/D=-1/1/3/5$.

The power extracted from the wind turbines is calculated in a similar fashion to the one presented in section 6-2. The thrust forces on two surfaces are obtained from the simulation results at a streamwise distance $dx=-1/+1$ meters relative to the location of the disc. The product of the algebraic sum of the forces and the averaged velocity at the disc yield the average power extracted from the flow. We can estimate the efficiency of the wind turbine array from eq. 6-12 to 58.2% and the total power extracted from the turbines to 645 kW, see table 6-7. In the latter two wind turbines significantly higher wake velocity recovery is predicted, relative to the first two, mainly due to enhanced turbulence levels in the domain which are shown to promote turbulent mixing.

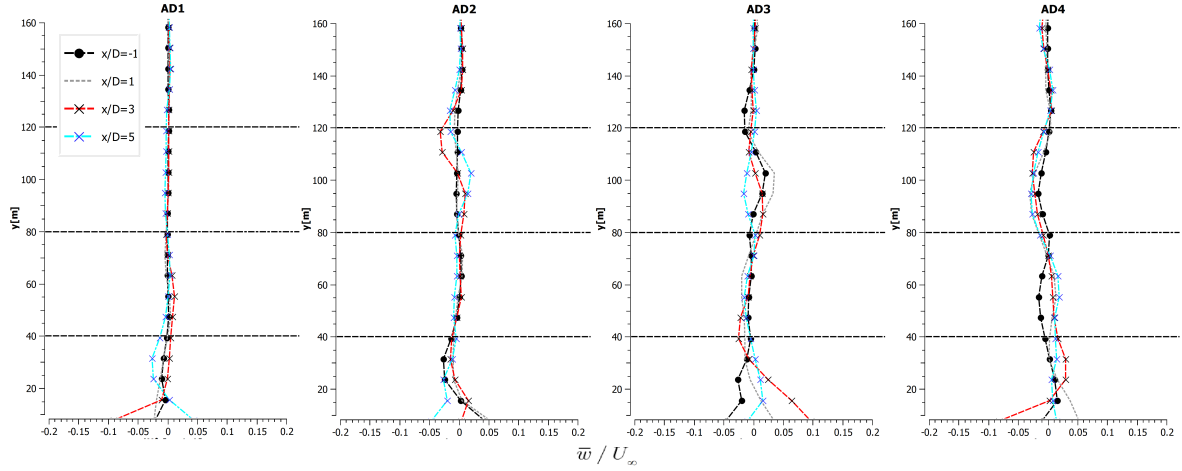


Figure 6-10: Out of plane velocity, \bar{w}/U_∞ , (z-direction) plots for the discs without specified tangential velocity (ADM-NR). The z-velocity data are gathered in locations: $x/D=-1/1/3/5$.

Table 6-7: Case (b1) results: Thrust force and power extracted for each one of the four actuator discs without swirl velocity specification (ADM-NR).

ADM-NR	AD1	AD2	AD3	AD4	efficiency [%]
\bar{u} [m/s]	5.768	4.307	4.301	4.566	
C'_T	0.839	0.819	0.777	0.748	
Thrust [N]	-86,456	-47,215	-44,170	-48,294	
Power [W]	500,320	204,346	189,843	221,090	1,115,599
					55.7

Case (b2): LES/ADM-R

The actuator disc model with axial and tangential inductions (ADM-R) is used, in the present section, to simulate the effects of blade rotation on the wake flow. Downstream the turbines the wake rotates with an angular velocity in the opposite direction to that of the rotor, to satisfy the conservation of angular momentum. The rotational kinetic energy represents a loss as it cannot be harnessed for energy conversion while at the same time the flow is accelerated radially due to centrifugal forces generated by the rotating plane. This results in out of plane velocity components in the y and z directions. The radial component (y-direction) is ignored in the present simulations as it generally accounts for less than 5% of the free stream flow [81].

The coefficient h_n , defined in eq. 6-8 for $N=-1$, is the input parameter for FLUENT to calculate the tangential velocity at the discs. For any blade element at location r , h_n is calculated using the methodology described in section 6-1-2. For the same thrust coefficient $C_T=0.56$, the tip speed ratio remains constant and equal to $\lambda=7$. At this point the time averaged disc velocities predicted for the ADM-R case will be used to estimate the tangential velocity for each one of the actuator discs instead of the average free-stream velocity at hub height. The tangential coefficient is at this point specified individually for each one of the discs. The results are presented in table 6-8 for $r=R$ (the coefficient remains constant in the radial direction).

Table 6-8: Parameters used to estimate the tangential velocity coefficient h_n at $r=R$ for $C_T=0.56$ & $\lambda=7$

	AD1	AD2	AD3	AD4
\bar{u} [m/s]	5.768	4.307	4.301	4.566
Ω [rad/s]	0.83	0.62	0.62	0.66
u_θ [m/s]	0.439	0.329	0.328	0.348
h_n	17.56	13.14	13.11	13.93

The normalized velocity profiles plotted in figure 6-11 present the same velocity recovery trend as the one presented in case (b1) (figure 6-8). Full recovery of the velocity profiles, is observed in both cases (ADM-NR/ADM-R), five rotor diameters downstream the latter two actuator discs, relative to their velocity profiles at $x/D=-1$. Slower velocity recovery can only be spotted 5D downstream AD2, relative to case (b1), that is also translated in smaller inlet velocities for AD3 and AD4. The TI profiles, before and after the introduction of swirl, follow similar trends characterized by an increase in the ambient TI levels from 0.1 to 0.2 as the flow develops in the array.

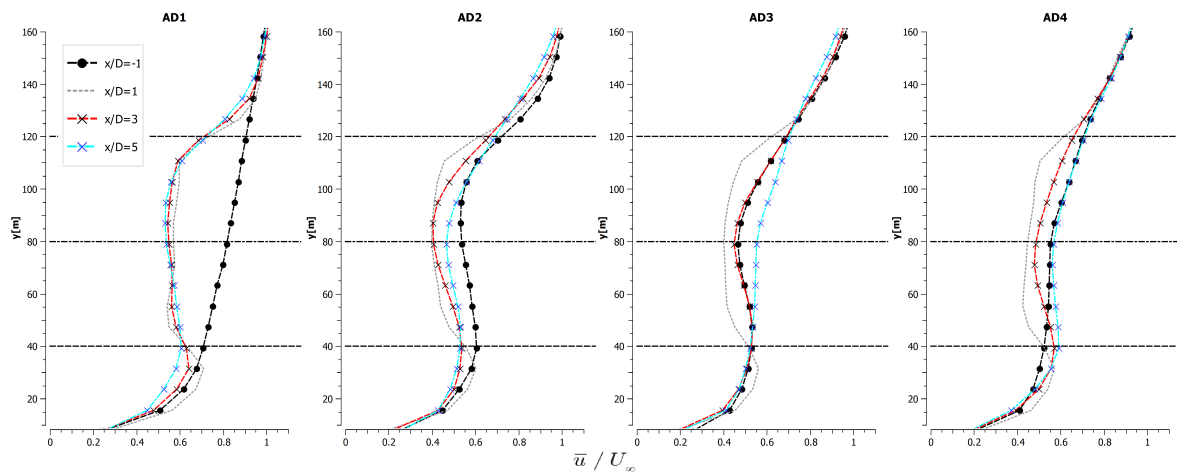


Figure 6-11: Normalized x -velocity \bar{u}/U_∞ plots in the wake of the discs (ADM-R). The time-averaged velocities are gathered in locations: $x/D=-1/1/3/5$.

The effect of the swirl on the flow is plotted in figure 6-13 in terms of the out-of-plane normalized velocity component at downstream locations. The magnitude of \bar{w}/U_∞ is much more pronounced downstream the first and second turbine and becomes less significant as we move towards AD3 and AD4. Higher TI levels, as we move further downstream, increase the mixing and minimize the effect of the out-of-plane velocity component.

The analysis of the turbulence intensity statistics provide inconclusive information relative to the mixing in the developing shear layer. In the work of Cal et al. (2010) [17] it is demonstrated that the Reynolds stresses² are responsible for the flow kinetic energy transport

²Reynolds stresses: $\langle u'^2 \rangle$, $\langle u'v' \rangle$ and $\langle v'^2 \rangle$ are present in turbulent flows. These terms cause diffusion of momentum normal to the flow direction and enhance the viscous effects in the flow. This mixing causes the

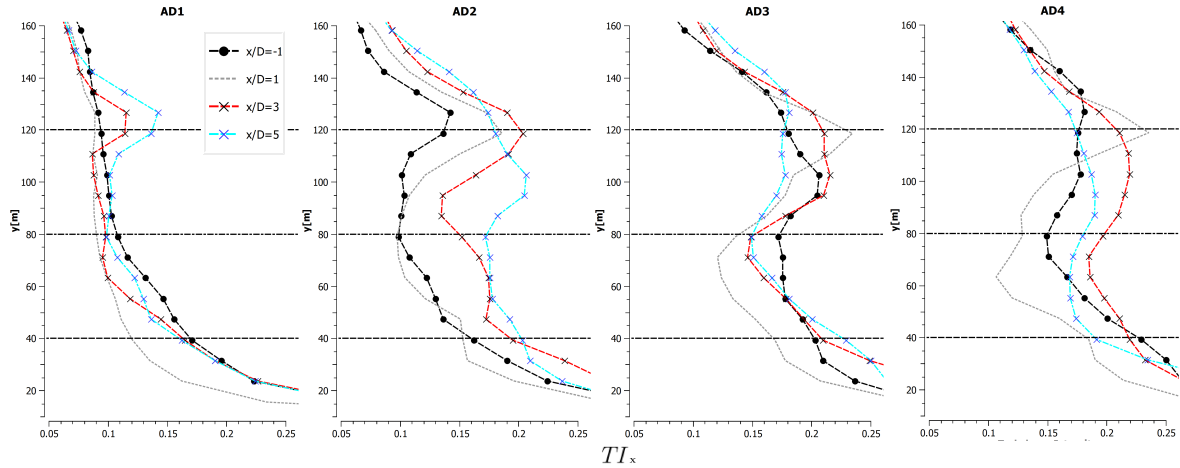


Figure 6-12: Turbulence intensity, in the streamwise direction (x-direction), in the wake of the discs (ADM-R). The TI data are plotted in: $x/D=-1/1/3/5$.

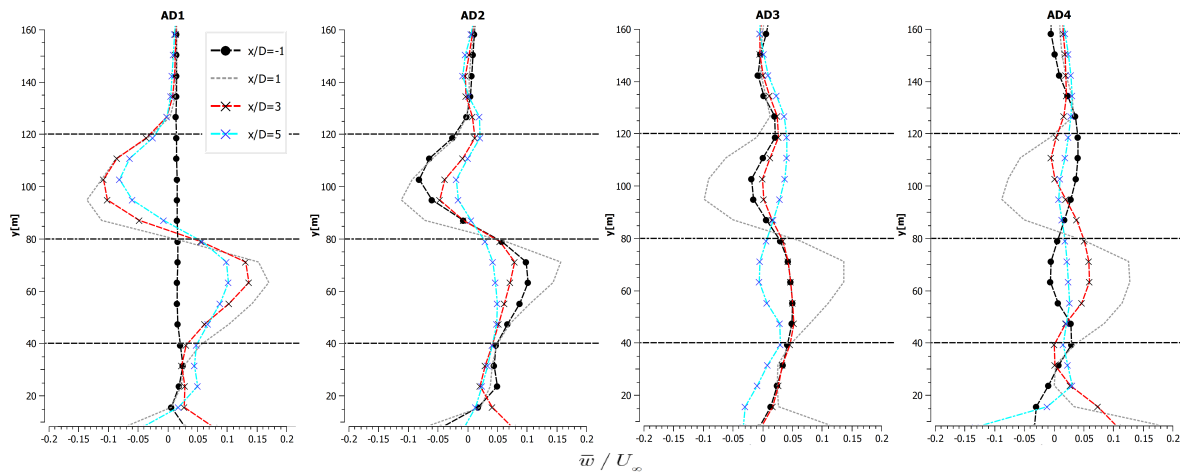


Figure 6-13: Out of plane normalized velocity, \bar{w}/U_∞ , (z-direction) plots for the discs (ADM-R) with specified tangential velocity. The z-velocity data are gathered in locations: $x/D=-1/1/3/5$.

and must therefore be considered when evaluating turbulent mixing. A comparison of the spatial gradient of the mean flow kinetic energy flux $\bar{\Phi} = -\bar{u}(u'v')$ is therefore evaluated in the x-y plane. The normalized mean flow kinetic energy transport: $\bar{\Phi}/U_\infty^3$ for the ADM-R and ADM-NR cases is presented in figure 6-14. It can be easily observed, from the contour plot, that the magnitude of the mean kinetic energy flux for the ADM-R case is \sim twofold the one predicted for the ADM-NR case. The effect of the added swirl, mainly downstream AD2, drastically enhances the transport of kinetic energy from the free-stream flow into the wind turbine wake.

wake to recover more quickly downstream the turbine.

${}^3\langle\Phi\rangle$ represents the fluxes in the x-y plane of the mean-flow kinetic energy flux. Positive values mean downward fluxes of kinetic energy, therefore energy entrained in the wind turbine wake.

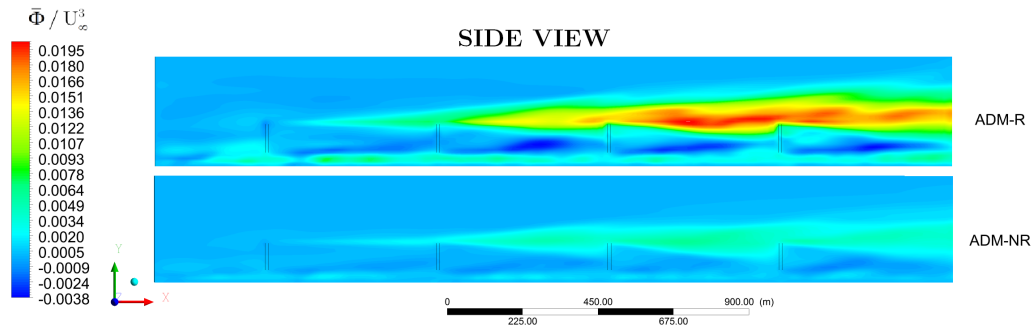


Figure 6-14: Side view of the normalized mean kinetic energy transport $\bar{\Phi}/U_\infty^3$ for the ADM and ADM-NR cases.

The mean static pressure integral calculator, over one upstream and one downstream surface area, is once again used to calculate the total thrust force on the flow. The time-averaged velocities at the discs, are then used to estimate the power extracted and determine the efficiency of the array. The results for case (b2) are presented in table 6-9. The added swirl velocity is generally considered as a loss of energy in the domain that cannot be harnessed by the turbines also reflected in the results obtained from the simulations. 1% loss in efficiency and 1.4% less extracted power from the domain, relative to the ADM-NR case, is predicted. As discussed in the work of Porté-Agel et al. (2010) [15] ADM-R yields mean velocity profiles that are in good agreement with the measurements in the wake.

The ADM-NR is able to capture the velocity distribution in the far-wake region ($x/D > 5$) but over-predicts the velocity in the center of the wake in the near-wake region ($x/D < 5$). A direct comparison of the velocity deficit for the actuator discs with and without tangential velocity specification is presented in figure 6-15. The loss in available kinetic energy is more pronounced close to the hub height of the discs ($y/D = 1$), as expected, and is visible for downwind distances up to five rotor diameters. In our case no experimental results are available to validate the simulation results therefore we will adopt a similar approach in the interpretation of the results.

Table 6-9: Case (b2) results: Average velocity at the discs, thrust force and power extracted for the four wind turbine case with added swirl.

ADM-R		AD1	AD2	AD3	AD4		efficiency [%]
	\bar{u} [m/s]	5.799	4.317	4.129	4.419		
	C_T'	0.838	0.817	0.813	0.823		
	Thrust [N]	-86,717	-46,849	-42,692	-49,466		
	Power [W]	502,872	202,249	176,275	218,591	1,099,987	54.7
ADM-NR	Power [W]	500,320	204,346	189,843	221,090	1,115,599	55.7

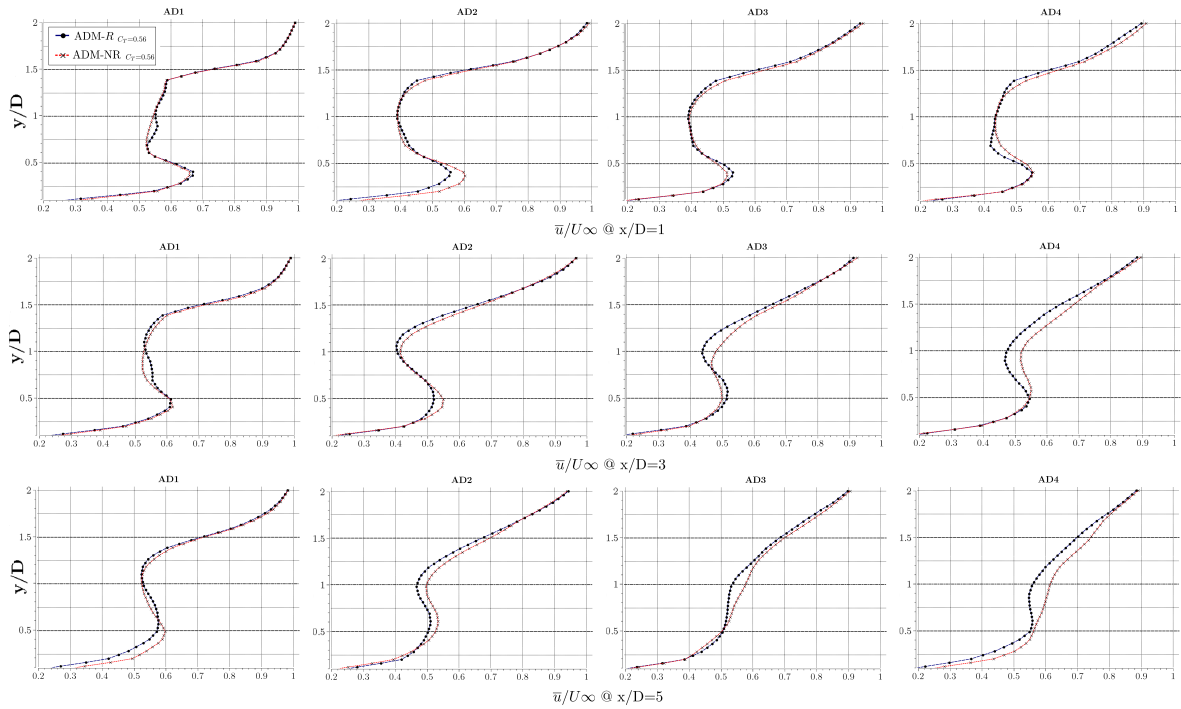


Figure 6-15: Normalized velocity deficit for ADM-R and ADM-NR plotted for three downwind distances $x/D=1/3/5$.

Wake expansion

The interaction of the ABL flow and a wind turbine induces the formation of a shear layer that starts at the edge of the rotor and expands along the domain fetch. Due to the non-uniformity of the velocity profile (wind shear), a non-axisymmetric shear layer, which is stronger at the upper edge of the rotor, is formed. The higher level of turbulence kinetic energy production is the main reason why enhanced turbulence levels are predicted in the upper half of the wake. The aforementioned effects have been reported in wind-tunnel [84, 85] and numerical simulation studies [86]. The outer part of the shear layer grows with downwind distance and contributed to the expansion of the wind farm wake [32].

The wake width is a significant parameter since it is the region of reduced momentum and increased turbulence from which less power can be extracted. Quantifying the wake expansion for the simulated cases is of significant importance since it will help identify the flying height of the kites. The wake expands with downstream distance since the streamlines that are diverged due to the presence of the rotor help expand the mixing area of the free-stream and the wake. According to Barthelmie et al. (2009) [2] the width of a single turbine's wake can be identified as the position where the normalized streamwise velocity (u/u_{ref}) is between 0.95 and 0.99. A side and top view of the wake width for the ADM-NR/ADM-R simulations are presented in figures 6-16 and 6-17 respectively.

No significant differences are noted in the expansion of the wake between the ADM-NR and ADM-R cases (figure 6-16). The wake expands from $D/4$ above the top-tip height of the first

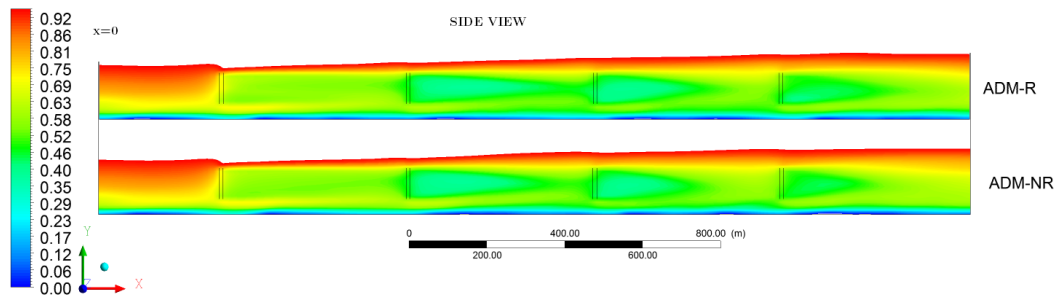


Figure 6-16: Side view of the wake expansion for the ADM and ADM-NR cases. The contour represents the normalized streamwise velocity \bar{u}/U_∞ .

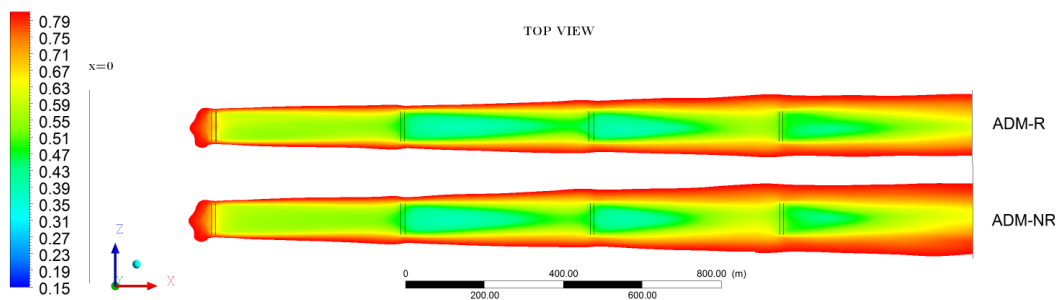


Figure 6-17: Top view of the wake expansion for the ADM and ADM-NR cases. The contour represents the normalized streamwise velocity \bar{u}/U_∞ .

disc to reach a maximum of $D/2$ above the top tip height of the fourth disc. More pronounced are the differences plotted in the x - z plane (figure 6-17) since there is a substantial increase in the wake area predicted for the ADM-NR case relative to the case with the added swirl. Enhanced kinetic energy transport in the wake due to the out-of-plane velocity component, for the ADM-R case, as well as the increased turbulence levels downwind AD3 and AD4 account for increased turbulent mixing in the wake region.

(c) 4 wind turbines (ADM-R) - partial vs optimal load

The effect of wind turbine loading, on wake evolution, is studied in terms of different tip-speed ratios that correspond to sub-optimal and optimal loading conditions. In the previous sections we already presented the results for sub-optimal operation ($C_T=0.56$, $a=0.17$ & $\lambda=7$) using the ADM-R model. A new simulation run using the actuator disc with axial and tangential inductions (ADM-R) operating under optimal conditions is presented here. Higher loading values were achieved in FLUENT by estimating beforehand the pressure coefficient of the polynomial function f_n presented in eq. 6-6. Based on the desired C_T values and expected mean velocities at the discs, $C_{T'}$ (eq. 6-2) and ΔP (eq. 6-5) were estimated for an induction factor $a=0.3$. For a mean velocity at hub height of $U_{hub,\infty} \sim 6\text{m/s}$ the pressure coefficient for FLUENT is estimated to be $f_n=-1.21$ (section 6-1-1). For $\lambda=8$ we calculate the coefficient h_n for the tangential velocity component, using section 6-1-2 as reference. For the downstream

turbines an ad hoc estimation of the disc averaged wind velocities is required to calculate the rotational speed and the tangential velocity component. Higher thrust means more energy extracted from the wind resulting in lower velocities at the discs. A rough approximation of 20% reduction in wind speed, relative to the values presented in table 6-9, is used to estimate the tangential velocity at the discs with higher loading. Such an approximation is not expected to compromise the accuracy of the results, since it is already shown that in highly turbulent flows the turbine-induced tangential velocity components are quickly dissipated in the near wake due to enhanced mixing. The ad hoc estimated values are presented in table 6-10.

Table 6-10: Parameters used to estimate the tangential velocity coefficient h_n at $r=R$ for $C_T=0.88$ & $\lambda=8$. The mean velocities at the discs are estimated to be 20% lower than the ones predicted in table 6-9.

	AD1	AD2	AD3	AD4
\bar{u} [m/s]	4.61	3.45	3.44	3.65
ω [rad/s]	0.92	0.69	0.68	0.73
u_θ [m/s]	0.255	0.19	0.19	0.202
h_n	10.18	7.62	7.60	8.07

Vertical profiles of the mean velocity, turbulence and kinetic energy flux are evaluated at a downstream distance of $x/D=5$ for each one of the actuator discs. Higher wind turbine loading is associated with higher thrust coefficient values, C_T for the discs and more energy extracted from the wind. This is translated into lower kinetic energy in the wake of the discs, predicted for the ADM-R $C_T=0.88$ case relative to the ADM-R $C_T=0.56$ case. The normalized mean x-velocity profiles, for the two loading cases examined, are plotted in figure 6-18. Wake velocity recovery downstream the rotor discs reveals the gradual development of the wake flow towards an equilibrium state as it develops inside the wind turbine array 6-18. As expected a more pronounced velocity deficit, for the higher loaded discs, is observed downstream AD1 as a result of the higher loading factor. From AD2 onwards, a much faster recovery of the wake velocity is observed relative to the relative inflow conditions ($x/D=-1$ /dotted lines) of the actuator discs. For AD3 & AD4 full wake velocity recovery is predicted at $x/D=5$. Interestingly, the velocity deficit for higher loaded discs recovers to the same levels in the domain as the ones predicted for discs in sub-optimal operation. Since the inflow conditions are identical for both loading cases, to account for the additional energy extracted from the domain, more efficient mixing with the undisturbed flow or enhanced flux of vertical momentum in the shear layer can be assumed. Turbulence intensity profiles and kinetic energy fluxes in the vertical direction plotted in figures 6-19 and 6-20 provide a good insight into the phenomena involved in the recovery of the wake.

Turbulence intensity profiles are plotted at $x/D=5$ for both loading cases in figure 6-19. TI profiles at $x/D=-1$ are also presented for reference to the ambient levels for each one of the discs. Streamwise turbulence intensity levels in the wake of the higher loaded turbines are much more pronounced relative to the partial loading case downstream AD1. The added turbulence due to higher loading of the discs is translated into TI levels twice the magnitude of the free-stream flow at the centre of the wake. Gradual development of the wake flow towards an equilibrium state is apparent since TI levels for AD3 and AD4, regardless of the loading factor, recover to the levels predicted at the inlet of the discs ($x/D=-1$) five rotor diameters

downstream. Higher added turbulence for the discs, under optimal load, are related to more efficient mixing and can explain the much faster recovery in the wake velocity downstream AD2, see figure 6-18.

The vertical transport of momentum from the free-stream flow in the turbine canopy is quantified in terms of the normalized flux of mean flow kinetic energy $\bar{\Phi}$ in the vertical direction [17]. The effect of higher wind turbine loading on the entrainment of kinetic energy in the wake is plotted in figure 6-20. Higher added turbulence levels predicted downstream AD1 are translated into higher values of vertical momentum flux resulting in a faster recovery of the wake velocity. Increased values of vertical momentum transport are only predicted downstream AD4 for the higher loaded discs.

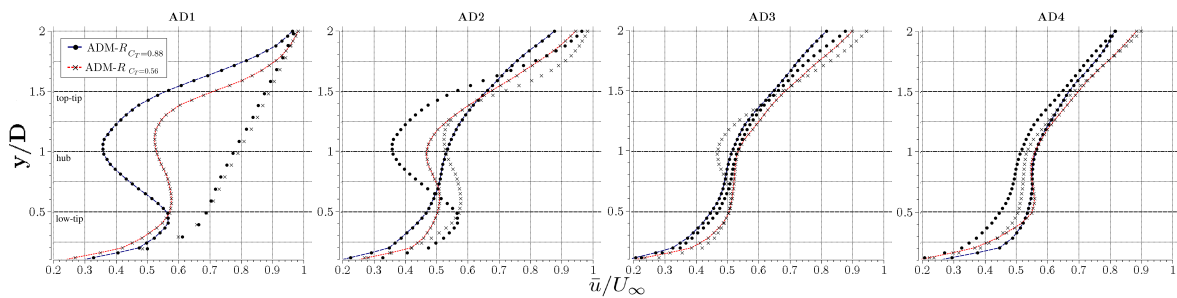


Figure 6-18: Normalized x-velocity profiles (continuous lines) at a downwind distance of 5 rotor diameters ($x/D=5$) for the actuator discs. The x-crosses represent the velocity profiles at $x/D=-1$ for $C_T=0.88$ & the dotted (no lines) for $C_T=0.56$.

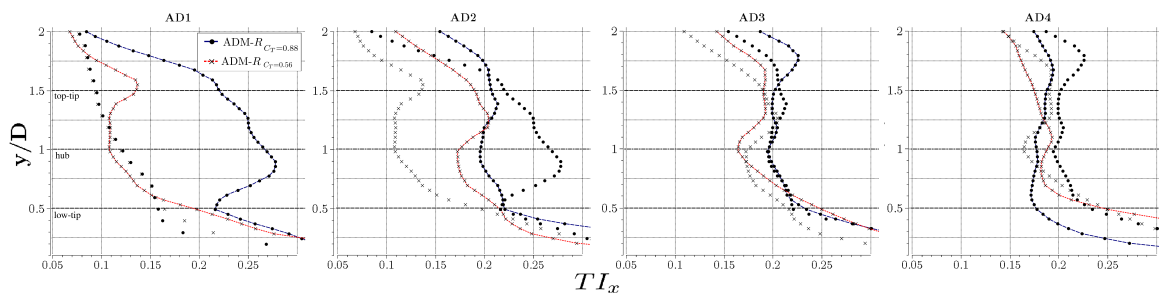


Figure 6-19: Turbulence intensity profiles at a downwind distance of 5 rotor diameters ($x/D=5$) for each one of the actuator discs under partial and optimal loading. The x-crosses represent the velocity profiles at $x/D=-1$ for $C_T=0.88$ & the dotted lines for $C_T=0.56$.

In table 6-11 the results from the simulation of the discs in optimal operation for the actuator discs are presented in terms of mean disc velocities, loading factor and extracted power and compared to the sub-optimal operation case. The power extracted by the wind turbines, calculated by the total thrust and the newly calculated average velocities, is estimated to be 18% higher for the turbines under optimal loading conditions compared to the partial loading case. Since the efficiency values largely depend on the power extracted from the first turbine, they can only be used for comparison between simulations when similar power values are obtained for AD1. The total extracted power from the domain will be the parameter to be used for comparison between simulations.

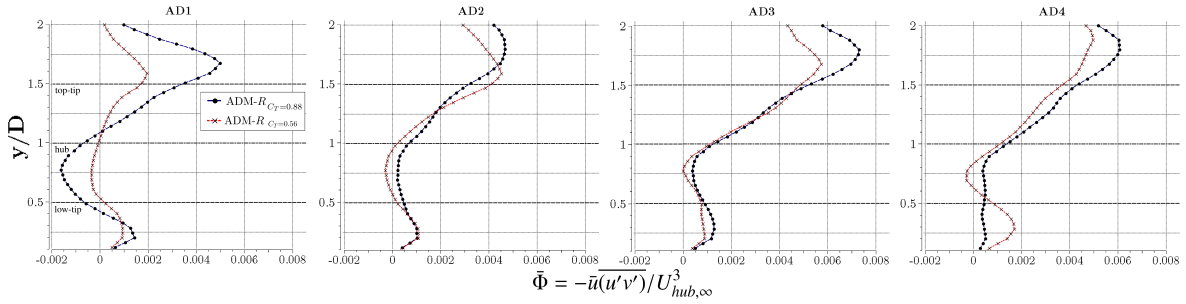


Figure 6-20: The radial profiles of the normalized mean flow-kinetic energy flux, $\bar{\Phi}$, are evaluated on the horizontal x-y plane. $\bar{\Phi}$ is plotted at $x/D=5$ downwind the actuator discs AD_i under partial and optimal load.

Table 6-11: Case (c) results: Average discs velocities, thrust and extracted power for the actuator disc model with rotation (ADM-R) operating under optimal load, $C_T=0.88$. The power extracted values of $C_T=0.56$ are also presented for comparison.

ADM-R		AD1	AD2	AD3	AD4	efficiency [%]
$C_T=0.88$	\bar{u} [m/s]	5.799	4.317	4.129	4.419	
	C_T'	1.947	1.876	1.922	1.916	
	Thrust [N]	-136,711	-56,010	-76,292	-72,361	
	Power [W]	652,947	174,404	273,924	253,414	1,354,690
$C_T=0.56$	Power [W]	502,872	202,249	176,275	218,591	1,099,987
						51.9
						54.7

The results presented in cases (b2) & (c) are the ones to more accurately approximate the characteristics of the wake, for the two turbine loading scenarios, and will therefore represent the base cases for comparison in chapter 7.

6-3 Discussion

The need to simulate a wind turbine array with more than two actuator discs was identified in the course of the simulations. Minimal wake velocity recovery in the two wind turbine array raised the issue of poorly developed wake flow that could not be considered for future comparison. The domain is therefore expanded to facilitate an array of four actuator discs, with smaller spacing distance ($6D$), aligned with the streamwise velocity component. Significant velocity recovery in the wake of the downstream turbines is predicted and the extracted power appears to reach an equilibrium after the second disc in the row; more pronounced in the optimal loading case. A fully developed state, with reference to the streamwise direction, can also be assumed for the turbulence in the domain since TI levels for the latter two wind turbines (AD3/AD4) fully recover, at a downwind distance of $5D$, to their inflow levels. Characteristics of fully developed flow are observed and can be considered eligible for the simulations including the kites in chapter 7.

Different specifications of the actuator disc model were also considered for the four wind turbine array. An actuator disc model only characterized by a streamwise pressure jump,

ADM-NR, and actuator discs with both axial and tangential inductions, ADM-R, were simulated. Consistent with the numerical results reported in the work of Porté-Agel (2010) [15] the velocity in the near wake (up to $5D$) is relatively over-estimated in the ADM-NR case. This explains the slightly faster recovery in the wake velocity deficit for ADM-NR (figure 6-15) compared to the ADM-R case. Slightly smaller wake expansion of the wake region (figure 6-17) for ADM-R is an indication of enhanced transport of vertical momentum and more efficient mixing. The ADM-R case also delivered 15% less power from the array compared to the ADM-NR case and an efficiency decrease of 4%. An anticipated result, in line with the results reported in the numerical work of Wu et al. [32] since blade rotation and the generation of swirl in the flow is a loss in mechanical energy that cannot be extracted by the wind turbines. A local refinement of the grid size, presented in Appendix B, cannot be treated with the level of certainty associated with global grid refinements therefore no strong conclusions can be drawn. The resolution of $D/10$, adopted in all upcoming sections of the report, strikes a good balance between the resolution of the relevant large eddies and the associated computational cost.

Numerical simulations of a wind turbine array with tethered kites

The objective for any kite application related to high altitude power generation is to generate the largest possible tug force, which is the pull force applied to the tether. Largest tug forces are directly related to the generated lift/drag ratio from the kite surface maximizing, in turn, the total forcing on the flow. The principles of maximizing the power output from a power generating kite system are therefore considered as guiding principles for the proposed design.

The kites are introduced in the computational domain as a discontinuous pressure jump over an infinitely thin surface specified as a function of the instantaneous inflow velocity. The "fan" boundary condition is used and the pressure jump coefficient in FLUENT is determined from tabulated pressure data of a 3D ballooned wing surface at a constant angle of attack of 10° . Since variations in the angle of attack in the spanwise direction complicate the pressure distribution at the wing surface, the kites are modelled as flat elliptical wings, with a constant angle of attack along the wing span. Based on the wing aerodynamics theory constant downwash velocity is associated with an elliptical wing surface generating an elliptic lift distribution [87].

A brief introduction of the simulated test cases of a four wind turbine array with suspended kites follows. The domain size, turbine number/spacing/actuator disc model (ADM-R) and kite height are kept constant for all evaluated cases. The effect of a series of design parameters on the wake flow is studied including: kite facing, kite size, actuator disc loading and kite power density is set up in a total of four case studies and presented in the following sections. In case (a) an elliptical kite surface of $105m^2$ is placed downwind each wind turbine at a height of 140m with two different facing configurations to evaluate the DSE [3] approach (ignored the drag component) vs the "correct" facing approach where both lift and drag forces contribute to the total body force on the flow. Case (b) deals with the effect of different kite surfaces on the development of the wake flow. Two elliptical kite surfaces are simulated: a small 8x16m kite with a projected surface of $105m^2$ and a large 16x32m kite with a projected surface of $470 m^2$. In case (c) the larger $470 m^2$ kite surface is employed to evaluate the effect of wind turbine loading after the introduction of a kite system. For all three aforementioned cases a

pressure jump of 39Pa (Appendix C table C-1) is used to simulate the forcing on the flow. Finally in case (d) three different power densities for the 470 m^2 kite surface, simulating higher apparent wind velocities (kite in motion) are evaluated. A summary of the realized simulations is presented in table 7-1.

Table 7-1: Summary of cases and corresponding parameters for the numerical computations of a wind turbines array with suspended kites.

Case	WTD's	WTD Loading	Kite size [m]	Kite area [m^2]	Kite power density [W/m^2]
(a1) "DSE"	4 Discs (ADM-R)	$C'_T=0.85$	8x16	$A_{kite,s}=A_{AD_i}/48=105$	307
(a2)	4 Discs (ADM-R)	$C'_T=0.85$	8x16	$A_{kite,s}=A_{AD_i}/48=105$	307
(b)	4 Discs (ADM-R)	$C'_T=0.85$	16x32	$A_{kite,l}=A_{AD_i}/12=470$	307
(c)	4 Discs (ADM-R)	$C'_T=0.85$ & $C'_T=2$	16x32	$A_{kite,l}=A_{AD_i}/12=470$	307
(d)	4 Discs (ADM-R)	$C'_T=2$	16x32	$A_{kite,l}=A_{AD_i}/12=470$	307/873/2456

7-1 Modelling the kite surface

The number of quantitative experiments on kites is limited and no wind tunnel measurements or in-flight data have been released, to our our knowledge, on pressure distribution. The pressure coefficient distribution of 3D flat plates that resemble the AR and Re of the chosen geometry for our kite system are used to simulate the aerodynamic performance of the kite system, explained in section 7-2.

The flow characteristics of a 3D ballooned wing section resembling a ram-air kite wing were measured in the experimental work of Aart de Wachter (2008) [13] for ASSET (Aerospace for Sustainable Engineering and Technology) at the Technical University of Delft. 3D measurements of the flying shape using photogrammetry and laser scanning and fluid analysis of the flow past the deformed shape using CFD were performed. The effect of ballooning of the wing on the flow and the resulting lift and drag relative to the NACA0012 profile was studied. An impression of a ballooned wing is presented in figure 7-1.

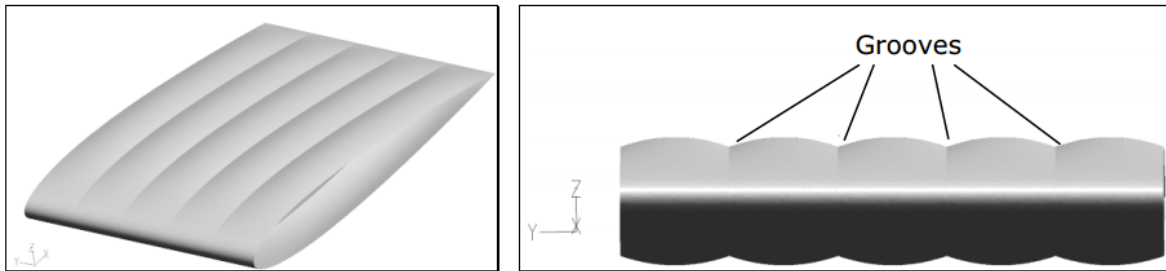


Figure 7-1: Grooves in the upper and lower surface due to ballooning of the wing [13].

The $k-\omega$ turbulence model was used to study the flow characteristics around a ballooned wing at an angle of attack of 10° . Figure 7-2 shows the pressure distribution for the ballooned wing and the reference NACA0012 airfoil. The curves are almost identical between the two wings while it is notable that there is hardly any pressure difference between the rib and the cell centre for the ballooned wing. The 3D effects of wind loading on the shape of the kite surface were identified after importing the captured geometry of the loaded kite (from

the wind tunnel) with photogrammetry into the CFD software. The dent identified in the pressure plots of figure 7-3 was caused by the suspension lines on the lower side of the ribs causing a deformation on the leading edge of the kite. The local pressure increase close to the leading edge of the kite, where it produces the maximum lift, lead to a reduction on lift of about 8%.

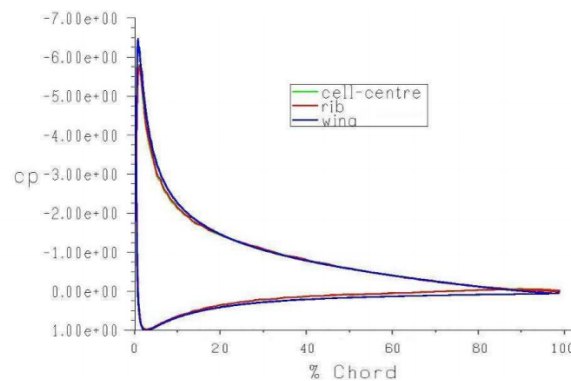


Figure 7-2: Pressure coefficients for ballooned wing (cell-centre/rib) and the NACA0012 profile (wing) simulations [13].

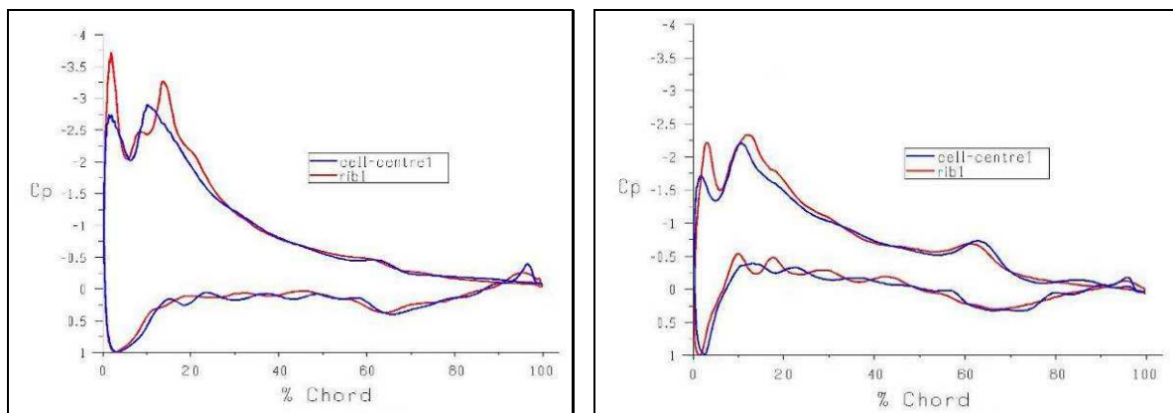


Figure 7-3: Left: Pressure distribution on the first rib and cell centre at high angle of attack. Right: Same distribution at low angle of attack [13].

The numerical data obtained from the work of Aart de Wachter are considered the basis for our simulations. The pressure distribution data of 3D ballooned wing surface obtained from both plots on figure 7-3 are captured, averaged and presented ($C_{p,l}$ & $C_{p,u}$) in Appendix-C. The captured pressure distribution is used to calculate the total force on the flow for each one of the simulated kites. Based on a free-stream velocity at kite flight height of $\bar{u}_w=7.8\text{m/s}$ an average pressure jump of 39Pa is estimated to model the suspended kites in the computational domain under steady flight.

7-2 Kite modelling conventions

The overall aerodynamic characteristics of a 3D kite wing, simulated as a curved rectangular wing and a flat rectangular non twisted plate with identical aspect ratio and Reynolds number, were compared in the work of Maneia (2013) [6]. It was reported that the curvature induces only a small deterioration of the aerodynamic properties, therefore the flat plate convention, to model the kite surface, is followed in the course of the present study.

The forces on the wing section can be determined via measurements of the pressure on the body's surface. The pressure differential between the upper and lower surface of the wing will cause a net force that is in turn analysed into lift and drag forces. The net aerodynamic force has the same magnitude but opposite sign with the force acting on the tether of a kite power system. The normal force is the difference of the pressure of the lower surface and the pressure over the upper surface of the wing section. The aerodynamic force relative to the free stream velocity V_∞ and normal force coefficient C_{F_a} (*Notation adopted from the Airborne wind energy book [88]*)

$$F_t = -F_a = -\frac{1}{2}\rho C_{F_a} A_w U_\infty^2 \quad (7-1)$$

To determine the pressure distribution along a wing section, a coefficient of pressure, C_p , is defined in eq. 7-2 where p is the local pressure, p_∞ is the free stream static pressure and $q_\infty = \frac{1}{2}\rho U_\infty^2$ is the free stream dynamic pressure.

$$C_p = \frac{p - p_\infty}{q_\infty} = \frac{p - p_\infty}{\frac{1}{2}\rho U_\infty^2} \quad (7-2)$$

Using Bernoulli's equation the pressure coefficient can be further simplified for incompressible, lossless, and steady flow [89]:

$$C_p = 1 - \left(\frac{V}{V_\infty}\right)^2 \quad (7-3)$$

Effectively the pressure coefficient can be used to measure the air speed over the surface of the airfoil. More negative C_p is related to higher local velocities relative to the free stream. The maximum C_p will occur at the leading edge stagnation point (zero velocity). It is expected that the minimum pressure coefficients will become more negative as the angle of attack increases up until the flow starts separating from the wing surface. The normal force coefficient in eq. 7-1 is computed by integrating the pressure coefficient, for the upper and lower wing surface, over the chord based on the trapezoidal rule as given by equation 7-4.

$$C_{F_a} = \int_0^1 (C_{p,l} - C_{p,u}) d\frac{x}{c} \quad (7-4)$$

7-3 Numerical setup

The basic principle of kite force generation and its ability to generate pulling forces lies in the manoeuvrability of the surface (figure 7-4). The generated tether force F_t is the vector sum of the airfoil's lift force F_L and drag force F_D .

$$F_t = \frac{1}{2} \rho u_a^2 A C_R \quad (7-5)$$

where: C_R is the resultant aerodynamic force coefficient expressed in terms of the local lift and drag coefficients: $C_R = \sqrt{C_l^2 + C_d^2}$. For the steady flight simulations a glide angle $\epsilon=10^\circ$ and an elevation angle $\beta=80^\circ$ are assumed in cases (a) (b) & (c). The aforementioned assumption yields an apparent wind speed u_a equal to the given wind speed of 7.8 m/s at a flight height of 140 meters. In case (d) the assumption of a kite in flight is used to evaluate the effect of higher power densities (result of higher apparent wind velocity) on the wake flow. For a dynamically flown kite, the airspeed u_a (eq. 7-6) is determined by the wind speed u_w at kite flight altitude, the kites glide angle ϵ and its position on the wind window, represented by its elevation angle β .

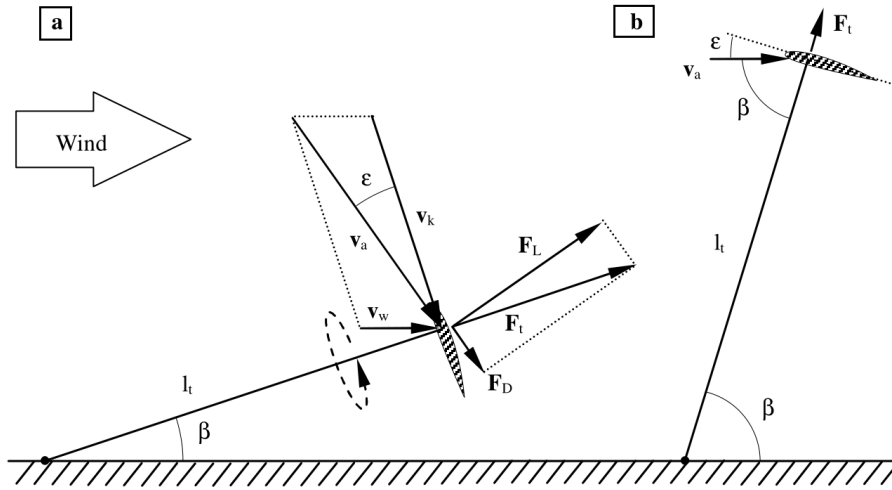


Figure 7-4: Left: (a) Force and velocity vectors at a kite in a continuous loop. Right: (b) kite in a static position [14].

$$u_a = u_w \frac{\cos \beta}{\sin \epsilon} \quad (7-6)$$

The resultant force/unit area exerted on the flow, due to the lift and drag forces acting on the kite, is introduced as a Gaussian shaped pressure jump in the computational domain. The body force in the flow due to the presence of the kite surface is realized, in the numerical simulations, with the fan boundary condition available in **FLUENT**. The aforementioned assumption is considered the only realizable option, regarding the computational cost, since

local refinement of the grid to match the y^+ requirements of LES for high Reynolds number flow is unrealistic.

The normal force coefficient and normal force per unit length are calculated from the pressure coefficient data in Appendix-C (table C-2) from equations 7-1 and 7-4 respectively. The sum of the normal-forces/unit-meter, presented in table C-1 over the chord of the kite, yield a pressure jump of 39Pa for a wind velocity of 7.8m/s. The total force on the flow is calculated as the product of the pressure jump, calculated earlier, and the projected surface area of the kite.

The Reynolds number is calculated using the kite's chord as reference length and the mean streamwise velocity at kite flight height (table 7-2). The side view (top left, figure 7-5) of the meshed computational domain helps visualize the successive grid refinements as we approach the locations of the kites. The grid refinement box is identified in the isometric and top-views of the domain (top right & bottom, figure 7-5) while centred in the refined area the kites, modelled as elliptical surfaces, can be recognised. The actuator discs are modelled as circular, infinitely thin surfaces, while no local grid refinement is applied. The computational domain size and mesh details used in the numerical simulations, of the present section, are presented in table 7-3.

Table 7-2: Flow characteristics of the kite system, under steady flight, used in the numerical simulations.

\bar{u}_w [m/s]	TI	v [m^2/s]	Re_c	Flight height [m]	AoA [$^\circ$]
7.8	8%	1.79E-05	6.71E+06	140	10

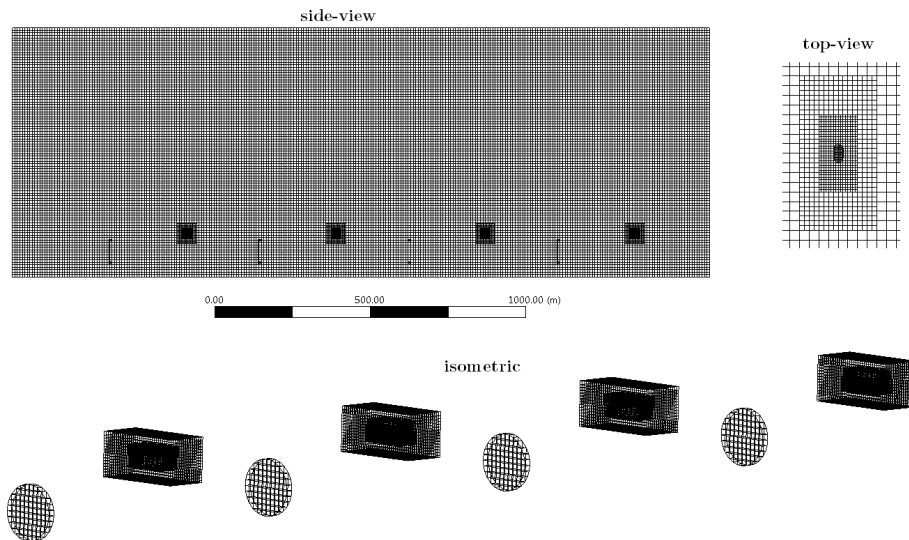


Figure 7-5: Mesh of the computational domain including the kite system and detailed view of the successive mesh refinement around the kite area. The hexahedral cells at the kite surface are of 1m length in all directions ($\Delta x = \Delta y = \Delta z = c/16$).

Table 7-3: Size and mesh details of the computational domain

Parameter	Value
Domain width: Lz	10D
Domain height: Ly	10D
Domain length: Lx	28D
Turbine spacing	6D
Kite x-placement	3D downstream the discs
Kite y-placement	D/4 above the discs
Cell spacing [m]	8 (D/10)
Cell refinement @ kite area	c/4 to c/8 to c/16
Computational load (s/time-step)	50
Total nodes count	3,345,412

7-4 Numerical simulation results

In the present section the results for a wind turbine array including the kites, modelled as body forces, are presented. All presented simulation results are evaluated for the same computational time with identical inflow velocity profiles (generated in the ABL section) and cfd solver settings. A total of three flowthrough passes are simulated (statistics are gathered for the latter two) while the flowthrough time is calculated as: $t = x/\bar{u}_{hub,\infty} = 2240m/5ms^{-1} \sim 448s$. Three flow passes require 1340s or 13400 time-steps for a time-step size $\Delta t=0.1s$ and an average of 8 days of computational time/test case. The kites under steady flight ((b) in figure 7-4) are with numerical simulations in cases (a),(b) & (c). A simplified approach of kite flight, yielding a higher apparent wind velocity and therefore higher power density (power/ m^2) is presented in case (d) of the numerical simulations.

(a) DSE report methodology & Kite facing study

The purpose of this test case is to replicate the configuration proposed in the DSE report [3] and compare the obtained numerical simulation results with the results of their analytical approach. In the DSE report a "reverse engineering" approach was followed to obtain the geometrical and aerodynamic characteristics of the kites. The starting point was the desired efficiency increase of 3% for a two wind turbine array. With the already known parameters of: the mean average velocity and the efficiency of the OWEZ wind farm, as reported in measurement campaigns, they were able to estimate the velocity deficit for the second turbine in a row. *Note: Though already questionable, their approach will be summarized without any comments on the assumptions made. We are only interested in breaking down the approach in order to be able to replicate it in terms of the applied forcing on the flow.* After the estimation of the velocity deficit in the wake of the first turbine, the array was scaled up to four wind turbines and the total mass flow that needed to be diverted in the wake was estimated, given the required efficiency increase. After introducing correction factors on the required mass flow rate (i.e. mixing efficiency, jet expansion, wind direction) the lift force for a single kite was calculated: $L = \dot{m}U_{\infty} \sin \varepsilon$, with ε the downwash angle. Assuming an angle of attack of 10° the downwash angle was calculated (eq. 2-4). Using the formulation of the lift generated

by a wing surface, for a lift coefficient, they were able to determine the required surface area of the kites: $A_{kite}=105m^2$. Though the reaction of the lift force on the flow is the one to generate a vertical velocity component, the adverse effects of the aerodynamic drag (horizontal component in the -x direction) was ignored. To help visualize the effects of the configuration you can imagine a kite rotated by 180° around the yaw axis (figure 7-6a). For the sake of comparison the downwash generated from a kite facing the wind, due to the reaction of the net aerodynamic forces (both lift and drag) on the flow, is simulated (7-6b) and the differences in power extraction and predicted efficiency are presented. The body force, due to the lift and drag on the kite, on the flow for case (a1) is calculated as: $F_{a,case(a1)} = L \cos \varepsilon + D \sin \varepsilon$. For case (a2) on the other hand: $F_{a,case(a2)} = L \cos \alpha - D \sin \alpha$.

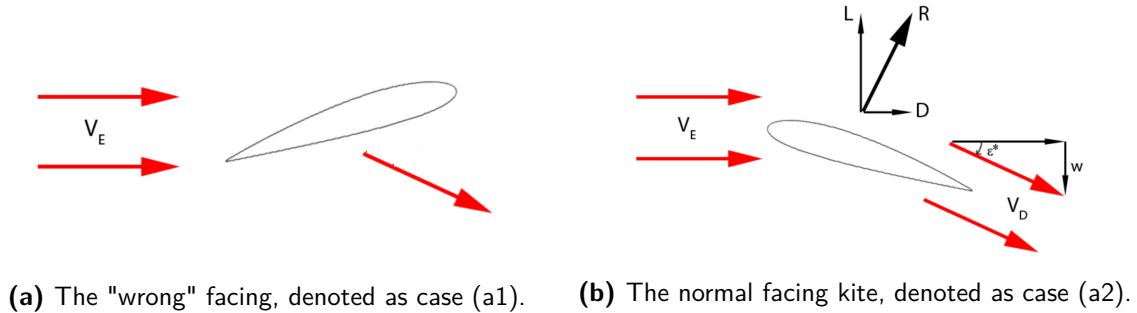


Figure 7-6: Visualization of the kite facing configurations

Table 7-4: Case (a) results: Simulation results after the introduction of the kite system. The effect of two facing configurations for a $105m^2$ kite surface is treated in the test case. The base case results, before the introduction of the kites, are presented in the bottom line.

ADM-R		AD1	AD2	AD3	AD4		efficiency [%]
case (a1) "DSE"	\bar{u} [m/s]	5.817	4.371	4.339	4.498		
	C_T'	0.841	0.815	0.819	0.832		
	Thrust [N]	-87,633	-47,945	-47,502	-51,800		
	Power [W]	509,734	209,587	206,123	232,984	1,158,429	56.8
case (a2)	\bar{u} [m/s]	5.819	4.368	4.298	4.434		
	C_T'	0.841	0.814	0.824	0.822		
	Thrust [N]	-87,700	-47,809	-46,862	-49,743		
	Power [W]	510,364	208,840	201,418	220,577	1,141,199	55.9
base case	Power [W]	502,872	202,249	176,275	218,591	1,099,987	54.7

When comparing the simulation results for the cases presented in table 7-4 a difference of 1.5% in power extraction and 1% difference in array efficiency is predicted. Though the difference in power predicted values is insignificant, the kite facing presented in case (a2) is adopted for the future simulations. Regardless of the kite facing configuration, an increase of 3.6%-5% in total extracted power from the domain is predicted after the introduction of the kites. It is the first indication of the potential gains in energy production with the use of suspended kites in a wind turbine array. The wind-turbine array efficiency increase predicted from the DSE report, in spite of the assumptions introduced in the analytical model, falls within a 2% uncertainty margin (DSE=4.3%, CFD=1-2%) from the numerically simulated test case and is considered a good first-order estimation. An argument to support the higher efficiency claims

in the DSE report is the fact that a slightly larger kite surface was assumed, $128m^2$ vs $105m^2$, and the thrust coefficient for the wind-turbines was $C_{T,DSE}=0.62$ relative to the simulated where $C_T=0.56$. The effects of different loading factors on the array efficiency increase are treated in test case (c).

In numerical simulations one could argue though, that the 1-2% change in the prediction of a variable could very well fall within the uncertainty introduced by physical modelling errors (mathematical model, boundary conditions), discretization errors (spatial and temporal discretization, truncation error), programming and computer round-off errors. Therefore, apart from the inquisitive urge to simulate additional kite configurations, in the following sections an attempt to further on increase the array efficiency beyond the uncertainty margins of the numerical setup is attempted.

(b) Kite sizing: $A_{kite,s}$ & $A_{kite,l}$

The effect of different kite sizes is evaluated in the present section. Essentially the same force/unit-area is applied over a larger surface area in the domain to qualitatively compare the effects on wake velocity recovery and kinetic energy flux relative to case (a2). A kite with twice the dimensions of the kite surface presented in case (a2) is simulated. The projected surface area of the large kite on the y-z plane is $470m^2$. First and second order statics of the wake flow are compared for the base case (without kites), case (a2) with the $A_{kite,s}=A_{AD_i}/48=105m^2$ kite surface and the latter one with the $A_{kite,l}=A_{AD_i}/12=470m^2$ kite. The facing of the kites in the present and all upcoming case studies is identical to the one presented in case (a2).

For a mean velocity, at kite flight height of 140 meters, of 7.8m/s, a total force of 18.5kN is calculated (explained in section 7-2 and presented in Appendix-C), for the $470m^2$ kite surface, which by basic unit transformations is converted into extracted power since $F_a=P/V_\infty$ where P equals 143kW or $300W/m^2$. Power densities up to $7kW/m^2$ for the SkySails [90] and $3.7kW/m^2$ the Anurac [91] designs are nowadays claimed for kite surfaces of $320m^2$ and $400m^2$ respectively. The $25m^2$ TU Delft AWE system [92], as reported in 2011 achieved a mean power density of $260W/m^2$ operating at 13m/s of wind velocity which, is as efficient as the proposed kite design. It is therefore clear that, with the advances of materials and kite designs reaching gliding ratios of $L/D=10$, a rather conservative approach is adopted for the aerodynamic performance of the proposed kite system.

A comparison of three flow statistics (mean streamwise velocity deficit: $\bar{u}/U_{hub,\infty}$, mean streamwise turbulence intensity: \overline{TI}_x , normalized mean kinetic energy flux: $\bar{\Phi}/U_{hub,\infty}^3$) is presented in the present section. The results are plotted at a streamwise distance $x/D=5$ for the base case of the actuator discs with added swirl (ADM-R) before and after the introduction of the kites. A trend towards a faster mean velocity recovery with increasing kite surface downstream the discs is predicted (figure 7-7). The velocity deficit reduces significantly after the introduction of the kites at a rate of 10% & 30% for the $A_{kite,s}$ and $A_{kite,l}$ surface sizes respectively. An important observation is the fact that the area of the flow exhibiting significant velocity recovery increases with increasing kite size, eventually affecting a larger rotor area. Though significant, the velocity recovery, for both kites, is limited to the top 3/4 of the wind turbine surface area. It would, therefore, be of particular interest to evaluate the effect of higher kite power densities (case (c)) on the wake flow in terms of disc area to benefit from the faster recovery.

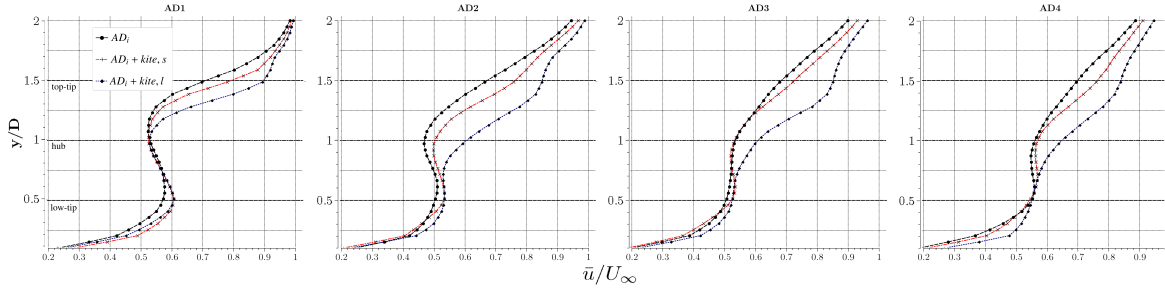


Figure 7-7: Normalized x-velocity plots at a downwind distance of 5 rotor diameters ($x/D=5$) for the actuator discs. The simulation results of the two simulations using the ADM-R concept before and after the introduction of the kite system are presented.

Second order statistics i.e. turbulence intensity levels are typically used to characterize mixing in the wake flow. The TI_x plots presented in figure 7-8 indicate a reduction in the turbulence levels in the wake for the simulations including the kites. The unexpected reduction in the turbulence levels in the wake is $\sim 12\%$ on average for $A_{kite,s}$ and $\sim 30\%$ on average for the $A_{kite,l}$ case. A contour plot of the turbulence levels in the wake for all three cases is also presented to provide a better understanding of the generated turbulence in the vicinity of the kites. As expected turbulence intensity levels increase in the vicinity of the kites to a maximum of 35% but dissipate quickly resulting in lower total TI values in the wake, when compared to the base case, at a downwind distance of five rotor diameters (figure 7-9). The rapid dissipation of generated turbulence is attributed to the dissipative nature of the Smagorinsky model on the smaller eddy scales. It is therefore not associated with the presence of the forcing on the flow rather the local grid changes in the vicinity of the kite surface.

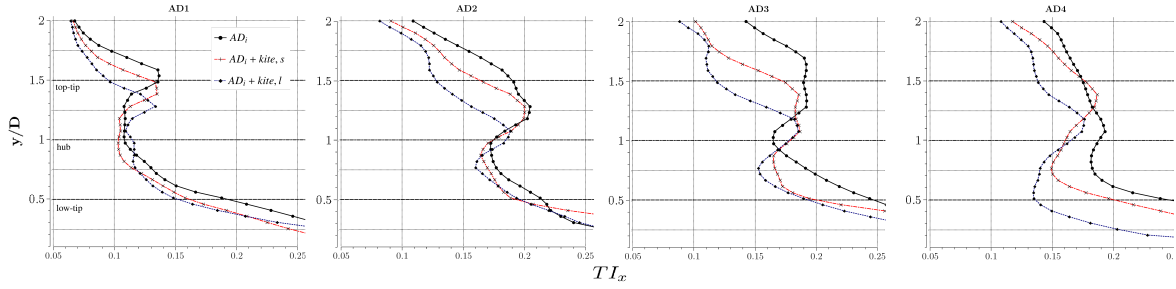


Figure 7-8: Turbulence intensity profiles at a downwind distance of 5 rotor diameters ($x/D=5$) for each one of the actuator discs. Comparative plots of the base case only with the ADM-R, ADM-R + $A_{kite,s}$ & ADM-R + $A_{kite,l}$.

The analysis of the x-component of turbulence intensity does not provide conclusive information about the mixing in the shear layer. The Reynolds shear stresses uv , uw and vw on the other hand is demonstrated [17] that they are responsible for the flow kinetic energy transport and must be taken into consideration for evaluating the turbulent mixing. To characterize mixing in the wake region, the spatial gradient of the flux of mean flow kinetic energy is evaluated in the x-y plane as: $\bar{\Phi} = -\bar{u}(u'v')$. The comparison of the normalized streamwise mean flow kinetic energy flux in the radial direction as plotted in 7-10 shows clearly the higher

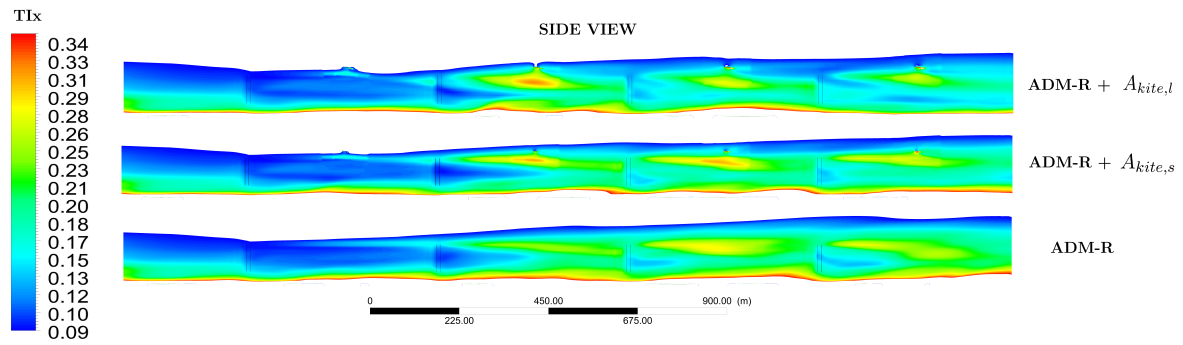


Figure 7-9: Contour plots of TI_x values for the ADM-R and ADM-R + kite systems.

magnitude of kinetic energy entrainment in the shear layer after the introduction of the kite system. A significant increase in the entrainment of the free-stream kinetic energy into the wind turbine wake before " AD_i " and after " AD_i+kite " the introduction of the kite is observed (black vs coloured lines). The effect of different kite surface areas, $A_{kite,s}$ (dashed red line) and $A_{kite,l}$ (dotted blue line), on the spatial distribution and magnitude of the mean kinetic energy flux is of particular interest. At $x/D=5$ downwind the discs an average increase of 27% and 50% on the mean KE flux is estimated after the introduction of the kite system, for $A_{kite,s}$ and $A_{kite,l}$ respectively, relative to the base simulation.

The results of the kite sizing study are presented in table 7-5. The total extracted power predicted for the wind turbine array with the larger kite surface ($A_{kite,l}$) is 11% higher relative to the one the smaller kite surfaces ($A_{kite,s}$). A substantial increase in the array efficiency value is also predicted; 7% higher with $A_{kite,l}$ relative to the $A_{kite,s}$ case. Relative to the base case (without kites) an increase in total extracted power of 14% and array efficiency values of $\sim 8\%$ is predicted. We can therefore conclude that, increasing the kite surface to $A_{kite,l}=A_{AD_i}/12$ results in a 50% increase in the flux of the mean kinetic energy entrained into the wake region, which is translated into faster wake velocity recovery and increased power production of the downstream turbines.

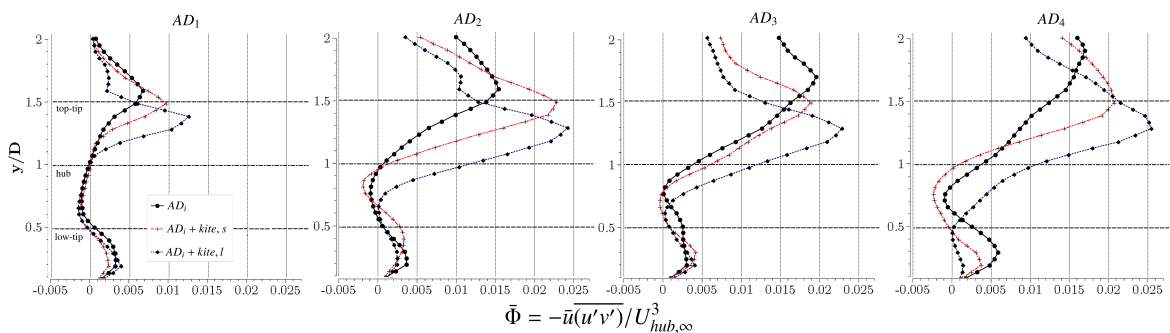


Figure 7-10: Radial profiles of the normalized mean flow-kinetic energy flux, $\bar{\Phi}$, evaluated on the horizontal x - y plane and plotted at $x/D=5$ downwind the actuator discs AD_i for the different kite sizes.

Table 7-5: Case (b) results: Simulation results of the case with the $A_{kite,l}=470m^2$ kite system. Power and efficiency values are also presented for case (a2) and the base case.

ADM-R		AD1	AD2	AD3	AD4		efficiency [%]
case (b)	\bar{u} [m/s]	5.816	4.536	4.742	4.709		
	$C_{T'}$	0.841	0.812	0.833	0.832		
	Thrust [N]	-87,614	-51,423	-57,692	-56,810		
	Power [W]	509,565	233,254	273,574	267,520	1,283,912	62.9
case (a2)	Power [W]	510,364	208,840	201,418	220,577	1,141,199	55.9
base case	Power [W]	502,872	202,249	176,275	218,591	1,099,987	54.7

As already noted, the substantial wake velocity recovery concerns the top 3/4 of the disc area associated with the peak in the predicted kinetic energy flux in the wake region. In an attempt to increase the disc area, affected by the enhanced vertical momentum transport, we examine higher power density values (P/m^2) for $A_{kite,l}$ in test case (d). In case (c) the effect of different wind turbine loading factors, $C_{T'}$ on the flow statistics is examined.

(c) ADM-R & $A_{kite,l}$ under partial and optimal load

The effect of the $A_{kite,l}=470m^2$ kite surface on the wake generated by turbines operating under partial and optimal load conditions is studied in the present section. The base cases, without the kites, for optimal and sub-optimal loading conditions characterized by $C_T=0.88$ & $C_T=0.56$ were presented in case (c) of section 6-2 and are used as reference for the present section.

The work-flow of estimating the pressure jump coefficient f_n used in FLUENT is by calculating $C_{T'}$ (eq. 6-2) for the desired C_T values and in turn the pressure drop ΔP from eq. 6-5 for each one of the discs. The predicted velocity values, averaged over the disc area, are substituted in u_D . It is easily understood that the pressure drop at the discs is proportional to the square of the velocity at the discs u_D , therefore $N=3$ is used when solving for f_n in eq. 6-6. The averaged disc velocities obtained for the base case simulations of case (c) (section 6-2) are used as a reference for the calculation of f_n . The calculated parameters and FLUENT pressure drop coefficient f_n are presented in table 7-6. The negative sign for f_n indicates the desired pressure drop in the streamwise direction.

Table 7-6: Reference parameters used in the simulations for the partial and optimal load cases with the $A_{kite,l}$.

ADM-R		AD1	AD2	AD3	AD4	f_n
$C_T=0.56$ / $C_{T'}=0.85$	\bar{u} [m/s]	5.799	4.317	4.129	4.419	
	ΔP [Pa]	20.8	11.5	10.6	12.1	-0.62
$C_T=0.88$ / $C_{T'}=1.98$	\bar{u} [m/s]	4.776	3.116	3.590	3.502	
	ΔP [Pa]	27.6	11.7	15.6	14.8	-1.21

The effect of the turbine loading on the flow statistics, after the introduction of the $A_{kite,l}$, is presented. The large kite with projected surface area of $470m^2$ with the same pressure jump

is used for both simulations. Vertical profiles of the mean velocity, turbulence and kinetic energy flux are evaluated at a downstream distance of $x/D=5$ for each one of the actuator discs.

Higher wind turbine loading ($C_T=2$) is associated with more energy extracted from the wind translated into more pronounced wake velocity deficit in the wake of the discs, predicted for the ADM-R $C_T=0.88$ & $A_{kite,l}$ case relative to the ADM-R $C_T=0.56$ & $A_{kite,l}$ case. The normalized mean x-velocity profiles at a downwind distance of $x/D=5$ and $x/D=-1$ (inflow for the discs) are plotted in figure 7-11. As a result of the higher loading factor, a much more pronounced wake velocity deficit is observed downwind AD1, relative to the partial loaded case. Similar to the partial/optimal loading wake characteristics of the base case (without the kites) the wake flow appears to move towards an equilibrium state as we move further downstream in the domain. Wake velocity recovery for the partial loaded turbines stabilizes to about $0.6U_{hub,\infty}$ at $x/D=5$ and to $0.5U_{hub,\infty}$ for the discs under optimal load. Interestingly, if we compare the recovery characteristics with the base case (figure 6-18) for AD3 and AD4 the same wake velocity recovery is predicted for the higher loaded discs before and after the introduction of the kites. For the partial loaded discs on the other hand the effect of the kite surface is much more pronounced and wake velocity recovery is enhanced also for AD4.

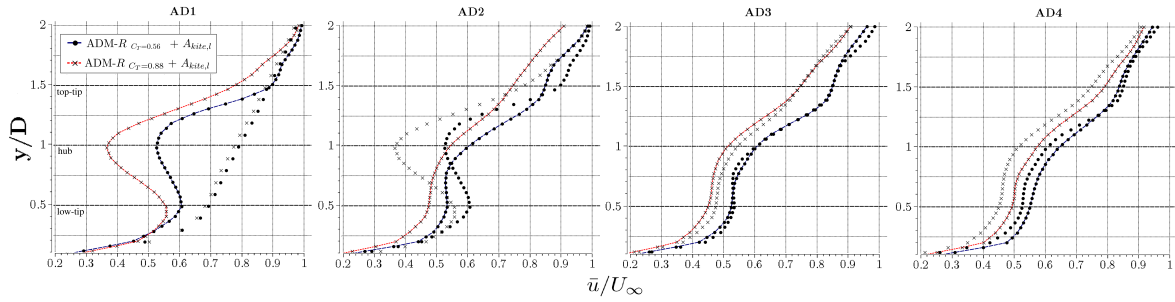


Figure 7-11: Normalized x-velocity profiles at a downwind distance of 5 rotor diameters ($x/D=5$) for the actuator discs. The x-crosses represent the velocity profiles at $x/D=-1$ for $C_T=0.88$ & the dotted (no lines) for $C_T=0.56$. The effect of different wind turbine loading on the wake velocity, including the $A_{kite,l}$ surface, is plotted.

Turbulence intensity profiles are plotted at $x/D=5$ for both loading cases in figure 7-12. TI profiles at the inlet of the discs ($x/D=-1$) are also presented for reference. As expected turbulence levels in the wake of the turbines operating under higher loading are more pronounced relative to the partial loading case. The added turbulence due to higher loading of the discs is translated to total TI levels of twice the magnitude at the centre of the wake downstream AD1 relative to the ambient conditions. The effect of the kite surface on the added turbulence levels is easily identified downstream AD3 and AD4. Further downstream in the domain, turbulence levels for higher loaded turbines, after the introduction of the kites, are constantly higher when compared to the partial loaded case in a much more pronounced fashion relative to the base cases, see figure 6-19.

The vertical transport of momentum from the free-stream flow in the turbine canopy is quantified in terms of the normalized flux of mean flow kinetic energy $\bar{\Phi}$ in the radial direction [17]. The effect of higher wind turbine loading on the entrainment of kinetic energy in the wake is plotted in figure 7-13. The higher added turbulence levels predicted downstream AD1

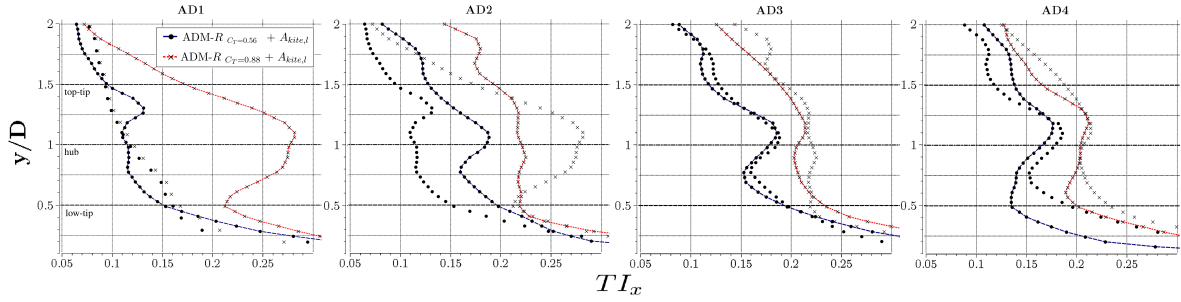


Figure 7-12: Comparative plots of different loading for the turbine using the ADM-R model. Turbulence intensity profiles at a downwind distance of 5 rotor diameters ($x/D=5$) for each one of the actuator discs. The x-crosses represent the velocity profiles at $x/D=-1$ for $C_T=0.88$ & the dotted lines for $C_T=0.56$. The $A_{kite,l}=470m^2$ is used to simulate the kite surface in the flow.

are translated into higher values of vertical momentum flux as well assisting the recovery of the wake velocity. The effect of different wind turbine loading does not appear to affect the vertical transport of momentum, downstream the latter three discs (AD2, AD3 & AD4), similar to the results reported before the introduction of the kites. When compared to the base cases (figure 6-20), the magnitude of the kinetic energy flux is on average four times larger in the wake region for both loading cases.

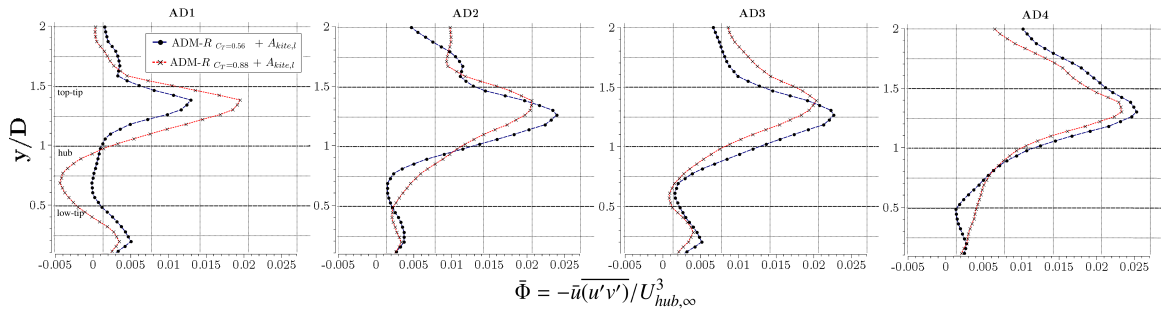


Figure 7-13: The radial profiles of the normalized mean flow-kinetic energy flux, $\bar{\Phi}$, are evaluated on the horizontal x-y plane. $\bar{\Phi}$ is plotted at $x/D=5$ downwind the actuator discs AD_i under partial and optimal load after the introduction of the $A_{kite,l}$.

An understanding on coherent structures present in the wake region from the patterns typically seen in a so called "plane mixing layer" as discussed by Finnigan [93]. A mixing layer is obtained by initially letting two airstreams of different velocity be separated by a splitter plate at $z=0$. The velocity fields is found to have an inflection point at $z=0$, which is the level of maximum shear between the two initial streams resulting in a peak in the shear production of Turbulence Kinetic Energy (TKE) at this level. It is also the level where the velocity variances σ_i^2 and shear stresses reach their maximum value. Turbulent momentum flux has the same effect as a shearing stress. The turbulent shearing stress is that given by the turbulent momentum flux and is described as: $\tau_{turb} = -\rho u'w'$. The inflection point ($z=0$) can be recognized at the top 3/4 of the wind turbine wake flow, downstream AD3/AD4, in the wake velocity (figure 7-11), turbulence intensity (figure 7-12) and kinetic energy flux (figure 7-13).

The extracted power and efficiency results for the partial and optimal loaded turbines with kites are presented in table 7-7 and compared to the predicted power and efficiency results from before the introduction of the kites. Relative to the base cases (without $A_{kite,l}$) presented in case (c) section 6-2, a 14% increase in the extracted power for the partial loading case is predicted and a 5.5% increase for the optimal loading case. The power extraction gains due to the presence of the kite surface are, therefore, much more pronounced when the turbines are operating with partial load factor. For the discs with the higher thrust values the increase in the array efficiency is 2.5% while for the partially loaded discs the increase is 8.2%. Due to the substantial difference in the predicted array efficiency increase for the two disc loading cases and the small efficiency increase for the case with $C_{T'} \sim 2$, additional cases considering only the higher loaded turbines are evaluated. The large kite surface size is used ($A_{kite,l}=470m^2$) with higher power densities (P/m^2) translated into larger resultant forces on the wake flow. Higher power densities could be realised with a more aerodynamically efficient wing under steady flight or by increasing the velocity at the wing surface. The latter option is realized in the following section, approximating higher velocities (higher pressure jump) with a kite in motion.

Table 7-7: Case (c) results: Simulation results of the different wind turbine loading cases, for the actuator disc with rotation (ADM-R) with the $A_{kite,l}=470m^2$ kite system.

ADM-R	Kite		AD1	AD2	AD3	AD4		efficiency [%]
$C_T=0.88$	$A_{kite,l}$	\bar{u} [m/s]	4.790	3.312	3.734	3.500		
		$C_{T'}$	1.952	1.890	1.943	1.917		
		Thrust [N]	-137,869	-63,846	-83,400	-72,318		
		Power [W]	660,340	211,482	311,421	253,143	1,436,386	54.4
$C_T=0.88$	\emptyset	Power [W]	652,947	174,404	273,924	253,414	1,354,690	51.9
$C_T=0.56$	$A_{kite,l}$	Power [W]	509,565	233,254	273,574	267,520	1,283,912	62.9
$C_T=0.56$	\emptyset	Power [W]	502,872	202,249	176,275	218,591	1,099,987	54.7

(d) ADM-R $C_T=0.88$ & $A_{kite,l}$ - varying power density

In the present section the effects of large surface kites, $A_{kite,l}$, with increasing power densities (W/m^2) on the wake flow are evaluated. The actuator disc model with rotation (ADM-R) under optimal loading ($C_{T'}=2$) is used to simulate the wind turbines in the computational domain. To physically interpret the effect of larger forcing on the wake flow we make the assumption of kites in motion. The airspeed of the kite or otherwise referred to as apparent wind velocity is determined by the wind speed u_w , the kites glide angle and the elevation angle β , see equation 7-6. Higher apparent wind velocity results in higher pressure difference between the upper and lower surface of the kite yielding the desired resultant force. In the results presented in the previous sections, for kites in steady motion, the wind velocity at kite flight was equal to the apparent wind velocity of 7.8 m/s, yielding a total resulting force on the flow of 18.5 kN. Two new simulations are set-up to evaluate a two- and four-fold increase in the resulting force on the flow amounting to 37kN and 74kN respectively.

For the purposes of tethered wings, meant for AWE applications, a L/D ratio can be achieved that is about equal to the AR. An increase in the L/D ratio above the AR factor to about 1.5

can be achieved by -quoting Storm Dunker- [88] " more elliptical plan-form shape, specialized low-vortex wingtip designs". For an AR=2 the maximum L/D ratio that could theoretically be realized would therefore be $L/D \sim 3$. As already discussed the maximum crosswind velocity, downwind the tether attachment point, can be approximated by multiplying the wind speed with the L/D ratio. Assuming the max increase in the L/D ratio of 1.5 and a limiting factor of $L/D=3$ we can calculate the maximum theoretical flight speed of u_a from eq. 7-7 [41].

$$u_a = \frac{2C_R}{3C_D}v_w \quad (7-7)$$

where: C_R the resultant aerodynamic force vector. For $C_L=1.1$ & $C_D=0.37$ the limiting factor of $L/D=3$ is approximated. For the same lift and drag coefficients, $C_R=1.16$ and the maximum allowed apparent velocity of $u_{a,max}=16.3$ m/s is calculated, see eq. 7-7 for $v_w=7.8$ m/s. Practical problems or limitations due to the large kite size are beyond the focus of the present study. For the given apparent velocity the the maximum tether force is calculated as $F_{t,max} \sim 90$ kN, see eq. 7-5. Since the values of the total forces (37 & 74kN) are within the theoretical potential of the kite surface, on the flow we can solve equation 7-5 for u_a for a rough approximation of the apparent kite velocity. A more systematic approach involves the modification of eq. 7-1 to account for the relative kite motion; V_∞ is replaced with the apparent velocity u_a . Trial and error method: for known pressure coefficient distribution (Appendix C table C-1), and by iteratively changing the apparent velocity u_a we reach the magnitude of the total force on the flow. The apparent velocities of 11.1m/s & 15.6 were found for the desired total forces of 37kN & 74kN respectively. For a constant glide angle $\epsilon=10^\circ$ (or angle of attack) the elevation angle β was approximated from eq. 7-6. Assuming that power is produced with perfect efficiency, the power density is calculated as $P' = F_a u_a / A$. A summary of the proposed configurations is presented in table 7-8.

Table 7-8: Kite flight parameters used to simulate the different kite power densities.

	F_a [kN]	ΔP [Pa]	U_w [m/s]	ϵ [°]	β [°]	U_a [m/s]	P' [W/m ²]
$A_{kite,l-39}$	18.5	39	7.8	10	80	7.8	307
$A_{kite,l-79}$	37	79	7.8	10	43.8	11.1	873
$A_{kite,l-157}$	74	157	7.8	10	29.5	15.6	2456

The "fan" boundary condition with a constant pressure jump of 79 & 157Pa is specified, for a kite surface of $470m^2$, to simulate the desired 37 & 74kN of total force respectively. As already stated, the applied forcing does not claim to represent the dynamics of kite flight but act as a proof of concept to inform future designs and research. The effect of higher kite power densities on the wake velocity profiles is evaluated at $x/D=5$ downwind the actuator discs and presented in figure 7-14. As expected, faster velocity recovery is associated with higher forcing on the flow. Doubling the force magnitude, $A_{kite,l-79}$, results in a 20% faster recovery relative the base case (ADM-R+ $A_{kite,l-39}$) at hub height for AD3 and AD4. At the same height, quadrupling the force $A_{kite,l-157}$ results in an average 50% increase in the velocity recovery five rotor diameters downstream the latter two simulated turbines.

The effect of higher forcing on the flow in terms of turbulence intensity profiles in the stream-wise direction, TI_x , is plotted in figure 7-15. Similar to the trend visualized in figure 7-9,

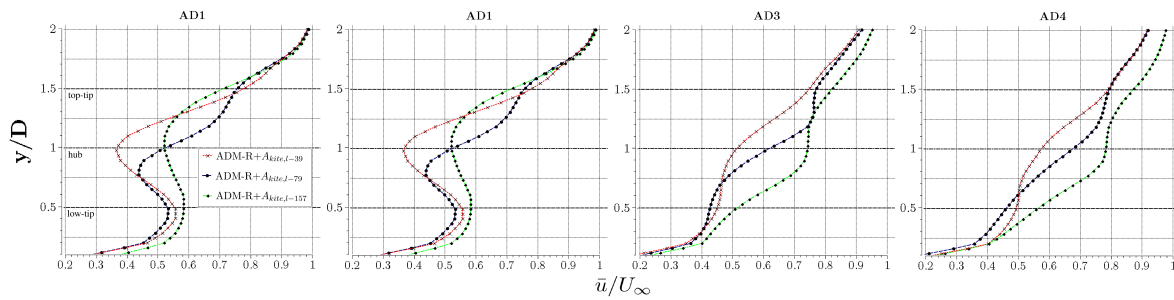


Figure 7-14: Normalized x-velocity profiles at a downwind distance of 5 rotor diameters ($x/D=5$) for the actuator discs under optimal load ($C_T=2$). The effect of different kite power densities, on the wake velocity, is plotted.

turbulence is enhanced in the vicinity of the kites and is quickly dissipated into heat before $x/D=5$. Enhanced turbulent mixing in assists the entrainment of vertical momentum and the re-energizing of the wake. The dampening of the wind shear due to the strong vertical velocity component results in a more blunt streamwise velocity profile and lower turbulence intensity values for the higher forcing cases.

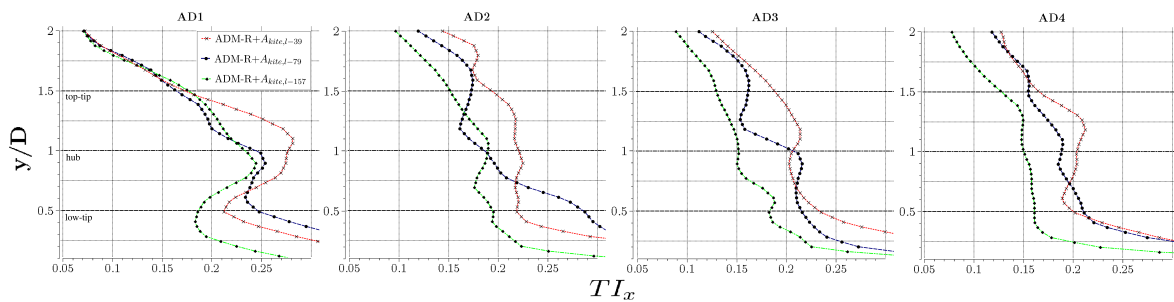


Figure 7-15: Turbulence intensity profiles at a downwind distance of 5 rotor diameters ($x/D=5$) for each one of the actuator discs (ADM-R, $C_T=0.88$). The $A_{kite,l}=470m^2$ with different power densities is used to simulate the kite in the domain.

Interesting conclusions can be drawn when examining the mean flow-kinetic energy flux in the radial direction (figure 7-16). The vertical $\bar{\Phi}$ profiles indicate that higher power densities are associated with fluctuations in the vertical momentum transport that affect a larger turbine area relative to the base case, $A_{kite,l=39}$. Similar trends are expected for the shear stress and turbulence kinetic energy (TKE) transport. Horizontal oscillations in the magnitude of vertical momentum flux, for the high kite power densities, are identified as regions of high TKE production (right part) and dissipation (left part) which is shown to suppress turbulence levels in the wake region, see figure 7-15, and enhance the re-energizing of the wake velocity, see figure 7-14.

Significantly higher kinetic energy flux in the wake region is translated in more available energy to be extracted from the wake flow. For the wind turbine array with the highest power density kites, $P'=2456 [W/m^2]$, a 24% increase in power production and a 15% increase in efficiency is predicted relative to the base case without kites and the actuator discs operating under

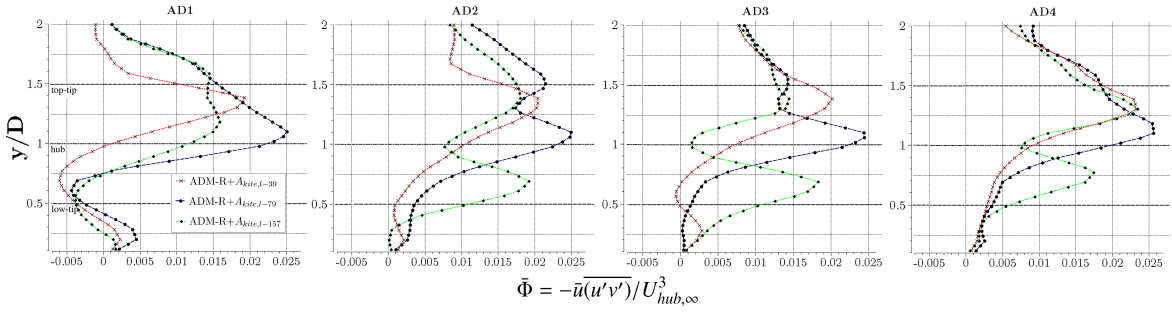


Figure 7-16: The radial profiles of the normalized mean flow-kinetic energy flux, $\bar{\Phi}$, are evaluated on the horizontal x-y plane. $\bar{\Phi}$ is plotted at $x/D=5$ downwind the actuator discs (ADM-R) under optimal load after the introduction of the $A_{kite,l}$ with three different power densities.

optimal loading, $C_T'=2$. The use of kites with power density, $P'=873 [W/m^2]$, results in an efficiency increase of $\sim 7\%$ relative to the case with the lowest power density kites.

Table 7-9: Case (d) results: Simulation results for the large kite surface $A_{kite,l}=470m^2$ and high power densities, using the actuator disc with rotation (ADM-R) under optimal loading $C_T'=2$.

ADM-R	$A_{kite,l} [W/m^2]$		AD1	AD2	AD3	AD4		efficiency [%]
$C_T=0.88$	2456	\bar{u} [m/s]	4.787	3.479	4.203	4.190		
		C_T'	1.952	1.893	1.943	1.906		
		Thrust [N]	-137,738	-70,545	-105,672	-103,036		
		Power [W]	659,445	245,418	444,189	431,764	1,780,817	67.5
$C_T=0.88$	873	\bar{u} [m/s]	4.791	3.559	3.953	3.811		
		C_T'	1.952	1.916	1.951	1.938		
		Thrust [N]	-137,939	-74,715	-93,900	-86,659		
		Power [W]	660,881	265,933	371,235	330,235	1,628,283	61.6
$C_T=0.88$	307	Power [W]	660,340	211,482	311,421	253,143	1,436,386	54.4
$C_T=0.88$	\emptyset	Power [W]	652,947	174,404	273,924	253,414	1,354,690	51.9

7-5 Discussion

A comprehensive study of a wide range of parameters to affect the wake flow in terms of different kite configurations were examined. The presence of a kite placed in-between the actuator discs appears to highly affect the extracted power from the wind turbine array. It is shown that it effectively diverts the free-stream flow above the discs and enhances the entrainment of kinetic energy from the lower parts of the ABL into the wind turbine canopy. Two kite sizes were evaluated denoted as $A_{kite,s}$ & $A_{kite,l}$ with a surface area 48 & 12 times smaller relative to the wind turbine area respectively. Increasing the size and power density (assuming a crosswind motion) of the kite is shown to assist wake velocity recovery and in turn yield higher power outputs for the turbines. The effect of the kite is also shown to be lower when the turbines operate under optimal loading relative to the partial loading case. This could give way to control strategies of sub-optimal operation for the turbines, decrease loading and compensate the lower energy extraction with the use of kites. The power extracted values are the only ones that can be compared between the different simulations. The efficiency of the array was calculated based on the power extracted by the first turbine which was different

between the cases studies. Efficiency values are presented, though, and compared when P_{AD1} is identical for different test cases. Utilizing the larger surface area is shown to increase power extraction by 2.5% relative to the base case (without kites) for the turbines operating under optimal load. The array efficiency increase is shown to depend on the magnitude of the vertical forcing on the flow and was predicted to +7.5% & +12.5% for two and four times increase relative to the $ADM-R+A_{kite,l-39}=307W/m^2$ case.

The wake flow in the wind turbine array is found to approximate the flow and turbulence characteristics in and above uniform tree or plant canopies which are widely investigated for meteorological purposes [26, 93]. Decades of survey have shown that canopy turbulence is dominated by organized structures of large scale eddies which transfer a vast majority of the momentum both within the roughness sublayer and above [93]. Those sweeps are able to penetrate the canopy which results in a displacement of the zeroplane¹ so that it lays well within the canopy, commonly at 3/4 of the mean canopy height [94]. The inflection point in the velocity field is clearly identified in the predicted wake velocity profiles, presented in the previous section, and coincides with the height where the peak in the vertical kinetic energy flux is observed. Higher forcing on the flow is associated with the vertical translation of the zeroplane, towards the height of the rotor center, enhanced vertical momentum transport and faster wake velocity recovery in the wake region. The downstream region of AD3 & AD4 is of main study interest as the wake flow develops towards an equilibrium state.

¹A mixing layer is obtained by initially letting two airstreams of different velocity be separated by a splitter plate at $z=0$. The velocity fields is found to have an inflection point at $z=0$, which is the level of maximum shear and velocity variances σ_i^2 between the two initial streams.

Chapter 8

Conclusions

The presence of the kites, modelled as a constant forcing on the flow, is shown to significantly affect the spatial distribution of the mean velocity deficit, turbulence intensity and vertical kinetic energy flux in the turbine wakes. Overall, higher forcing on the flow represented by higher kite power densities is associated with faster wake velocity recovery, lower turbulence intensities and enhanced vertical kinetic energy flux. In all cases the highest turbulent fluxes in the wake are found around the upper edge of the wake where the mean shear is maximum; in line with reported literature results [31]. Faster wake velocity recovery (up to 30%) is also associated with increasing kite surface size with identical power densities. Enhanced power extraction is also predicted since a larger rotor surface area is affected by the vertical momentum transport from the undisturbed flow into the turbine canopy.

The wind turbines were modelled with both axial and induction factors, ADM-R, which is considered to yield improved predictions compared to the ADM-NR [32]. The wake flow in the wind turbine array is found to approximate the flow and turbulence characteristics in and above uniform tree or plant canopies which are widely investigated for meteorological purposes [26, 93]. The large scale structures of the flow velocity fields is found to have an inflection point at $z=0$, which is the level of maximum shear and velocity variances σ_i^2 between the two initial streams within the canopy, commonly at $3/4$ of the mean canopy height [94]. In our simulations the sweeps enhanced by the applied vertical forcing penetrate the canopy which results in a displacement of the zero plane (mixing layer separation) at $3/4$ of the disc area. The inflection point in the velocity field is clearly identified in the predicted wake velocity profiles and coincides with the canopy height where the peak in the vertical kinetic energy flux is observed. Higher forcing on the flow is associated with enhanced vertical momentum transport and faster wake velocity recovery in the wake region. Different wind turbine loading factors are shown to significantly affect the effectiveness of the kites. Higher relative efficiency increase is predicted for the sub-optimally loaded rotors in comparison with the optimally loaded ones; an important observation that could pave the way for sub-optimal collective control of wind turbines with the use of kites to provide comparable array efficiencies and mitigate fatigue loads.

Though the main focus of the study is on a qualitative comparison of the mean flow prop-

erties before and after the introduction of the vertical forcing, extracted power and array efficiency results are reported. For the discs with optimal loading factor, $C'_T=2$, the total extracted power for the array was increased by 24% for the largest force magnitude simulated in the domain, $F_a=74\text{kN}$ corresponding to a 470m^2 kite surface with a power density of $P'=2456[\text{W}/\text{m}^2]$. A 16% and 5% increase was predicted for the kites with $P'=873[\text{W}/\text{m}^2]$ and $P'=307[\text{W}/\text{m}^2]$ respectively. Based on the extracted power values from the turbines the wind turbine array efficiency was estimated. The kites with the highest power density are associated with an array efficiency increase of $\sim 16\%$ followed by a 10% and a 2.5% efficiency increase for the remaining two kite power density configurations.

8-1 Recommendations

8-1-1 ABL profiles

- Evaluate the effect of near wall damping functions coupled with LES on the velocity profiles and document the additional computational costs involved. It is generally desirable to have an LES formulation that automatically provides zero eddy-viscosity for flows with laminar turbulent transition, where the Smagorinsky model negatively affects the laminar flow. An alternative near-wall approach available in FLUENT for LES simulations, based on the work of Werner and Wengle [95, 96]. The Werner-Wengle wall functions can be enabled using the "`define/models/viscous/near-wall-treatment/werner-wengle-wall-fn`" text command. An additional one is the Embedded/Zonal LES (ELES, ZLES) [67] approach part of the hybrid Scale-Resolving Simulation (SRS) in FLUENT. The domain is explicitly split into a RANS and a LES portion beforehand and for the in-between regions the turbulence model is switched from RANS to LES/WMLES. The boundary layers are covered by a RANS model and the mixing layer by a LES model.
- Determine the boundary layer profiles of the mean velocity and turbulence kinetic energy (TKE) for the neutral ABL with ADMS. Atmospheric Dispersion Modelling System (ADMS) can be used to determine the mean velocity and TKE values which are later on used in FLUENT, as inflow boundary conditions, with the use of User Define Functions (UDF) [52]. For flat terrain simulations, the ADMS boundary layer structure is defined in terms of the Monin Obukhov length, boundary layer height and surface roughness [97].

8-1-2 Wind turbine array with kites

- Increase the size of the computational domain and the number of simulated turbines using the ADM-R model. Evaluate the effect of the kites when placed in an "infinitely large" wind farm operating in a fully developed atmospheric boundary layer. The contribution of the kites can only be verified after an equilibrium between the forces in the flow (wind turbine drag vs vertical transport of energy) has been reached.
- Investigate the effect of different vertical and streamwise locations for the kites, for a range of wind turbine loading conditions, and characterize the wake re-energizing

process. The temporal evolution of far-wake turbulence and mean-flow kinetic-energy transport need to be captured in order to guarantee statistical convergence in case only time-averaged results are of interest.

- Though the original goal of the study was to provide a qualitative insight into the mean flow statistics after the introduction of the kites in the array, the simulated cases and the vast amount of data collected would be fully utilized only in the case of a quantitative description of the flow parameters in the time-domain. The results could, therefore, be expanded to fully utilize the LES sets by considering the temporal and spatial coherency of the parameters in the evolving flow field.
- A step further would be the identification of flow patterns of the flow field by using a set of "snapshots" of the 3D velocity field at prescribed points in time. In that case proper orthogonal decomposition (POD) analysis [98], would be needed to quantitatively describe the flow patterns in the LES domains. Using the flow structures identified by the POD analysis, we could understand the effect of largest turbulence structures on the vertical entrainment of kinetic energy within the simulated wind turbine array and compare it with the LES domain including the kite surfaces.

Appendix A

UDF - Read velocity profiles

A-1 FLUENT on the HPC12 cluster

To perform all the calculations in an efficient manner, a queuing system is used in the HPC12 cluster. PBS is a job resource manager. A job is defined as a computational task such as a computational simulation or data analysis. PBS provides job queuing and execution services in a batch cluster environment (i.e. running jobs not through a (graphical) interface. To link your computer to the HPC12 you need a SSH connection. Refer to the instructions from Sander van Zuijlen available on the Aerodynamics Research Group on Blackboard.

A sample submission file for launching FLUENT on the HPC12 cluster is presented.

```
#!/bin/bash -l
#PBS -j oe
#PBS -l nodes=1:ppn=20:typeh,walltime=240:00:00
#PBS -N THE_KITES_WORK!
#PBS -M e.ploumakis@student.tudelft.nl
#PBS -m abe

cd $PBS_O_WORKDIR
# for multiple nodes "cat $PBS_NODEFILE" and at the fluent call command "cnf=$PBS_NODEFILE"
#Set variables for script
# What version of the solver to use
FLUENTSOLVER=3ddp
#HOW MANY CPUS- note that you'll still need to update the $PBS -l nodes line
CPUCOUNT=20
#Which input journal file to use to give fluent?
#INPUT=$PBS_O_WORKDIR/$PBS_JOBNAME
INPUT=THE_KITES_WORK.jou
#Where do we want to put output at?
```

```

OUTPUT=$PBS_O_WORKDIR/$PBS_JOBID.txt

# Run Fluent with:
# -pib use Infiniband parallel
# -cnf=$PBS_NODEFILE get the list of machines PBS is running on from the server
# -t$CPUCOUNT use $CPUCOUNT CPUs total
# -g no graphics, batch mode
# -i read the file in $INPUT
# > $OUTPUT 2>&1 Redirect program output to a file in your home directory.

module load intel
module load ansys
module load fluent/15.0
fluent $FLUENTSOLVER -g -t$CPUCOUNT -i $INPUT -psgimpi > $OUTPUT 2>&1

```

A journal file is also necessary when running a job using the queuing system to load the case and save the results. All commands found in the FLUENT GUI can also be executed as TUI commands from a journal file. Journal files have the extension ".jou". A simple journal file to read the case file, compile and load the UDF, monitor a velocity, initialize the flow, set data sampling, run the simulation and finally save the results is presented:

```

/file/read-case /home/eploumakis/12_02_4ADs/12_02_4ADs.cas
/define/user-defined/compiled-functions/compile libudf_ccc yes ccc.c
/define/user-defined/compiled-functions/load libudf_ccc
/solve/monitors/surface/set-monitor vel-fan-1 "Area-Weighted Average" x-velocity (11) yes
/file/read-profile in-prof-13903.prof
/solve/initialize/initialize-flow
/solve/dual-time-iterate 2600 20
/solve/set/data-sampling yes 1 yes yes yes yes
/solve/dual-time-iterate 13000 20
file/write-data /home/eploumakis/12_02_4ADs/dom.dat
file/write-case /home/eploumakis/12_02_4ADs/sdom.cas
exit
yes

```

A-2 FLUENT commands

WRITE PROFILES: Once the desired wind conditions have been reached you need to enable a command in the Solve/Execute commands box. Enable one command and set it to every one time step. Enter the command: "file/write-profile xvels-%t.prof x-velocity y-velocity z-velocity".

READ PROFILES: The commands can be specified in the graphical interface via

Calculation Activities— > Execute commands

or the command line of FLUENT referred to as "TUI". Using the GUI, a command was set to be executed every time step for each one of the following code lines. The saved velocity profiles generated in the precursor simulation are read in the successor simulations using the following commands:

```

/*****
Commands to read velocity profiles in FLUENT every time-step
*****/
(define ttt "file/read-profile/")
(define tm "in-prof-")
(set! tm (string-append tm (number->string (rpgetvar 'ccc))))
(define bbb)
(set! bbb (String-append ttt tm))
(ti-menu-load-string bbb)
(models-changed)
define/user-defined/execute-on-demand "ts_counter::libudf_ccc"
(%rpgetvar 'ccc)

```

A-3 User Defined Function (UDF) code

Each one of the following commands is executed in the beginning of every single time-step of the simulation. You need to create UDF that counts the time-steps, it must be written in C++ and saved as a ".c" file. The "ccc" variable was used as counter. The library created here is libudf_ccc.

```

/*****
UDF for advancing velocity profiles "ccc" each time step in FLUENT
*****/
#include "udf.h"
int minFiles=13900;
int maxFiles=25000;

DEFINE_ON_DEMAND(ts_counter)
{
int udfccc=RP_Get_Integer("ccc");
if(udfccc>maxFiles)
{udfccc=minFiles;}
else
{udfccc=udfccc+1;}
RP_Set_Integer("ccc",udfccc);
}

```

Appendix B

Four wind turbines - local grid refinement

The reference grid used in the present study has an equidistant resolution of $D/10$ in the entire domain. In order to study the numerical error due to resolution, one successive refinement is performed in a square box that extends from inlet to outlet surrounding the disc area. The square box covers the area of interest (disc locations) and the wake calculations are performed. The size of the refinement box is $L_x=2240\text{m} \times L_y=160\text{m} \times L_z=160\text{m}$ and extends from the inlet plane all the way to the outlet. The results of the local grid refinement study are not included in the main part of the report since it involves refining the grid size only on a small area of the computational domain. No strong conclusions can be drawn since simple sub-grid-scale models change their behaviour based on the grid resolution which could in turn lead to the profile changes of the parameters presented below. Since for simple SGS models like the Smagorinsky it is important to follow a constant grid resolution the results presented here could only be of future value if validated from global grid refinement studies. Global grid refinement was considered too-computationally intensive for the purposes of the present work.

The choice of only one successive grid refinement is based on the results reported in the work of Nilsson (2012) [99]. Nilsson reported that insignificant changes were predicted in the wind turbine power output and turbulence intensity levels for grid resolutions finer than $D/20$. The grid refinement case, in our simulations, involves a background grid with $D/10$ and a square box where the $D/20$ refinement takes place. The coarse case involves a uniform grid of $D/5$ without any refinement in the area close to the turbine locations.

First and second order statistics are compared for the coarse ($D/5$), the base ($D/10$) and the refined ($D/20$) case. The streamwise velocity and turbulence intensity profiles are plotted at a distance of $x/D=5$ downstream each one of the actuator discs in figures B-1 and B-2 respectively. An underestimation of the streamwise velocity is found for the larger grid sizes, which is more pronounced in the centre of the wake downwind AD2 and AD3. The time-averaged velocities at the disc area, for each one of the three successive grid refinements, is presented in table B-1.

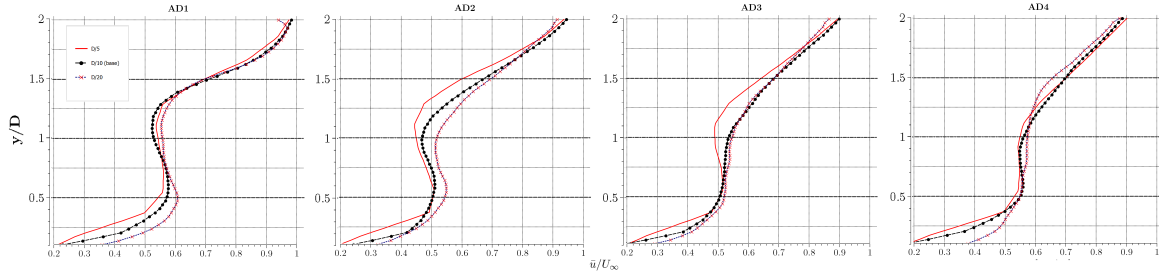


Figure B-1: Comparison of the normalized x -velocity \bar{u}/U_∞ profiles in the wake of the discs with rotation (ADM-R). The time-averaged velocities are plotted at $x/D=5$ downwind each one of the discs.

Successive refinements of the grid size indicate an increase in the predicted turbulence intensity values above the hub height; a trend more pronounced for first three actuator discs. Lower turbulence levels, the closer we move towards the ground surface, are observed for the finer grid sizes. Despite the decrease in the TI levels below hub height, for the finer grid sizes, the maximum TI values are still found at the low-tip height of the turbines. This is in direct contradiction with the results reported in the numerical [31] and experimental [100] work found in the literature. Maximum TI values were reported near the top-tip level of the turbines, where the mean shear is maximum. Excessive gradients of the mean velocity near the wall, due to the contribution of the Smagorinsky-Lilly SGS model, already reported in the work of Mason (1994) [70], provide the explanation of the trend observed in the present study.

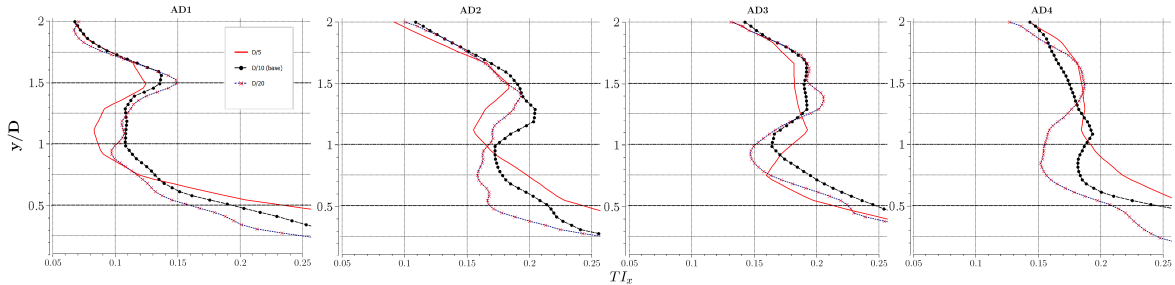


Figure B-2: Comparison of the turbulence intensity levels, in the streamwise direction (x -direction), for different grid sizes. The TI data are plotted at $x/D=5$ downwind each one of the discs (ADM-R).

An increase in efficiency, presented in table B-1, is associated with the case characterized by smaller grid spacing. The simulation results show an efficiency increase of 1.5% for the finer grid (D/20) relative to the base case (D/10). On the other hand, the coarser grid (D/5) underestimates the extracted power by the turbines by 7%. The efficiency values can at this point be considered to characterize the wake flow since the power extracted by the first wind turbine is within a 1% difference for all simulated cases. The computational load for the refined case (D/20) was estimated to an extra ~ 2 days/test-case. Since, $<1\%$ discrepancy in the predicted efficiency values was recorded the extra computational time was not considered an investment worth considering. In case the turbulence intensity levels in the wake region

were the main study focus, the grid refinement of D/20 should have been considered. The grid size of the baseline case (D/10) is the only one considered throughout the present study. There was no attempt on successive refinements of the mesh resolution close to the actuator discs, something that could be addressed in future studies.

Table B-1: Case (d) results: Grid resolution and computational time per time step for the coarse (D/5), base (D/10) and refined (D/20) grid sizes. The time-averaged streamwise velocities at the discs and the efficiency values for the array are presented.

ADM-R	Grid resol.	Nodes	Comp. time	AD1	AD2	AD3	AD4	efficiency [%]
	D/5	456,775	10 s/t.s.	5.912	4.265	3.806	3.952	48.5
	D/10 (base)	2,894,862	38 s/t.s.	5.954	4.402	4.226	4.575	54.7
	D/10, D/20	3,710,814	52 s/t.s.	5.963	4.514	4.483	4.468	55.3

Kite system calculations

C-1 Pressure distribution

The pressure jump for a reference kite surface, with chord length $c=1$, is calculated to estimate the force/ m^2 for the simulations with a free-stream velocity of 7.8 m/s (table C-1). The pressure coefficient data were obtained from the simulations of art de Wachter (2008) [13]. The velocities at the upper and lower surface of the kite are calculated by solving eq. 7-3. The pressures on both sides are calculated from eq. 7-2. The averaged pressures per section are then weighted based on the length of each section (S_l) to obtain the weighted pressure average for the kite surface ($\Delta P_{w,avg}$). An average pressure jump of 39Pa is used for the simulations.

C-2 Normal force calculations

Calculations of the normal force coefficient and normal force based on the distribution of the pressure coefficient on the upper and lower surfaces of the wing section for chord length, $c=16m$ (table C-2). The length of each section S_l is calculated from $((x/c)_{i+1}-(x/c)_i) \cdot c$. The surface area S_A is obtained by discretizing the wing, in the span-wise direction, in 28 sections and multiplying the average width $S_w=1.14m$ with S_l . The total force in each one of the wing sections was calculated from eq. 7-1 for a free-stream velocity at flight height of 7.8 m/s .

Table C-1: Pressure jump calculation steps for a reference wing surface with chord $c=1$ for an ambient velocity of 7.8 m/s.

x/c	$C_{p,l}$	$C_{p,u}$	$U_l[m/s]$	$U_u [m/s]$	$P_l [Pa]$	$P_u [Pa]$	$\Delta P [Pa]$	$S_l [m]$	$\Delta P_{w,avg}[Pa]$
0	0.000	-2.500	2.45	4.58	0.00	-32.10	32.10	0	0.00
0.002	0.750	-2.800	1.22	4.77	0.69	-39.04	39.72	0.002	7.18
0.004	0.830	-3.000	1.01	4.89	0.52	-44.03	44.54	0.002	8.43
0.006	0.840	-3.100	0.98	4.96	0.49	-46.63	47.12	0.002	9.17
0.008	0.850	-3.500	0.95	5.19	0.47	-57.78	58.25	0.002	10.54
0.01	0.960	-3.400	0.49	5.13	0.14	-54.89	55.03	0.002	11.33
0.015	0.950	-3.300	0.55	5.08	0.17	-52.06	52.24	0.005	26.82
0.02	0.930	-2.800	0.65	4.77	0.24	-39.04	39.28	0.005	22.88
0.03	0.910	-2.400	0.73	4.51	0.30	-29.94	30.24	0.01	34.76
0.04	0.860	-2.000	0.92	4.24	0.44	-22.01	22.45	0.01	26.35
0.06	0.750	-2.140	1.22	4.34	0.69	-24.65	25.34	0.02	47.80
0.08	0.650	-2.250	1.45	4.41	0.83	-26.83	27.66	0.02	53.00
0.1	0.560	-2.500	1.62	4.58	0.90	-32.10	33.01	0.02	60.67
0.15	0.410	-3.200	1.88	5.02	0.89	-49.31	50.20	0.05	208.01
0.2	0.290	-2.300	2.06	4.45	0.76	-27.85	28.60	0.05	197.00
0.25	0.201	-1.500	2.19	3.87	0.59	-13.76	14.35	0.05	107.37
0.3	0.122	-1.250	2.29	3.67	0.39	-10.32	10.71	0.05	62.65
0.35	0.066	-1.000	2.37	3.46	0.23	-7.34	7.56	0.05	45.69
0.4	0.015	-0.750	2.43	3.24	0.05	-4.82	4.87	0.05	31.09
0.45	0.030	-0.740	2.41	3.23	0.11	-4.72	4.83	0.05	24.25
0.5	0.150	-0.750	2.26	3.24	0.47	-4.82	5.28	0.05	25.28
0.55	0.170	-0.550	2.23	3.05	0.52	-3.13	3.65	0.05	22.32
0.6	0.200	-0.550	2.19	3.05	0.59	-3.13	3.71	0.05	18.40
0.7	0.220	-0.280	2.16	2.77	0.63	-1.31	1.94	0.1	28.30
0.8	0.000	-0.200	2.45	2.68	0.00	-0.88	0.88	0.1	14.13
0.9	-0.120	0.203	2.59	2.18	-0.49	0.59	-1.09	0.1	-1.03
0.95	-0.500	-0.350	3.00	2.84	-2.75	-1.73	-1.02	0.05	-5.26
Sum								1	39.05

Table C-2: Pressure coefficient data for the upper and lower surface of the 470 m^2 kite based on the simulation data obtained from Aart de Wachter (2008) [13]. The normal force coefficient and normal force values for a wind velocity of 7.8m/s, 11m/s & 15.6m/s

x/c	$C_{p,l}$	$C_{p,u}$	S_l [m]	S_A [m^2]	C_{F_a}	F_a [N] ($U_w=7.8m/s$)	F_a [N] ($U_w=11.1m/s$)	F_a [N] ($U_w=15.6m/s$)
0.000	0.000	-2.500	0	0.00	2.50	0	0	0
0.002	0.750	-2.800	0.032	0.94	3.55	124	250	497
0.004	0.830	-3.000	0.032	0.94	3.83	134	269	537
0.006	0.840	-3.100	0.032	0.94	3.94	138	277	552
0.008	0.850	-3.500	0.032	0.94	4.35	152	306	609
0.010	0.960	-3.400	0.032	0.94	4.36	153	307	611
0.015	0.950	-3.300	0.08	2.35	4.25	372	747	1489
0.02	0.930	-2.800	0.08	2.35	3.73	327	656	1307
0.03	0.910	-2.400	0.16	4.70	3.31	580	1163	2319
0.04	0.860	-2.000	0.16	4.70	2.86	501	1005	2004
0.06	0.750	-2.140	0.32	9.40	2.89	1012	2032	4049
0.08	0.650	-2.250	0.32	9.40	2.90	1016	2039	4063
0.10	0.560	-2.500	0.32	9.40	3.06	1072	2151	4288
0.15	0.410	-3.200	0.8	23.50	3.61	3161	6345	12645
0.20	0.290	-2.300	0.8	23.50	2.59	2268	4552	9072
0.25	0.201	-1.500	0.8	23.50	1.70	1489	2989	5957
0.30	0.122	-1.250	0.8	23.50	1.37	1201	2411	4806
0.35	0.066	-1.000	0.8	23.50	1.07	934	1874	3734
0.40	0.015	-0.750	0.8	23.50	0.77	670	1345	2680
0.45	0.030	-0.740	0.8	23.50	0.77	674	1353	2697
0.50	0.150	-0.750	0.8	23.50	0.90	788	1582	3153
0.55	0.170	-0.550	0.8	23.50	0.72	631	1265	2522
0.60	0.200	-0.550	0.8	23.50	0.75	657	1318	2627
0.70	0.220	-0.280	1.6	47.00	0.50	876	1758	3503
0.80	0.000	-0.200	1.6	47.00	0.20	350	703	1401
0.90	-0.120	0.203	1.6	47.00	-0.32	-566	-1135	-2263
0.95	-0.500	-0.350	0.8	23.50	-0.15	-131	-264	-525
1.00	-0.190	-0.090	0.8	23.50	-0.10	-88	-177	-352
Sum			16	470		18,495	37,120	73,982

Bibliography

- [1] Pankaj K Jha, Earl PN Duque, Jessica L Bashioum, and Sven Schmitz. Unraveling the mysteries of turbulence transport in a wind farm. *Energies*, 8(7):6468–6496, 2015.
- [2] Rebecca Jane Barthelmie, K Hansen, Sten Tronæs Frandsen, Ole Rathmann, JG Schepers, W Schlez, J Phillips, K Rados, A Zervos, ES Politis, et al. Modelling and measuring flow and wind turbine wakes in large wind farms offshore. *Wind Energy*, 12(5):431–444, 2009.
- [3] Daniel Boonman, Carsten Broich, Ronald Deerenberg, Koen Groot, Ash Hamraz, Roeland Kalthof, Gijs Nieuwint, Jan Schneiders, Yu Tang, and Jord Wiegerink. Tu delft - dse report, wind farm efficiency. Technical report, 2011.
- [4] Jeroen Breukels. *An engineering methodology for kite design*. TU Delft, Delft University of Technology, 2011.
- [5] Rolf van der Vlugt, Johannes Peschel, and Roland Schmehl. Design and experimental characterization of a pumping kite power system. In *Airborne wind energy*, pages 403–425. Springer, 2013.
- [6] Gianmauro Maneia, Caterina Tribuzi, Daniela Tordella, and Michele Iovieno. Aerodynamics of a rigid curved kite wing. *arXiv preprint arXiv:1306.4148*, 2013.
- [7] Inc. dba Flightlab. *Three-Dimensional Aerodynamics, Flight Emergency & Advanced Maneuvers Training*. Flightlab Ground School, 2009.
- [8] John M Wallace and Peter V Hobbs. *Atmospheric science: an introductory survey*, volume 92. Academic press, 2006.
- [9] Tony Burton, Nick Jenkins, David Sharpe, and Ervin Bossanyi. *Wind energy handbook*. John Wiley & Sons, 2011.
- [10] Erich Hau and Horst Von Renouard. *Wind turbines: fundamentals, technologies, application, economics*. Springer, 2013.

- [11] A Jimenez, A Crespo, E Migoya, and J Garcia. Advances in large-eddy simulation of a wind turbine wake. In *Journal of Physics: Conference Series*, volume 75, page 012041. IOP Publishing, 2007.
- [12] David Wood. *Small wind turbines*. Springer, 2011.
- [13] Aart de Wachter. Deformation and aerodynamic performance of a ram-air wing. Master's thesis, Delft University of Technology, 2008.
- [14] Falko Fritz. Application of an automated kite system for ship propulsion and power generation. In *Airborne wind energy*, pages 359–372. Springer, 2013.
- [15] Fernando Porté-Agel, Hao Lu, and Yu-Ting Wu. A large-eddy simulation framework for wind energy applications. In *The Fifth International Symposium on Computational Wind Engineering (CWE2010), Chapel Hill, North Carolina*, 2010.
- [16] Stefan Ivanell, Robert Mikkelsen, Jens Sørensen, and D Henningson. Acd modelling of wake interaction in the horns rev wind farm. In *Extended Abstracts for Euromech Colloquium*, volume 508, 2009.
- [17] Raúl Bayoán Cal, José Lebrón, Luciano Castillo, Hyung Suk Kang, and Charles Meneveau. Experimental study of the horizontally averaged flow structure in a model wind-turbine array boundary layer. *Journal of Renewable and Sustainable Energy*, 2(1):013106, 2010.
- [18] Johan Meyers and Charles Meneveau. Large eddy simulations of large wind-turbine arrays in the atmospheric boundary layer. *AIAA Paper*, 827:2010, 2010.
- [19] Marc Calaf, Charles Meneveau, and Johan Meyers. Large eddy simulation study of fully developed wind-turbine array boundary layers. *Physics of Fluids (1994-present)*, 22(1):015110, 2010.
- [20] Guillaume España, Sandrine Aubrun, Stéphane Loyer, and Philippe Devinant. Spatial study of the wake meandering using modelled wind turbines in a wind tunnel. *Wind Energy*, 14(7):923–937, 2011.
- [21] Ferhat Bingöl, Gunner C Larsen, and Jakob Mann. Wake meandering-an analysis of instantaneous 2d laser measurements. In *Journal of Physics: Conference Series*, volume 75, page 012059. IOP Publishing, 2007.
- [22] Daniel Baldacchino and Gerard JW van Bussel. Wind turbine wake stability investigations using a vortex ring modelling approach. In *Journal of Physics: Conference Series*, volume 555, page 012111. IOP Publishing, 2014.
- [23] Richard JAM Stevens, Dennice Gayme, and Charles Meneveau. Using the coupled wake boundary layer model to evaluate the effect of turbulence intensity on wind farm performance. In *Journal of Physics: Conference Series*, volume 625, page 012004. IOP Publishing, 2015.
- [24] Fernando Porté-Agel, Yu-Ting Wu, Hao Lu, and Robert J Conzemius. Large-eddy simulation of atmospheric boundary layer flow through wind turbines and wind farms. *Journal of Wind Engineering and Industrial Aerodynamics*, 99(4):154–168, 2011.

-
- [25] Björn Witha, G Steinfeld, M Dörenkämper, and D Heinemann. Large-eddy simulation of multiple wakes in offshore wind farms. In *Journal of Physics: Conference Series*, volume 555, page 012108. IOP Publishing, 2014.
- [26] G Russell, PG Jarvis, and JL Monteith. Absorption of radiation by canopies and stand growth. *Plant canopies: their growth, form and function*, 31:21–39, 1989.
- [27] B Sanderse, SP Pijl, and B Koren. Review of computational fluid dynamics for wind turbine wake aerodynamics. *Wind Energy*, 14(7):799–819, 2011.
- [28] LJ Vermeer, Jens Nørkær Sørensen, and A Crespo. Wind turbine wake aerodynamics. *Progress in aerospace sciences*, 39(6):467–510, 2003.
- [29] Jens Nørkær Sørensen. Aerodynamic aspects of wind energy conversion. *Annual Review of Fluid Mechanics*, 43:427–448, 2011.
- [30] Martin Otto Laver Hansen, Jens Nørkær Sørensen, S Voutsinas, Niels Sørensen, and H Aa Madsen. State of the art in wind turbine aerodynamics and aeroelasticity. *Progress in aerospace sciences*, 42(4):285–330, 2006.
- [31] Yu-Ting Wu and Fernando Porté-Agel. Atmospheric turbulence effects on wind-turbine wakes: An les study. *energies*, 5(12):5340–5362, 2012.
- [32] Yu-Ting Wu and Fernando Porté-Agel. Simulation of turbulent flow inside and above wind farms: Model validation and layout effects. *Boundary-layer meteorology*, 146(2):181–205, 2013.
- [33] Niels Troldborg, Jens N Sørensen, and Robert Mikkelsen. Actuator line simulation of wake of wind turbine operating in turbulent inflow. In *Journal of physics: conference series*, volume 75, page 012063. IOP Publishing, 2007.
- [34] Somnath Baidya Roy and Justin J Traiteur. Impacts of wind farms on surface air temperatures. *Proceedings of the National Academy of Sciences*, 107(42):17899–17904, 2010.
- [35] Sonia Wharton and Julie K Lundquist. Atmospheric stability affects wind turbine power collection. *Environmental Research Letters*, 7(1):014005, 2012.
- [36] GP Van den Berg. Wind turbine power and sound in relation to atmospheric stability. *Wind Energy*, 11(2):151–169, 2008.
- [37] M Magnusson and A-S Smedman. Air flow behind wind turbines. *Journal of Wind Engineering and Industrial Aerodynamics*, 80(1):169–189, 1999.
- [38] Nicholas Hamilton, Hyung Suk Kang, Charles Meneveau, and Raúl Bayoán Cal. Statistical analysis of kinetic energy entrainment in a model wind turbine array boundary layer. *Journal of Renewable and Sustainable Energy*, 4(6):063105, 2012.
- [39] Claire VerHulst and Charles Meneveau. Altering kinetic energy entrainment in large eddy simulations of large wind farms using unconventional wind turbine actuator forcing. *Energies*, 8(1):370–386, 2015.

- [40] Dale Crane. *Dictionary of aeronautical terms*. Aviation Supplies & Academics, Incorporated, 2012.
- [41] Miles L Loyd. Crosswind kite power (for large-scale wind power production). *Journal of Energy*, 4(3):106–111, 1980.
- [42] Abe Silverstein and S Katzoff. Design charts for predicting downwash angles and wake characteristics behind plain and flapped wings. 1939.
- [43] Roland B Stull. *An introduction to boundary layer meteorology*, volume 13. Springer, 1988.
- [44] Giorgio Crasto. Numerical simulations of the atmospheric boundary layer. *Universita degli Studi di Cagliari*, 2007.
- [45] JM McDonough. Introductory lectures on turbulence physics, mathematics and modeling. 2004.
- [46] HELGE AAGAARD Madsen. A cfd analysis of the actuator disc flow compared with momentum theory results. In *Proc. 10th IEA Symp. on the Aerodynamics of Wind Turbines, Edinburgh*, pages 109–124, 1996.
- [47] Idriss Ammara, Christophe Leclerc, and Christian Masson. A viscous three-dimensional differential/actuator-disk method for the aerodynamic analysis of wind farms. *Journal of Solar Energy Engineering*, 124(4):345–356, 2002.
- [48] Niels Troldborg, Jens Norker Sørensen, and Robert Flemming Mikkelsen. *Actuator line modeling of wind turbine wakes*. PhD thesis, Technical University of Denmark Danmarks Tekniske Universitet, Department of Energy Engineering Institut for Energiteknik, 2008.
- [49] Robert Mikkelsen, Jens N Sørensen, and Niels Troldborg. Prescribed wind shear modelling combined with the actuator line technique. In *Proceedings of the 2007 EWEC conference, Milan*, 2007.
- [50] I Dobrev, F Massouh, and M Rapin. Actuator surface hybrid model. In *Journal of Physics: Conference Series*, volume 75, page 012019. IOP Publishing, 2007.
- [51] Bert Blocken, Jan Carmeliet, and Ted Stathopoulos. Cfd evaluation of wind speed conditions in passages between parallel buildings - effect of wall-function roughness modifications for the atmospheric boundary layer flow. *Journal of Wind Engineering and Industrial Aerodynamics*, 95(9):941–962, 2007.
- [52] Andrew Riddle, David Carruthers, Alan Sharpe, Christine McHugh, and Jennifer Stocker. Comparisons between fluent and adms for atmospheric dispersion modelling. *Atmospheric environment*, 38(7):1029–1038, 2004.
- [53] Niels N Sørensen. *General purpose flow solver applied to flow over hills*. PhD thesis, Technical University of Denmark Danmarks Tekniske Universitet, Riso National Laboratory for Sustainable Energy Riso Nationallaboratoriet for Baeredygtig Energi, Wind Energy Division Afdelingen for Vindenergi, Aeroelastic Design Aeroelastisk Design, 1995.

-
- [54] Cedric Alinot and Christian Masson. k-e model for the atmospheric boundary layer under various thermal stratifications. *Journal of solar energy engineering*, 127(4):438–443, 2005.
- [55] IP Castro. Cfd for external aerodynamics in the built environment. *The QNET-CFD Network Newsletter*, 2:229–259, 2003.
- [56] NG Wright and GJ Easom. Non-linear k-e turbulence model results for flow over a building at full-scale. *Applied Mathematical Modelling*, 27(12):1013–1033, 2003.
- [57] Zhengtong Xie and Ian P Castro. Les and rans for turbulent flow over arrays of wall-mounted obstacles. *Flow, Turbulence and Combustion*, 76(3):291–312, 2006.
- [58] A Dejoan, JL Santiago, A Martilli, F Martin, and A Pinelli. Comparison between les and rans computations for the must field experiment. part ii: Effects of incident wind angle deviation on the mean flow and plume dispersion. *Boundary-Layer Meteorol*, 135:133–150, 2010.
- [59] N Jarrin, S Benhamadouche, Y Addad, and D Laurence. Synthetic turbulent inflow conditions for large eddy simulation. In *Proceedings, 4th International Turbulence, Heat and Mass Transfer Conference, Antalya, Turkey*, 2003.
- [60] MH Baba-Ahmadi and GR Tabor. Inlet conditions for large eddy simulation of gas-turbine swirl injectors. *AIAA journal*, 46(7):1782–1790, 2008.
- [61] Jakob Mann. The spatial structure of neutral atmospheric surface-layer turbulence. *Journal of Fluid Mechanics*, 273:141–168, 1994.
- [62] D Mehta, AH Van Zuijlen, B Koren, JG Holierhoek, and H Bijl. Large eddy simulation of wind farm aerodynamics: a review. *Journal of Wind Engineering and Industrial Aerodynamics*, 133:1–17, 2014.
- [63] Matthew J Churchfield, Sang Lee, John Michalakes, and Patrick J Moriarty. A numerical study of the effects of atmospheric and wake turbulence on wind turbine dynamics. *Journal of turbulence*, (13):N14, 2012.
- [64] Yu-Ting Wu and Fernando Porté-Agel. Large-eddy simulation of wind-turbine wakes: evaluation of turbine parametrisations. *Boundary-layer meteorology*, 138(3):345–366, 2011.
- [65] Sang Lee, Matthew Churchfield, Patrick Moriarty, J Jonkman, and J Michalakes. Atmospheric and wake turbulence impacts on wind turbine fatigue loadings. In *50th AIAA Aerospace Sciences Meeting including the New Horizons Forum and Aerospace Exposition*, pages 09–12, 2012.
- [66] A Andren, AR Brown, PJ Mason, J Graf, U Schumann, C-H Moeng, and FTM Nieuwstadt. Large-eddy simulation of a neutrally stratified boundary layer: A comparison of four computer codes. *Quarterly Journal of the Royal Meteorological Society*, 120(520):1457–1484, 1994.
- [67] FR Menter. Best practice: Scale-resolving simulations in ansys cfd. *ANSYS Germany GmbH*, pages 1–70, 2012.

- [68] RC Hall. Evaluation of modelling uncertainty. cfd modelling of near-field atmospheric dispersion. project emu final report, european commission directorate-general xii science. *Research and Development Contract EV5V-CT94-0531, WS Atkins Consultants Ltd., Surrey*, 1997.
- [69] PJ Richards and RP Hoxey. Appropriate boundary conditions for computational wind engineering models using the k- ϵ turbulence model. *Journal of wind engineering and industrial aerodynamics*, 46:145–153, 1993.
- [70] Paul J Mason. Large-eddy simulation: A critical review of the technique. *Quarterly Journal of the Royal Meteorological Society*, 120(515):1–26, 1994.
- [71] J Franke and W Frank. Numerical simulation of the flow across an asymmetric street intersection. *Proceedings of the 4EACWE*, 138, 2005.
- [72] ALM Grant. The structure of turbulence in the near-neutral atmospheric boundary layer. *Journal of the atmospheric sciences*, 49(3):226–239, 1992.
- [73] Fernando Porté-Agel, Charles Meneveau, and Marc B Parlange. A scale-dependent dynamic model for large-eddy simulation: application to a neutral atmospheric boundary layer. *Journal of Fluid Mechanics*, 415:261–284, 2000.
- [74] Paul J Mason and DJ Thomson. Large-eddy simulations of the neutral-static-stability planetary boundary layer. *Quarterly Journal of the Royal Meteorological Society*, 113(476):413–443, 1987.
- [75] Vestas. (u.d.). project description, vestas (2008). <http://pdf.directindustry.com/pdf/vestas/v80-20-mw-brochure/20680-53605.html>. Accessed: 2015-04-29.
- [76] Jennifer Annoni, Peter Seiler, Kathryn Johnson, Paul Fleming, and Pieter Gebraad. Evaluating wake models for wind farm control. In *American Control Conference (ACC), 2014*, pages 2517–2523. IEEE, 2014.
- [77] Eilyan Bitar and Pete Seiler. Coordinated control of a wind turbine array for power maximization. In *American Control Conference (ACC), 2013*, pages 2898–2904. IEEE, 2013.
- [78] FLUENT 14.5 users manual, les near-wall treatment. http://www.arc.vt.edu/ansys_help/flu_ug/flu_ug_sec_bc_fan.html. Accessed: 2015-04-28.
- [79] FLUENT 14.5 users manual, les near-wall treatment. http://www.arc.vt.edu/ansys_help/flu_ug/flu_ug_sec_report_surface_integrals_generate.html. Accessed: 2015-04-28.
- [80] Konstantinos Rados, G Larsen, R Barthelmie, W Schlez, B Lange, G Schepers, T Hegberg, and M Magnisson. Comparison of wake models with data for offshore windfarms. *Wind Engineering*, 25(5):271–280, 2001.
- [81] Davide Medici and PH Alfredsson. Measurements on a wind turbine wake: 3d effects and bluff body vortex shedding. *Wind Energy*, 9(3):219–236, 2006.

-
- [82] Takao Maeda, Yasunari Kamada, Junsuke Murata, Sayaka Yonekura, Takafumi Ito, Atsushi Okawa, and Tetsuya Kogaki. Wind tunnel study on wind and turbulence intensity profiles in wind turbine wake. *Journal of Thermal Science*, 20(2):127–132, 2011.
- [83] Kurt S Hansen, Rebecca J Barthelmie, Leo E Jensen, and Anders Sommer. The impact of turbulence intensity and atmospheric stability on power deficits due to wind turbine wakes at horns rev wind farm. *Wind Energy*, 15(1):183–196, 2012.
- [84] Corey D Markfort, Wei Zhang, and Fernando Porté-Agel. Turbulent flow and scalar transport through and over aligned and staggered wind farms. *Journal of Turbulence*, 13(1), 2012.
- [85] Leonardo P Chamorro and Fernando Porté-Agel. A wind-tunnel investigation of wind-turbine wakes: boundary-layer turbulence effects. *Boundary-layer meteorology*, 132(1):129–149, 2009.
- [86] Yu-Ting Wu and Fernando Porté-Agel. Large-eddy simulation of wind-turbine wakes: evaluation of turbine parametrisations. *Boundary-layer meteorology*, 138(3):345–366, 2011.
- [87] John J Bertin and Michael L Smith. *Aerodynamics for engineers*, volume 1. Prentice Hall Englewood Cliffs, 1989.
- [88] Storm Dunker. Ram-air wing design considerations for airborne wind energy. In *Airborne Wind Energy*, pages 517–546. Springer, 2013.
- [89] John David Anderson Jr. *Fundamentals of aerodynamics*. Tata McGraw-Hill Education, 1985.
- [90] Dr. Roland Schmehl. Kiting for wind power. http://www.anurac.de/wp-content/uploads/Schmehl_Kite.pdf. Accessed: 2015-03-12.
- [91] Anurac kite design. <http://anurac.de/leistung/kite-design/>. Accessed: 2015-03-12.
- [92] Dr. Roland Schmehl. Large-scale power generation with kites. <http://www.lr.tudelft.nl/actueel/artikelen-homepage/large-scale-power-generation-with-kites/>. Accessed: 2015-03-12.
- [93] John Finnigan. Turbulence in plant canopies. *Annual Review of Fluid Mechanics*, 32(1):519–571, 2000.
- [94] Mathias Rotach. *Turbulence within and above an urban canopy*. PhD thesis, Diss. Naturwiss. ETH Zürich, Nr. 9439, 1991. Ref.: A. Ohmura; Korref.: HC Davies; Korref.: TR Oke, 1991.
- [95] H Werner and H Wengle. Large-eddy simulation of turbulent flow over and around a cube in a plate channel. In *Turbulent Shear Flows 8*, pages 155–168. Springer, 1993.
- [96] FLUENT 14.5 users manual, les near-wall treatment. http://www.arc.vt.edu/ansys_help/flu_th/flu_th_turb_les_wall_treatment.html. Accessed: 2015-04-25.

-
- [97] DJ Carruthers, RJ Holroyd, JCR Hunt, WS Weng, AG Robins, DD Apsley, DJ Thompson, and FB Smith. Uk-adms: A new approach to modelling dispersion in the earth's atmospheric boundary layer. *Journal of wind engineering and industrial aerodynamics*, 52:139–153, 1994.
- [98] Gal Berkooz, Philip Holmes, and John L Lumley. The proper orthogonal decomposition in the analysis of turbulent flows. *Annual review of fluid mechanics*, 25(1):539–575, 1993.
- [99] Karl Nilsson. Numerical computations of wind turbine wakes and wake interaction: Optimization and control. 2012.
- [100] Leonardo P Chamorro and Fernando Porté-Agel. Turbulent flow inside and above a wind farm: a wind-tunnel study. *Energies*, 4(11):1916–1936, 2011.